Title
Combining Dynamic Earthquake and Tsunami Models With Case Studies Offshore Alaska and Southern California

Author
Ryan, Kenny J.

Publication Date
2016

UNIVERSITY OF CALIFORNIA
RIVERSIDE

Combining Dynamic Earthquake and Tsunami Models With Case Studies Offshore Alaska and Southern California

A Dissertation submitted in partial satisfaction
of the requirements for the degree of

Doctor of Philosophy

in

Geological Sciences

by

Kenny Ryan

June 2016

Dissertation Committee:

David D. Oglesby, Chairperson
Gareth J. Funning
Eric L. Geist
Abhijit Ghosh

The Dissertation of Kenny Ryan is approved:

Committee Chairperson

University of California, Riverside

Acknowledgments

I thank my PhD committee members for their thoughtful comments and critiques that led to the improvement of this document. I am very appreciative of David Oglesby for his support, mentorship, and friendship throughout my PhD process and beyond. I am also indebted to many friends within the Department of Earth Sciences at the University of California, Riverside, for their help and support over the years. Chapter 2 has been published as part of a USGS Open-File Report (Ryan, Oglesby, Geist, 2013), and Chapter 3 has been published in Geophysical Research Letters (Ryan, Geist, Barall, Oglesby, 2015).

ABSTRACT OF THE DISSERTATION

Combining Dynamic Earthquake and Tsunami Models With Case Studies Offshore Alaska and Southern California

by

Kenny Ryan

Doctor of Philosophy, Graduate Program in Geological Sciences
University of California, Riverside, June 2016
David D. Oglesby, Chairperson

Earthquakes and their corresponding tsunamis pose significant hazard to populated regions around the world. Therefore, it is critically important that we seek to more fully understand the physics of the combined earthquake-tsunami system. One way to address this goal is through numerical modeling. The work discussed herein focuses on combining dynamic earthquake and tsunami models through the use of the Finite Element Method (FEM) and the Finite Difference Method (FDM). Dynamic earthquake models account for the force that the entire fault system exerts on each individual element of the model for each time step, so that earthquake rupture takes a path based on the physics of the model; dynamic tsunami models can incorporate water height variations to produce water wave formation, propagation, and inundation. *Chapter 1* provides an introduction to some important concepts and equations of elastodynamics and fluid dynamics as well as a brief example of the FEM. In *Chapter 2*, we investigate the 3-D effects of realistic fault dynamics on slip, free surface deformation, and resulting tsunami formation from an M_w 9 megathrust earthquake offshore Southern Alaska. Corresponding tsunami models, which

use a FDM to solve linear long-wave equations, match sea floor deformation, in time, to the free surface deformation from the rupture simulations. Tsunamis generated in this region could have large adverse effects on Pacific coasts. In *Chapter 3*, we construct a 3-D dynamic rupture model of an earthquake on a reverse fault structure offshore Southern California to model the resulting tsunami, with a goal of elucidating the seismic and tsunami hazard in this area. The corresponding tsunami model uses final seafloor displacements from the rupture model as initial conditions to compute local propagation and inundation, resulting in large peak tsunami amplitudes northward and eastward due to site and path effects. In *Chapter 4*, we begin to evaluate 2-D earthquake source parameters from characteristics of the Rayleigh-wave field by running a suite of 2-D dynamic rupture models on thrust/reverse faults that vary in dip angle and fault curvature, and with equivalent prestress conditions such as constant traction across the fault or variable prestress distributions. We compare traveling Rayleigh-wave breakout amplitudes with fault slip distribution. Such Rayleigh-wave analysis has implications for early estimation of far-field tsunami amplitude, since source parameters are directly related to tsunami generation and propagation.

Contents

List of Figures

List of Tables

Chapter 1

Introduction

Below we give a brief overview of essential concepts and equations that are employed by computational models throughout the rest of the dissertation, and then we conclude with a short note on the Finite Difference Method as well as a Finite Element Method (FEM) example. Simple “derivations” are given for many analytic equations, while constitutive equations – that describe relationships between physical quantities (e.g., stress and displacement) – are also listed. More comprehensive derivations can be found in books on elasticity (e.g., Sokolnikoff, 1956), fluid mechanics (e.g., Owczarek, 1968; Currie, 2013, updated from 1974), and geophysics (e.g., Dean and Dalrymple, 1991; Stein and Wysession, 2003; Shearer, 2009; Aki and Richards, 2009). The FEM is demonstrated by the 1-D shallow water wave equations, and we follow similar notation and procedures to that of Hughes (2000).

1.1 Solid Mechanics: Key Concepts in Modeling Earthquakes

1.1.1 Continuum hypothesis

The continuum hypothesis is one common and basic assumption in the numerical analysis of physical processes. In this approach, individual small particles (i.e., molecules) are ignored. Instead, continuous matter is assumed with field variables such as density and velocity being uniquely defined at specific locations in the physical model. These field variables are further assumed to be average values for all (un-modeled) small particles within a small neighborhood ϵ surrounding those particles. Differential equations are then used to describe the variation (in time and space) of field variables. A continuum approximation is valid if the number of molecules per small volume neighborhood, n, is very large compared to the small volume neighborhood ϵ, and also if that small volume neighborhood is very small compared to the volume V of the model space:

$$\frac{1}{n} \ll \epsilon \ll V.$$

This approach works for well for dense gases, liquids, and solids. In contrast, a statistical approach that focuses on the dynamics of molecular movements, while useful, is not well developed for dense mixtures. We utilize the continuum approximation here.

1.1.2 Strain

A single continuous body is said to be *strained* if the relative position of points (i.e., the distance between points) within that body changes (e.g., Sokolnikoff, 1956). Any change in the relative position of points is termed a *deformation*. It is important to note the difference between deformation and *rigid displacements*, that is, translations and rotations, which do not alter the distance between any two points in the body. Motions on and near the surface of the Earth have both deformation and rigid displacement components. For our purposes we will be referring to small deformations relative to the size of the body being strained. Figure 1.1 shows a cartoon schematic of a body (of mass M) undergoing deformation and rigid displacement. The small vector $\delta\mathbf{x}$ points from sample point A to sample point B (i.e., points A and B are close to each other) and has a magnitude that is equal to the distance between the two points. If that body is rigidly displaced and deformed, we see that the new small vector $\delta\mathbf{x}'$ from point A to point B has a different direction and magnitude than $\delta\mathbf{x}$. The position of point A is represented by the vector $\mathbf{x}$ and the displacement that point A undergoes is represented by the vector $\mathbf{u}$. Similarly, the position of point B is represented by the vector $\mathbf{x} + \delta\mathbf{x}$ and the displacement that point B undergoes is represented by the vector $\mathbf{u} + \delta\mathbf{u}$. Thus, the relative displacement between

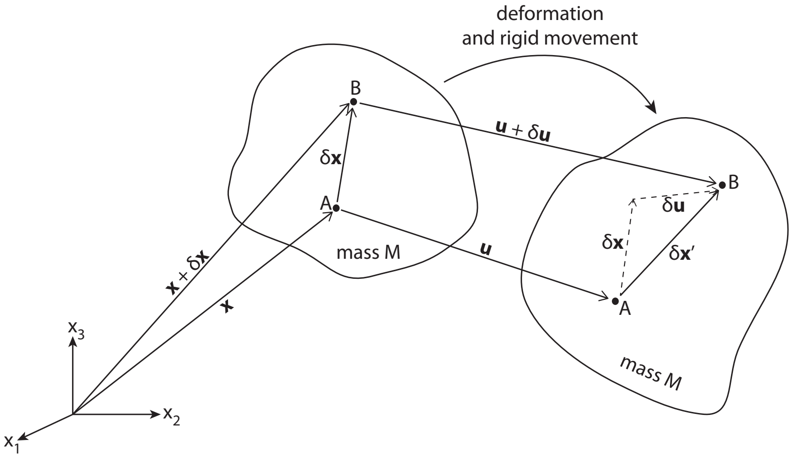

Figure 1.1: A schematic of a continuous body experiencing displacement.

points A and B within the body at its original state and its altered state is $\delta\mathbf{u}$. If we consider each vector component of $\mathbf{u}$, that is, u_i for $i = \{1, 2, 3\}$, to be a function of $\mathbf{x}$, we can expand each component in a truncated Taylor series to approximate a value for u_i at $\mathbf{x} + \delta\mathbf{x}$:

$$u_i(\mathbf{x} + \delta\mathbf{x}) \approx u_i(\mathbf{x}) + \frac{\partial u_i(\mathbf{x})}{\partial x_j}\delta x_j$$

where we will be using the Einstein summation convention, so that repeated indices are summed (e.g., $\alpha_{ij}x_j = \alpha_{i1}x_1 + \alpha_{i2}x_2 + \alpha_{i3}x_3$). Using the approximation above, each component of the relative displacement $\delta\mathbf{u}$ can be approximated by the last term in the truncated Taylor series which depends on the position vector $\mathbf{x}$:

$$\delta u_i \approx \frac{\partial u_i(\mathbf{x})}{\partial x_j}\delta x_j.$$

Another way to write this is

$$\delta u_i \approx \frac{\partial u_i}{\partial x_j}\delta x_j = \frac{1}{2}\left(\frac{\partial u_i}{\partial x_j} + \frac{\partial u_j}{\partial x_i}\right)\delta x_j + \frac{1}{2}\left(\frac{\partial u_i}{\partial x_j} - \frac{\partial u_j}{\partial x_i}\right)\delta x_j = (e_{ij} + w_{ij})\delta x_j \tag{1.1}$$

where $e_{ij} = \frac{1}{2}\left(\frac{\partial u_i}{\partial x_j} + \frac{\partial u_j}{\partial x_i}\right)$ and $w_{ij} = \frac{1}{2}\left(\frac{\partial u_i}{\partial x_j} - \frac{\partial u_j}{\partial x_i}\right)$ are termed the *strain* and *rotation* tensors, respectively. For a body that experiences only *translational* rigid motion, $\delta\mathbf{u}$ will obviously be zero, so translational motion does not contribute to the relative displacement components δu_i. It can be shown that, since the magnitude of vector $\delta\mathbf{x}$ is unchanged by rigid displacements, rigid rotations do contribute to the relative displacement components δu_i and are of the skew-symmetric form w_{ij} (i.e., $w_{ij} = -w_{ji}$) (e.g., Sokolnikoff, 1956). The remaining contributions to δu_i result from deformation and are of the symmetric form e_{ij} (i.e., $e_{ij} = e_{ji}$). Note that the rate of strain tensor involves derivatives of velocities instead of displacements, and thus can be written as $\dot{e}_{ij}$ where the dot signifies the time derivative.

1.1.3 Stress

If we consider a continuous medium as before, a mass M can have two different types of forces act on it – *body* forces and *surface* forces. When the sum of these forces is not zero, mass M accelerates and may or may not deform. Body forces are forces that act on the volume of a body; therefore, such forces are proportional to the mass of the body. An example of a body force is the force due to gravity $\rho\mathbf{g}\delta V$, where ρ is the density of the material, $\mathbf{g}$ is the acceleration due to gravity, and δV is a small volume that the force is applied to. For a large body, the body force needs to be summed for each δV so that the total body force is $\int_V \rho\mathbf{g}\,dV$. Surface forces are forces that act on the surface of a body; therefore, such forces are related to the surface area of that body. An example of a surface force is the force that results from the hydrostatic pressure on an object that is submerged within a fluid, where the pressure acts in different directions based on the orientation of the object's surface. Let $\mathbf{F}_s = \mathbf{Q}\delta S$, where $\mathbf{Q}$ is a force per area δS, be a surface force acting on some small surface area δS of a volume. Now we can define the traction vector $\mathbf{T}$, which is a force per unit area, as a limiting case when we shrink the surface element to zero:

$$\mathbf{T} = \lim_{\delta S \to 0} \frac{\mathbf{F}_s}{\delta S} = \lim_{\delta S \to 0} \mathbf{Q}. \tag{1.2}$$

Figure 1.2 shows the traction vector acting on an infinitesimal surface element dS of some body of mass M. The net surface force for the body is then $\int_S \mathbf{T}\,dS$.

The traction vector $\mathbf{T}$ clearly depends on the orientation of the surface on which it acts, and the orientation of a planar surface is described by its unit normal vector $\mathbf{n}$. The relationship between the traction vector $\mathbf{T}$ and the unit normal vector $\mathbf{n}$ is through the

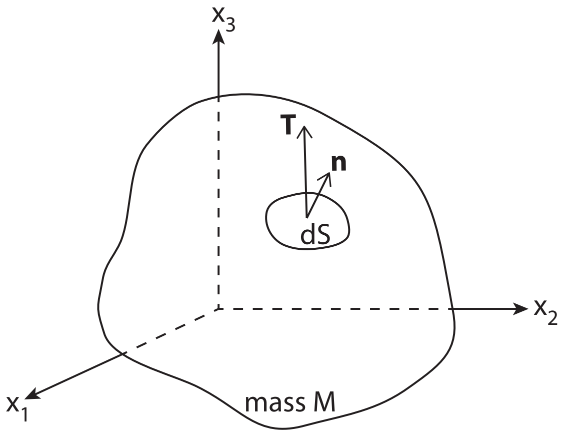

Figure 1.2: A schematic of a continuous body with the traction vector **T** acting on an infinitesimal surface element dS with unit normal **n**.

stress tensor $\boldsymbol{\sigma}$. We can demonstrate this in 2-D. Figure 1.3 shows a small right triangle in equilibrium (i.e., zero acceleration). We are assuming the triangle has a constant depth into and out of the page. Panel (a) shows traction upon one of the surfaces. This surface has unit normal **n** and unit vector parallel **p**. We say that the traction vector has a *normal stress* magnitude of s in the unit normal **n**-direction and a *shear stress* magnitude of t in the unit parallel **p**-direction. For equilibrium, there must be surface forces acting on the other two sides of the triangle so that the sum of the forces in each orthogonal direction is zero. Figure 1.3 panel (c) shows components of shear and normal stress on the other two surfaces of the triangle, along with the traction vector components on the third surface, in the x_1- and x_2-directions. We can determine the relative areas of the sides of the triangle through the angle θ as seen in panel (b) of Figure 1.3. The subscripts of the stress tensor components σ_{ij} should be noted here. The first subscript indicates the coordinate axis that is normal to the surface element on which the stress is acting, while the second subscript indicates the direction of the stress component. Therefore, summing the forces in the x_1-

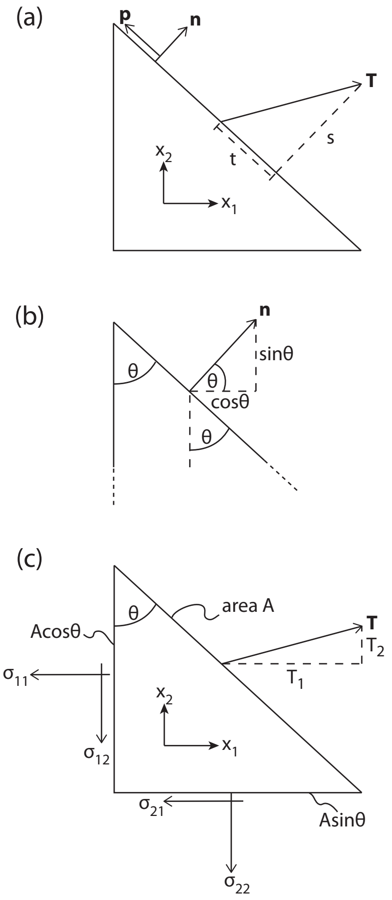

Figure 1.3: (a) A small right triangle, with constant depth into and out of the page, is subjected to traction **T** on the largest side. (b) The unit normal vector **u** can be decomposed into a sine and cosine term. (c) Stress components are introduced onto the other two sides of the triangle.

and x_2- directions, respectively, results in

$$\sigma_{11} A \cos\theta + \sigma_{21} A \sin\theta = T_1 A$$

$$\sigma_{12} A \cos\theta + \sigma_{22} A \sin\theta = T_2 A.$$

We can divide the equations above by area A to get

$$\sigma_{11} \cos\theta + \sigma_{21} \sin\theta = T_1$$

$$\sigma_{12} \cos\theta + \sigma_{22} \sin\theta = T_2.$$

We can see from panel (b) of Figure 1.3 that the normal vector can be decomposed into an $n_1 = cos\theta$ component along the x_1-axis and an $n_2 = sin\theta$ component along the x_2-axis. Thus, we can write the equation above as

$$\sigma_{11}n_1 + \sigma_{21}n_2 = T_1$$

$$\sigma_{12}n_1 + \sigma_{22}n_2 = T_2.$$

We can write this system of linear equations in matrix form as

$$\begin{bmatrix} \sigma_{11} & \sigma_{21} \\ \sigma_{12} & \sigma_{22} \end{bmatrix} \begin{Bmatrix} n_1 \\ n_2 \end{Bmatrix} = \begin{Bmatrix} T_1 \\ T_2 \end{Bmatrix}$$

In summation notation (tensor notation), this can be written as

$$T_j = \sigma_{ij}n_i. \tag{1.3}$$

Additionally, it can be shown that if there is zero torque on the triangle about the x_3-axis, $\sigma_{12} = \sigma_{21}$ (e.g., Stein and Wysession, 2003). In general, the stress tensor is *symmetric* (i.e., $\sigma_{ij} = \sigma_{ji}$). Therefore, it is common practice to also write

$$T_j = \sigma_{ji}n_i$$

or in vector form as

$$\mathbf{T} = \boldsymbol{\sigma} \cdot \mathbf{n}.$$

We have seen that the traction vector **T** is related to the unit normal vector **n** via the stress tensor $\boldsymbol{\sigma}$ in 2-D. The stress tensor generalizes to 3 spatial dimensions. In fact, because stress can be described as a tensor (of rank 2), the state of stress does not change in different Cartesian coordinate systems. Note that the *components* of the stress tensor can change between different coordinate systems, but the *state* of stress remains invariant.

The 3-D stress tensor, made up of both normal and shearing components (and noting that this tensor is symmetric), is

$$\boldsymbol{\sigma} = \begin{bmatrix} \sigma_{11} & \sigma_{12} & \sigma_{13} \\ \sigma_{21} & \sigma_{22} & \sigma_{23} \\ \sigma_{21} & \sigma_{22} & \sigma_{23} \end{bmatrix}. \tag{1.4}$$

Thus, the stress tensor has nine components, and represents the state of stress at a point. In Figure 1.4 a small cube demonstrates the stress tensor in Cartesian coordinates. Note that the stress tensor is defined to act on a point in space, and as the cube shrinks to zero size, the state of stress is defined by nine components. It is worthwhile to learn the sign convention for the stress tensor components. If the surface that the component acts on has an outward-unit normal vector that is in the positive direction for that axis, then each stress component on that face will be positive in the axis-positive direction. If the surface that the component acts on has an outward-unit normal vector that is in the negative direction for that axis, then each stress component on that face will be positive in the axis-negative direction. Figure 1.4 shows all positive components. Take, for example, σ_{32} on the top face of the small cube in Figure 1.4. The unit vector for that face points in the positive x_3-axis direction, and so a positive value for σ_{32} would point in the positive x_2-axis direction. For the bottom face of the cube, the unit vector for that face points in the negative x_3-axis direction, and so a positive value for σ_{32} would point in the negative x_2-axis direction. Note that Figure 1.3 utilized this convention when summing the forces and setting them equal to zero for equilibrium.

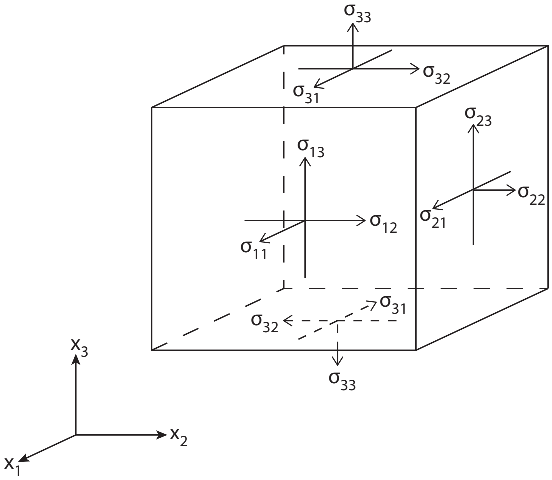

Figure 1.4: Stresses acting on a small cube.

1.1.4 Conservation of Momentum

We will use Newton's second law to express conservation of momentum. More specifically, the rate of change of momentum is equal to the sum of forces acting on some body. Let $\mathbf{f}$ be the vector that represents the body forces per unit mass. Then the sum of the body forces over the body will be $\int_V \rho\mathbf{f}\,dV$. Now let $\mathbf{T}$ be the surface vector that represents the surface force per unit area. Then the sum of the surface forces acting over surface S (that contains the body) will be $\int_S \mathbf{T}\,dS$. Additionally, the total change of momentum of the body is $\frac{d}{dt}\int_V \rho\mathbf{v}\,dV = \int_V \rho\mathbf{a}\,dV$, where $\mathbf{v}$ is the velocity vector for each small summed volume, and $\mathbf{a}$ is the acceleration vector for each small summed volume. Note that we have assumed that the mass of the object does not change, and that the function $\rho\mathbf{v}$ in the integral is continuous over the volume of the body. If we equate this change in momentum to the sum of all external forces acting on the body of mass M we have

$$\int_V \rho\mathbf{a}\,dV = \int_S \mathbf{T}\,dS + \int_V \rho\mathbf{f}\,dV.$$

This vector form can be transferred into tensor form:

$$\int_V \rho a_j\,dV = \int_S T_j\,dS + \int_V \rho f_j\,dV.$$

By utilizing our previous discussion of traction being the sum of stresses multiplied by corresponding normal vector components (see eq. 1.3), the equation above becomes

$$\int_V \rho a_j\,dV = \int_S \sigma_{ij} n_i\,dS + \int_V \rho f_j\,dV.$$

The first term on the right hand side (RHS) of the above equation can be changed into a volume integral via the Divergence theorem: $\int_S a_i n_i\,dS = \int_V \frac{\partial a_i}{\partial x_i}\,dV$, where a is some field variable. Therefore the equation above becomes

$$\int_V \rho a_j\,dV = \int_V \frac{\partial \sigma_{ij}}{\partial x_i}\,dV + \int_V \rho f_j\,dV.$$

All of these volume integrals could be collected and placed on the left hand side (LHS) with the RHS being zero. And since we chose the volume arbitrarily, the integrands must sum to zero. Therefore, we can use the integrands in the above equation to form

$$\rho a_j = \frac{\partial \sigma_{ij}}{\partial x_i} + \rho f_j. \tag{1.5}$$

This equation relates the acceleration (in the x_j-direction) to the gradient of stress (a stress component in the x_j-direction) and the body forces (in the x_j-direction). It is often referred to as the *equation of motion*, or the *equation of equilibrium* when ρa_j is set to zero (e.g., Sokolnikoff, 1956).

1.1.5 A Constitutive Relationship for Stress and Strain

For *linearly elastic* materials the stress tensor is linearly related to the strain tensor if the value of strain is relatively small (so that the material can rebound, elastically, and return to its original shape). The justification for this concept is through experimentation. More specifically, the stress tensor σ_{ij} is linearly related to the strain tensor e_{kl} through the fourth-rank tensor c_{ijkl} $(i, j, k, l = \{1, 2, 3\})$ by

$$\sigma_{ij} = c_{ijkl} \frac{1}{2} \left(\frac{\partial u_k}{\partial x_l} + \frac{\partial u_l}{\partial x_k} \right) = c_{ijkl} e_{kl}. \tag{1.6}$$

This is referred to as a generalized *Hooke's law.* It is approximately valid for values of strains in the Earth up to 10^{-4} (strain is unitless!) (e.g., Stein and Wysession, 2003). The fourth-rank tensor c_{ijkl}, with 3^4 components, can be simplified by noting symmetry and isotropic conditions. Since c_{ijkl} is a map from stress to strain, and since the stress and strain tensors are symmetric, c_{ijkl} is minor-symmetric with $c_{ijkl} = c_{jikl}$ and $c_{ijkl} = c_{ijlk}$ (e.g., Hughes, 2000). This symmetry reduces the number of elastic constants from 81 to 36. Now, since c_{ijkl} is minor-symmetric with respect to the indices k and l, we can write the equation above as

$$\sigma_{ij} = c_{ijkl} e_{kl} = c_{ijkl} \frac{\partial u_k}{\partial x_l}. \tag{1.7}$$

Now we can use this form of Hooke's law to re-write the equation of motion (eq. 1.5) as

$$\rho a_j = \frac{\partial}{\partial x_i} \left(c_{ijkl} \frac{\partial u_k}{\partial x_l} \right) + \rho f_j. \tag{1.8}$$

This form of the equation of motion is the starting basis for many finite element techniques in linearly elastostatic (i.e., the ρa_j term is set to zero) and elastodynamic analysis (Hughes, 2000). Furthermore, if there are no body forces acting then we get

$$\rho \frac{\partial^2 u_j}{\partial t^2} = \frac{\partial}{\partial x_i} \left(c_{ijkl} \frac{\partial u_k}{\partial x_l} \right) \tag{1.9}$$

where we have replaced the acceleration term with the second time derivative of displacement. This form of the equation of motion provides us with some physical intuition about the outcome of conservation of momentum and Hooke's law. In fact, this familiar form is a wave equation since it relates time derivatives of displacement to spatial derivatives of displacement. In seismology, the propagation of seismic waves far from the earthquake fault can be described by this equation (e.g., Shearer, 2009). Note that we say this is appropriate far from the fault since equivalent body forces (forces that produce the same displacement field as that of fault slip) must be modeled when considering fault motion (e.g., Shearer, 2009). It is very interesting that, by combing Newton's second law with Hooke's law, we ultimately get wave motion!

Strain energy considerations (e.g., Sokolnikoff, 1956; Aki and Richards, 2009) result in major-symmetry of c_{ijkl} with $c_{ijkl} = c_{klij}$ (Hughes, 2000) that further reduces the number of elastic constants to 21. Lastly, isotropic (independence of direction) conditions further reduce the number of constants to 2. Under these assumptions (e.g., Shearer, 2009),

$$c_{ijkl} = \lambda \delta_{ij} \delta_{kl} + G(\delta_{ik} \delta_{jl} + \delta_{il} \delta_{jk})$$

where δ_{ij} is the Kronecker delta and where λ and G (i.e., the 2 elastic constants) are referred to as *elastic moduli* since they relate stress to displacement. λ is *Lamé's first parameter*, while G is the *shear modulus* (that is also referred to as *Lamé's second parameter*). The values of these parameters need to be determined experimentally. We can write the isotropic form of Hooke's law as (e.g., Shearer, 2009)

$$\begin{aligned}\sigma_{ij} &= c_{ijkl}e_{kl} = \left[\lambda\delta_{ij}\delta_{kl} + G(\delta_{ik}\delta_{jl} + \delta_{il}\delta_{jk})\right] e_{kl} \\ &= \lambda\delta_{ij}e_{kk} + G(e_{ij} + e_{ji}) = \lambda\delta_{ij}e_{kk} + 2Ge_{ij}\end{aligned} \tag{1.10}$$

where we have utilized only non-zero contributions that result from the Kronecker delta function as well as the symmetry of the strain tensor.

1.1.6 Physical Boundary Conditions on Faults and on Earth's Surface

It is well known that earthquake ruptures are controlled by friction on faults. The general friction equation for a point on an interface (e.g., fault surface) without cohesion (bonding) is:

$$\tau \leq \mu\sigma_{\text{eff}} \tag{1.11}$$

where τ is the shear stress, μ is the friction coefficient, and σ_{eff} is the effective normal stress that is taken to be positive in compression on the surface. When the shear stress at that point becomes equal to the friction coefficient multiplied by the normal stress, sliding commences that relieves (reduces) the shear stress at that same point. Before, during, and after this process the friction coefficient and effective normal stress may also change. When the shear stress is smaller than the product of the former two, sliding ceases. For earthquakes this is a quasi-periodic process that helps explain why earthquakes occur every so many years along the same faults, but with some level of unpredictability in time. It is intuitive that kinetic coefficients of friction are often smaller than their static counterparts – sliding a heavy cardboard box across a slick household floor demonstrates this. Initially it is more difficult to move, but once the box begins sliding it becomes easier to push. The nature of such coefficients of friction has been explored in the laboratory for many years (e.g., Rabinowicz, 1951).

One such friction formulation that describes this observation and has been used in numerical modeling is linear slip-weakening friction (e.g., Ida, 1972; Andrews, 1976):

$$\mu = \begin{cases} \frac{\mu_k - \mu_s}{d_0} u + \mu_s, & \text{if } u < d_0 \\ \mu_k, & \text{if } u \geq d_0 \end{cases} \tag{1.12}$$

where u is total displacement (i.e., slip on a fault) and d_0 is a slip distance over which the friction coefficient μ drops from its static value μ_s to its kinetic value μ_k; d_0 is referred to as the *effective slip-weakening distance*. For computational studies, a nonzero value of d_0 is necessary to resolve the (shear) stress drop (i.e., rupture front) process accurately and with stability. It is also a reasonable physical assumption, since energy being focused by seismic waves driving rupture is probably not focused at a single point, but a finite volume (Andrews, 1976), leading to an apparent fracture (i.e., dissipated) energy associated with that finite volume during the onset of fault slip. Additionally, laboratory studies on rock friction show gradual stress drops (e.g., Dieterich, 1978, 1979). Andrews (1976) was a pioneer in using a linear slip-weakening formulation to model spontaneous earthquake rupture in 2-D.

Another friction formulation, that is similar to linear slip-weakening friction, is linear time-weakening friction (Andrews, 2004):

$$\mu = \begin{cases} \frac{\mu_k - \mu_s}{t_0} t + \mu_s, & \text{if } t < t_0 \\ \mu_k, & \text{if } t \geq t_0 \end{cases} \tag{1.13}$$

where t is total time during slip and t_0 is a time over which the friction coefficient μ drops from its static value μ_s to its kinetic value μ_k, and where t_0 can be referred to as the *effective time-weakening interval.* A linear time-weakening friction law can be a useful numerical tool. Since stress drop must be resolved in time and space to produce numerically stable and accurate results, one can specify t_0 directly to do so. In fact, since earthquake ruptures travel at roughly the S-wave speed, one can ensure that the rupture front is spread out over three to four spatial (modeling) intervals by making t_0 equal to the time that it takes for an S-wave to travel across three to four spatial elements.

More complex and realistic friction formulations have also been developed from laboratory experimentation. One such formulation is rate- and state-dependent friction (Dieterich, 1978, 1979; Ruina, 1983). Dieterich (1978) shows, through experiments and analysis of a spring slider system, that the friction coefficient of rock varies with time and slip velocity. More specifically, the static friction increases with stationary contact time, and the kinetic friction also changes with the contact time of sliding asperities – small contact surfaces across the fault that are continually sliding into and out of existence – as well as with slip velocity history. Dieterich (1979) further shows through laboratory experiments that an increase in slip speed leads to an abrupt increase in frictional strength, after which the frictional strength falls toward a steady (kinetic) value. Using the constitutive relations proposed by Dieterich (1978, 1979), Ruina (1983) formulated state variable friction laws that include the time and velocity dependence of friction coefficient. The general form of the rate- and state-dependent friction law is:

$$\tau = \left[\mu_0 + aln\left(\frac{V}{V_0}\right) + bln\left(\frac{\theta}{\theta_0}\right)\right]\sigma_{\text{eff}} \tag{1.14}$$

where μ_0 represents a constant reference value for the coefficient of friction; a and b are constitutive parameters estimated from laboratory experiments; V_0 and θ_0 are reference values for slip rate and the state of the sliding surface, respectively; θ can be thought of as the average age of contacts at some constant sliding velocity, and the bracketed term is the friction coefficient. Note that for an increase in sliding velocity V there is a corresponding increase in friction, and as sliding velocity grows the asperities are in contact for smaller amounts of time, making θ small and ultimately decreasing friction. Later, Linker and Dieterich (1992) further developed the rate-state framework to include the friction coefficient's dependence on normal stress. They found that increases in normal stress led to decreases in the state variable θ and decreases in normal stress led to increases in θ. This result indicates that the friction coefficient at least partially compensates (acts in the opposite direction) for changes in normal stress.

Since shear stress during sliding depends on the friction coefficient (and the normal stress) as seen in the equations above, the functional form of frictional weakening is directly related to the earthquake rupture energy budget (e.g., Andrews, 1976; Kanamori and Rivera, 2006). The total energy of the earthquake can be split into three categories: fracture energy, energy expended against friction (i.e., heat energy), and radiated seismic energy (see Figure 1.5). Figure 1.5 shows a simplified energy budget schematic for earthquakes and how it is related to the functional form of shear stress evolution, where τ_0 is the initial shear stress; τ_y is the yield shear stress; τ_f is the final shear stress; d_0 is the effective slip-weakening distance, and d_f is the final amount of slip. We note that radiated energy density should be thought of as an average over the entire fault; the contributed radiated energy density from

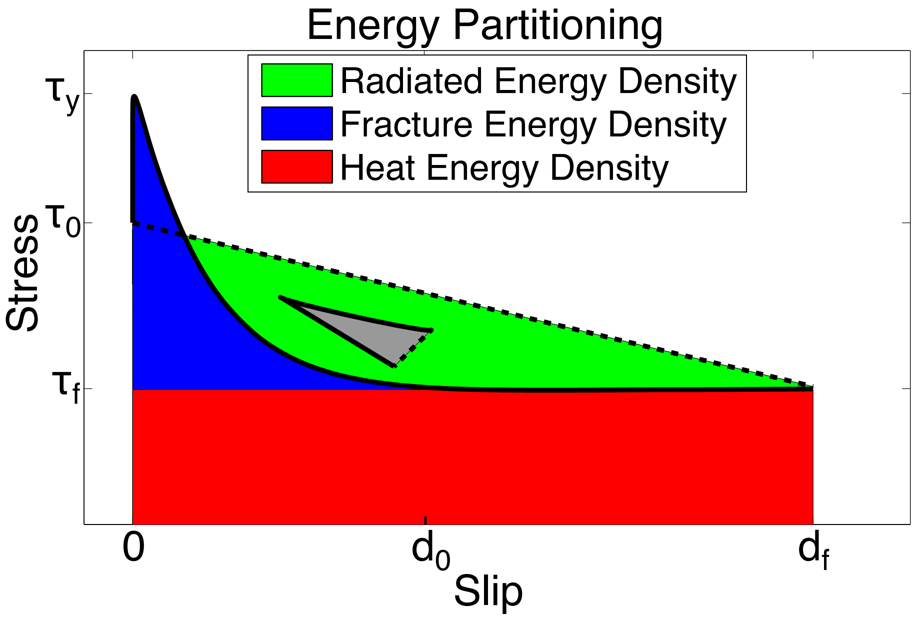

Figure 1.5: A simplified schematic of energy partitioning for an earthquake. The solid black line indicates shear stress with slip at a point on the fault. The gray "triangle" within the radiated energy density indicates the full subtraction of the fracture energy density from the total energy budget (the area under the dashed line). Note that the Figure shows a nonlinear weakening curve for generality. In general, different friction laws produce different weakening curve geometries. Figure from Ryan and Oglesby, (2014).

a single point cannot be determined easily from stress-versus-slip weakening curves since rupture along portions of the fault sends radiation to other portions of the fault. In other words, during rupture complex stress-wave interactions occur so that energy is transferred amongst parts of the fault. However, fracture and frictional energy are dissipated at points along the fault, making those easily measurable from models.

In addition to friction on the fault surface, it is important to consider the boundary conditions at the Earth's surface in earthquake modeling. Numerical implementations of these boundary conditions often assume that the atmosphere and ocean are nonexistent, and that the Earth's surface is a *free* surface in that it is the boundary between solid material and a vacuum. If the Earth's surface is represented by the top surface of the cube in Figure

1.4, then $\sigma_{31} = \sigma_{32} = \sigma_{33} = 0$. In other words, there is no traction at the surface since there is no surface force compressing, extending, or shearing that surface (if the surface is free, there is nothing there to supply such a force!). Such a boundary condition ultimately alters stress transfer during an earthquake, and thus can produce significant effects on the rupture process and final displacement field (e.g., Oglesby et al., 1998).

1.2 Fluid Mechanics: Key Concepts in Modeling Tsunamis

1.2.1 Lagrangian and Eulerian specifications

The continuum hypothesis is utilized for fluid mechanics in the same way it is for solid mechanics. Therefore, it is valid here under the same assumptions stated within the solid mechanics section above. Eulerian or Lagrangian reference frames can both be used to describe flow fields. Within the Eulerian frame of reference a fixed region, in space, is observed as different particles travel through it in time. Within the Lagrangian frame of reference a fluid mass is followed as it flows (i.e., changes shape and location). A simple analogy involves a cat observing a large fish tank that contains many fish. If the cat continuously observes a fixed region of the tank as different fish pass by, that is an Eulerian specification. If the cat follows a single fish as it moves about the tank, that is a Lagrangian specification. We utilize both of these reference frames to describe some of the following key formulas. A control or representative volume is used in both frameworks. In the Eulerian framework the fixed region is the control volume, while in the Lagrangian framework the control volume consists of the fluid mass being followed.

It is worth noting that a common notation for the *velocity* vector in fluid mechanics is $\mathbf{u} = (u, v, w)$, where where u, v, and w represent the velocity components in the x, y, and z directions, respectively. We use this convention here. It should not be confused with the displacement variable u in solid mechanics!

1.2.2 Material Derivative

Let α be some field variable (e.g., density) of a material. For a small amount of time δt, a specific volume element in the Lagrangian framework will travel a small distance represented by $\delta x, \delta y, \delta z$. Therefore, a small change in α is represented by the following total change (this is analogous to the total difference from calculus):

$$\delta\alpha \approx \frac{\partial\alpha}{\partial t}\delta t + \frac{\partial\alpha}{\partial x}\delta x + \frac{\partial\alpha}{\partial y}\delta y + \frac{\partial\alpha}{\partial z}\delta z.$$

Dividing through by δt results in:

$$\frac{\delta\alpha}{\delta t} \approx \frac{\partial\alpha}{\partial t} + \frac{\delta x}{\delta t}\frac{\partial\alpha}{\partial x} + \frac{\delta y}{\delta t}\frac{\partial\alpha}{\partial y} + \frac{\delta z}{\delta t}\frac{\partial\alpha}{\partial z}.$$

In the limit as $\delta t \to 0$, we see that $\frac{\delta x}{\delta t} \to u$, $\frac{\delta y}{\delta t} \to v$, $\frac{\delta z}{\delta t} \to w$ where u, v, and w represent the velocity components in the x, y, and z directions, respectively. Thus, we obtain the total time derivative of α:

$$\frac{D\alpha}{Dt} = \frac{\partial\alpha}{\partial t} + u\frac{\partial\alpha}{\partial x} + v\frac{\partial\alpha}{\partial y} + w\frac{\partial\alpha}{\partial z}.$$

This Lagrangian formulation of the total time derivative (of a field variable) is known as the *material derivative.* In fact, this equation relates the Lagrangian framework on the LHS to the Eulerian derivatives on the RHS. In vector form this equation can be written as

$$\frac{D\alpha}{Dt} = \frac{\partial\alpha}{\partial t} + (\mathbf{u} \cdot \boldsymbol{\nabla})\alpha,$$

and in tensor notation as

$$\frac{D\alpha}{Dt} = \frac{\partial \alpha}{\partial t} + u_k \frac{\partial \alpha}{\partial x_k}. \tag{1.15}$$

1.2.3 Reynolds' Transport Theorem

Application of the conservation principles that follow result in an integro-differential equation of the form

$$\int_V L\alpha \, dV = 0$$

where L is some differential operator and α is some set of material properties (e.g., density, velocity, etc.). If the control volume V is arbitrarily chosen, then it follows that the integrand must be zero (i.e., $L\alpha = 0$).

By considering an arbitrary control volume in the Lagrangian reference frame we can elegantly derive conservation equations. However, we need the ability to transform between volume integrals in the Lagrangian and Eulerian specifications. This can be done with Reynolds' Transport Theorem. In the Lagrangian reference frame the total time derivative of some property α integrated over some arbitrary control volume V is

$$\frac{D}{Dt}\int_{V(t)} \alpha(t)\, dV = \lim_{\delta t \to 0} \left\{ \frac{1}{\delta t} \left[\int_{V(t+\delta t)} \alpha(t+\delta t)\, dV - \int_{V(t)} \alpha(t)\, dV \right] \right\}.$$

If we add and subtract the quantity $\alpha(t+\delta t)$ integrated over the control volume V at time t we get

$$\begin{aligned}\frac{D}{Dt}\int_{V(t)} \alpha(t)\, dV = \lim_{\delta t \to 0} \Bigg\{ & \frac{1}{\delta t} \left[\int_{V(t+\delta t)} \alpha(t+\delta t)\, dV - \int_{V(t)} \alpha(t+\delta t)\, dV \right] \\ & + \frac{1}{\delta t} \left[\int_{V(t)} \alpha(t+\delta t)\, dV - \int_{V(t)} \alpha(t)\, dV \right] \Bigg\}.\end{aligned}$$

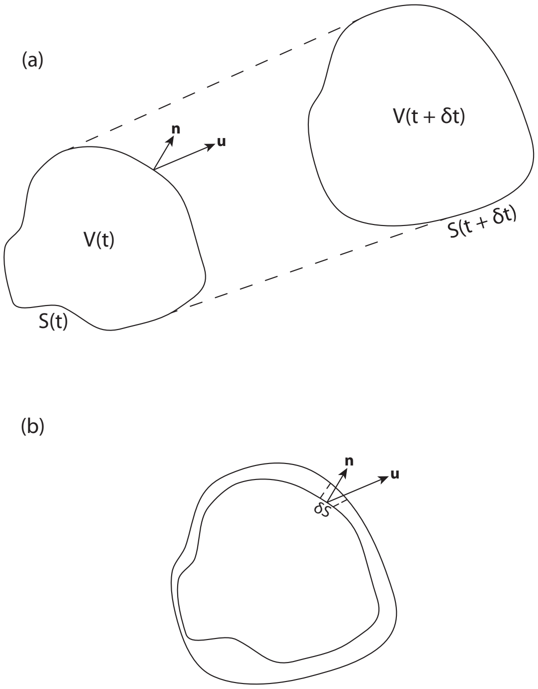

Figure 1.6: (a) Control volume V (surrounded by surface S) at time t and at some later time $t + \delta t$. Note that the distance moved by the control volume within the time interval δt is exaggerated. (b) Control volume at different times superimposed on one another. Vectors $\mathbf{u}$ and $\mathbf{n}$ indicate the velocity and unit normal at a surface point, and a small surface piece in indicated by δS.

The first two integrals on the RHS involve the same integrand but different integration volumes, while the last two integrals involve different integrands but the same integration volumes. Thus, we can group each pair of integrals correspondingly:

$$\begin{aligned}\frac{D}{Dt}\int_{V(t)} \alpha(t)\,dV = \lim_{\delta t \to 0} \Bigg\{ & \frac{1}{\delta t}\left[\int_{V(t+\delta t)-V(t)} \alpha(t+\delta t)\,dV\right] \\ & + \frac{1}{\delta t}\left[\int_{V(t)} \left(\alpha(t+\delta t) - \alpha(t)\right) dV\right]\Bigg\}.\end{aligned}$$

Since the last integral has integration limits that are independent of δt we can bring the $\frac{1}{\delta t}$

into the integration producing

$$\frac{D}{Dt}\int_{V(t)}\alpha(t)\,dV = \lim_{\delta t\to 0}\left\{\frac{1}{\delta t}\left[\int_{V(t+\delta t)-V(t)}\alpha(t+\delta t)\,dV\right]\right.$$
$$\left.+\left[\int_{V(t)}\frac{\alpha(t+\delta t)-\alpha(t)}{\delta t}\,dV\right]\right\}.$$

In the limit as $\delta t \to 0$ the last term being integrated can now be seen to be the Eulerian time derivative of α:

$$\frac{D}{Dt}\int_{V(t)}\alpha(t)\,dV = \lim_{\delta t\to 0}\left\{\frac{1}{\delta t}\left[\int_{V(t+\delta t)-V(t)}\alpha(t+\delta t)\,dV\right]\right\}+\int_{V(t)}\frac{\partial\alpha}{\partial t}\,dV.$$

The first integral on the RHS can be transformed into a surface integral in the following way. As the control volume $V(t)$ moves it changes size and shape into $V(t+\delta t)$ (see Figure 1.6). A small surface area δS on surface $S(t)$ that surrounds $V(t)$ has velocity $\mathbf{u}$ and an outward normal vector $\mathbf{n}$; therefore, the perpendicular distance between small surface elements on $S(t)$ and $S(t+\delta t)$ is $\mathbf{u}\cdot\mathbf{n}\delta t$. Thus, a small surface area δS will correspond to a volume change of $\delta V \approx \mathbf{u}\cdot\mathbf{n}\delta t\delta S$, or in the limit as $\delta S \to 0$, $dV = \mathbf{u}\cdot\mathbf{n}\delta t dS$. We can therefore replace dV in the first integral on the RHS in the equation above with $\mathbf{u}\cdot\mathbf{n}\delta t dS$ (and noting that the integration will now be over a surface for each δt) to get

$$\frac{D}{Dt}\int_{V(t)}\alpha(t)\,dV = \lim_{\delta t\to 0}\left\{\frac{1}{\delta t}\left[\int_{S(t)}\alpha(t+\delta t)\mathbf{u}\cdot\mathbf{n}\delta t\,dS\right]\right\}+\int_{V(t)}\frac{\partial\alpha}{\partial t}\,dV.$$

and canceling out the δt values for the first term on the RHS we have

$$\begin{aligned}\frac{D}{Dt}\int_{V(t)}\alpha(t)\,dV &= \lim_{\delta t\to 0}\left\{\left[\int_{S(t)}\alpha(t+\delta t)\mathbf{u}\cdot\mathbf{n}\,dS\right]\right\}+\int_{V(t)}\frac{\partial\alpha}{\partial t}\,dV\\ &= \int_{S(t)}\alpha(t)\mathbf{u}\cdot\mathbf{n}\,dS+\int_{V(t)}\frac{\partial\alpha}{\partial t}\,dV.\end{aligned}$$

This result is Reynolds' Transport Theorem. We can see that this result allows us to recast the material derivative of an integrated quantity into other integrated quantities (where the differential operator is now within an integral). However, we need to get this equation into a more useable form via this form of the Divergence theorem:

$$\int_{S(t)} \alpha(t)\mathbf{u}\cdot\mathbf{n}\,dS = \int_{V(t)} \boldsymbol{\nabla}\cdot(\alpha\mathbf{u})\,dV.$$

We can insert the RHS of the above equation into the previous equation to obtain

$$\frac{D}{Dt}\int_{V(t)} \alpha(t)\,dV = \int_{V(t)} \left[\frac{\partial\alpha}{\partial t} + \boldsymbol{\nabla}\cdot(\alpha\mathbf{u})\right] dV$$

or, in tensor notation as

$$\frac{D}{Dt}\int_{V(t)} \alpha(t)\,dV = \int_{V(t)} \left[\frac{\partial\alpha}{\partial t} + \frac{\partial}{\partial x_k}(\alpha u_k)\right] dV. \tag{1.16}$$

We will now use this form of the Reynolds' Transport Theorem to demonstrate the conservation of mass and momentum for a specific mass in the Lagrangian framework.

1.2.4 Conservation of Mass

For a specific control volume V, the mass is $\int_V \rho\,dV$, where ρ is the density of a single fluid. Thus, the conservation of mass in the Lagrangian framework can be expressed as

$$\frac{D}{Dt}\int_V \rho\,dV = 0.$$

Using Reynolds' Transport Theorem (eq. 1.16) we see that the above equation is equal to

$$\int_V \left[\frac{\partial\rho}{\partial t} + \frac{\partial}{\partial x_k}(\rho u_k)\right] dV = 0.$$

Since the control volume is chosen arbitrarily, the integrand above must be zero:

$$\frac{\partial\rho}{\partial t} + \frac{\partial}{\partial x_k}(\rho u_k) = 0. \tag{1.17}$$

This is called the *continuity equation* since it involves a partial derivative of velocity; thus, the velocity is assumed to be continuous. Expanding this equation via the chain rule we get

$$\frac{\partial \rho}{\partial t} + u_k \frac{\partial \rho}{\partial x_k} + \rho \frac{\partial u_k}{\partial x_k} = 0.$$

The first two terms on the LHS are the Eulerian form of the material derivative (eq. 1.15), so we can replace them by the Lagrangian form of the material derivative to get

$$\frac{D\rho}{Dt} + \rho \frac{\partial u_k}{\partial x_k} = 0.$$

However, if we now ignore variations in density we can make a further simplification to the equation above. So we consider a single fluid of a single phase. For a constant density and constant mass of a control volume, the volume must remain the same. Therefore, we can regard the fluid as *incompressible*. No variation in density is described by

$$\frac{D\rho}{Dt} = 0.$$

Thus, the continuity equation for an incompressible fluid is

$$\frac{\partial u_k}{\partial x_k} = \boldsymbol{\nabla} \cdot \mathbf{u} = 0. \tag{1.18}$$

1.2.5 Conservation of Momentum

Now we will make use of Newton's second law as well as information discussed thus far to express conservation of momentum for flows. More specifically, the rate of change of momentum is equal to the sum of forces acting on some mass (i.e., the control volume). Let $\mathbf{f}$ be the vector that represents the body forces per unit mass. Then the sum of the body forces over the control volume will be $\int_V \rho \mathbf{f} \, dV$. Now let $\mathbf{T}$ be the surface vector that represents the surface force per unit area. Then the sum of the surface forces acting over surface S (that contains V) will be $\int_S \mathbf{T}\, dS$. Additionally, the momentum contained in the control volume is $\int_V \rho\mathbf{u}\, dV$ and the change of momentum in the Lagrangian reference frame is $\frac{D}{Dt}\int_V \rho\mathbf{u}\, dV$. If we equate this change in momentum to the sum of all external forces acting on the mass we have

$$\frac{D}{Dt}\int_V \rho\mathbf{u}\, dV = \int_S \mathbf{T}\, dS + \int_V \rho\mathbf{f}\, dV.$$

This vector form can be transferred into tensor form by utilizing our previous discussion of traction being the sum of stresses multiplied by corresponding normal vector components (see eq. 1.3). Thus, the above equation becomes

$$\frac{D}{Dt}\int_V \rho u_j\, dV = \int_S \sigma_{ij} n_i\, dS + \int_V \rho f_j\, dV.$$

The LHS can be replaced using Reynolds' transport theorem (eq. 1.16) using ρu_j in place of α. The first term on the RHS can be changed to a volume integral via the Divergence theorem. Therefore the equation above becomes

$$\int_V \left[\frac{\partial(\rho u_j)}{\partial t} + \frac{\partial}{\partial x_k}(\rho u_j u_k)\right] dV = \int_V \frac{\partial \sigma_{ij}}{\partial x_i}\, dV + \int_V \rho f_j\, dV.$$

All of these volume integrals could be collected and placed on the LHS with the RHS being zero. And since we chose the control volume arbitrarily, the integrands must sum to zero. Therefore, we can use the integrands in the above equation to form the following:

$$\frac{\partial(\rho u_j)}{\partial t} + \frac{\partial}{\partial x_k}(\rho u_j u_k) = \frac{\partial \sigma_{ij}}{\partial x_i} + \rho f_j.$$

The first term on the LHS can be expanded via the chain rule. The second term on the LHS can also be expanded using the chain rule and by considering $\rho u_j u_k$ to be the product of ρu_k and u_j.

$$\rho\frac{\partial u_j}{\partial t} + u_j\frac{\partial \rho}{\partial t} + u_j\frac{\partial}{\partial x_k}(\rho u_k) + \rho u_k\frac{\partial u_j}{\partial x_k} = \frac{\partial \sigma_{ij}}{\partial x_i} + \rho f_j.$$

The second and third terms on the LHS in the equation above sum to zero since they are the continuity equation (eq. 1.17) multiplied by u_j. Finally, the nonlinear equation that expresses the conservation of momentum for a fluid can be written as

$$\rho\frac{\partial u_j}{\partial t} + \rho u_k\frac{\partial u_j}{\partial x_k} = \frac{\partial \sigma_{ij}}{\partial x_i} + \rho f_j. \tag{1.19}$$

The first term on the LHS is the familiar acceleration due to velocity change with time. The second term on the LHS represents a spatial acceleration (i.e., a convective term). The RHS involves spatial gradients of stress and body forces, both of which contribute the net external forces on the mass.

1.2.6 A Constitutive Relationship for Stress and Rate of Strain

For *Newtonian fluids* the stress tensor is linearly related to the rate of strain tensor. In other words, viscous stresses – that arise during flow – are linearly proportional to the deformation rate for certain fluids under certain conditions. The justification for this concept is through experimentation. Under many conditions, water is one example of a Newtonian fluid. More specifically, the *deviatoric* stress tensor τ_{ij} (deviation from static pressure) is linearly related to the rate of strain tensor $\dot{e}_{ij}$ through the fourth-rank tensor c_{ijkl} $(i, j, k, l = \{1, 2, 3\})$ by

$$\tau_{ij} = c_{ijkl}\frac{1}{2}\left(\frac{\partial u_k}{\partial x_l} + \frac{\partial u_l}{\partial x_k}\right) = c_{ijkl}\dot{e}_{kl}.$$

The fourth-rank tensor c_{ijkl}, with 3^4 elements, can be simplified by noting isotropic conditions and that the deviatoric stress tensor is related to the rate of strain tensor (not the rotation tensor). The most general isotropic fourth-rank tensor has 3 independent scalar coefficients (e.g., Currie, 2013); and the rate of strain tensor (which is symmetric) requires that c_{ijkl} be minor-symmetric with $c_{ijkl} = c_{ijlk}$ (e.g., Hughes, 2000), further reducing the number of scalar coefficients from 3 to 2. Therefore, we have

$$\tau_{ij} = \lambda \delta_{ij} \frac{\partial u_k}{\partial x_k} + \mu \left(\frac{\partial u_i}{\partial x_j} + \frac{\partial u_j}{\partial x_i} \right)$$

where δ_{ij} is the Kronecker delta and where λ and μ (i.e., the 2 scalar coefficients) are referred to as viscosity coefficients since they relate stress to spatial derivatives of velocity. These parameters need to be determined experimentally. The full stress tensor needs to incorporate a static pressure term, and so it is of the form

$$\begin{aligned} \sigma_{ij} &= -p\delta_{ij} + \tau_{ij} \\ &= -p\delta_{ij} + \lambda \delta_{ij} \frac{\partial u_k}{\partial x_k} + \mu \left(\frac{\partial u_i}{\partial x_j} + \frac{\partial u_j}{\partial x_i} \right) \end{aligned} \tag{1.20}$$

where p is the pressure (that is negative in compression) in a fluid at rest. This equation along with the conservation of momentum equation (eq. 1.19) form the Navier-Stokes equations.

1.2.7 Velocity Potential and the Bernoulli Equation

Kelvin's theorem states that an ideal (i.e., inviscid and incompressible) flow that originates as irrotational will remain irrotational (the theorem is explained in more detail in fluid mechanics texts: e.g., Owczarek, 1968; Currie, 2013). Therefore, the vorticity vector $\boldsymbol{\omega}$ in the fluid will be zero. The vector $\boldsymbol{\omega}$ is defined by the curl of the velocity vector and so $\boldsymbol{\omega} = \boldsymbol{\nabla} \times \mathbf{u} = 0$. We also know that the curl of any gradient is zero, so we can write

$\boldsymbol{\omega} = \boldsymbol{\nabla} \times \boldsymbol{\nabla}\phi = 0$ where ϕ is referred to as the *velocity potential.* Thus, we choose

$$\mathbf{u} = \boldsymbol{\nabla}\phi.$$

If we regard the fluid as incompressible, then the continuity equation to be satisfied is eq. 1.18 and this gives us the Laplace equation

$$\nabla^2\phi = 0. \tag{1.21}$$

The momentum equation (eq. 1.19) may be simplified and integrated to yield the Bernoulli equation. Doing so requires that the fluid be inviscid (i.e., negligible viscosity with the viscosity coefficients μ and λ being zero), the body forces being conservative (i.e., the work done on a particle is independent of the path along which that particle moves), and the flow either being steady (unchanging with time) or irrotational. The Bernoulli equation with the irrotational assumption and with constant pressure $p = P$ is

$$\frac{\partial \phi}{\partial t} + \frac{P}{\rho} + \frac{1}{2}\boldsymbol{\nabla}\phi \cdot \boldsymbol{\nabla}\phi - G = F(t) \tag{1.22}$$

where G is a scalar function that is related to some body force $\mathbf{f}$ by $f_j = \frac{\partial G}{\partial x_j}$ and $F(t)$ is some function of time that results from an integrated term in the Bernoulli equation derivation under the stated assumptions (e.g., Dean and Dalrymple, 1991). Note that we can also write the Bernoulli equation in terms of velocity:

$$\frac{\partial \phi}{\partial t} + \frac{P}{\rho} + \frac{1}{2}\mathbf{u} \cdot \mathbf{u} - G = \frac{\partial \phi}{\partial t} + \frac{P}{\rho} + \frac{1}{2}\left(u^2 + v^2 + w^2\right) - G = F(t).$$

1.2.8 Small Amplitude, Long Wavelength Surface Waves in Shallow Water

Gravity waves on a liquid surface are an overarching topic here. This section demonstrates the basics of shallow water wave theory in 1-D, where the wave amplitude is along the z-axis and the wave propagation is along the x-axis. In doing so we go from general surface wave conditions to more specific assumptions that allow further simplification. As with many other areas in physics, one key aspect is clearly stating the problem to be solved as well as the assumptions to be made. We assume that liquid gravity waves are irrotational for our purposes; this follows from the assumption that a long period surface wave will have very small changes in the vertical velocity component with respect to the horizontal direction and vice versa (i.e., the velocity components satisfy the Laplace equation). If we assume zero vorticity and incompressibility, the Laplace equation (eq. 1.21) must be satisfied. We let the x-axis of the coordinate system be at the mean level of the free surface of the liquid, and the z-axis be the vertical axis (see Figure 1.7). The depth of the liquid is h. The amplitude of the wave is denoted by A, and the free surface is defined by $z = \eta(x,t)$ or $z - \eta = 0$.

Physical Boundary Conditions for Surface Gravity Waves

Perhaps the most important part of modeling physical processes is correctly determining and implementing physical boundary conditions. We describe the free surface (the water-air interface in this case) and the bottom surface (e.g., the water-ground interface) boundary conditions now. These boundary conditions, along with some assumptions, will

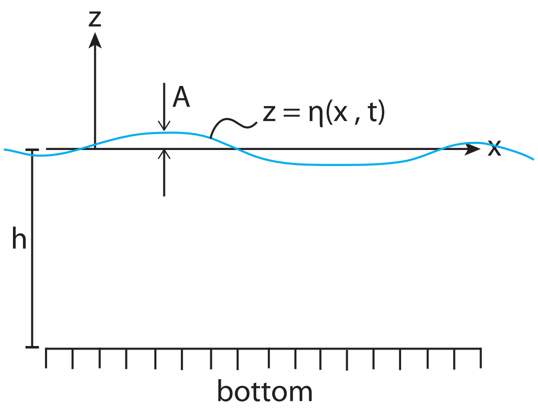

Figure 1.7: A snapshot of a liquid wave (blue curve) and corresponding coordinate system.

give us a frequency dispersion relation. The *kinematic* free surface boundary condition states that a particle of fluid on the free surface remains on that free surface with time, and thus

$$\frac{D}{Dt}(z-\eta)=0.$$

In other words, if we move with the free surface it does *not* change. In the Eulerian specification (using eq. 1.15) this becomes

$$\frac{\partial(z-\eta)}{\partial t}+(\mathbf{u}\cdot\boldsymbol{\nabla})(z-\eta)=0.$$

Since the z coordinate does not depend on time in the Eulerian framework (η does!), η depends only on x and t, and the spatial coordinates are independent of each other we have

$$-\frac{\partial\eta}{\partial t}-u\frac{\partial\eta}{\partial x}+w=0$$

where w is the velocity component (within the velocity vector $\mathbf{u}$) in the z-direction. Using the velocity potential ϕ we can then turn this equation into

$$\frac{\partial\eta}{\partial t}+\frac{\partial\phi}{\partial x}\frac{\partial\eta}{\partial x}=\frac{\partial\phi}{\partial z}. \tag{1.23}$$

We also need to specify a *dynamic* free surface boundary condition. Naturally, this involves specifying pressure on the free surface, which can be done with the irrotational Bernoulli equation (eq. 1.22) where the scalar function G is related to the force of gravity by $G = -gz = -g\eta$ on the free surface:

$$\frac{\partial \phi}{\partial t} + \frac{P}{\rho} + \frac{1}{2}\boldsymbol{\nabla}\phi \cdot \boldsymbol{\nabla}\phi + g\eta = F(t). \tag{1.24}$$

Lastly, the boundary condition at the bottom must also be imposed. We are assuming that the fluid/solid interface along the bottom is continuous (i.e., there are no voids along the bottom). This boundary condition is relatively intuitive, and for an inviscid fluid amounts to the velocity component that is normal to the bottom being zero at that location:

$$\frac{\partial \phi}{\partial z} = 0 \text{ on } z = -h. \tag{1.25}$$

We note that many boundary conditions for surface gravity waves are not described here, such as lateral boundary conditions that characterize long-period ocean waves as they approach and inundate coastlines and bottom boundary conditions that characterize wave formation and propagation. Additionally, other physical parameters such as bottom friction and geostrophic effects (e.g., the Coriolis effect) are not described here. The reader is referred to texts on marine geophysics (e.g., Dean and Dalrymple, 1991; Liu, 2009) and fluid mechanics (e.g., Currie, 2013) for details on how such boundary conditions and physical parameters affect surface gravity waves in the ocean.

A Small-Amplitude, Linear Approximation of the Free Surface

The boundary conditions described above (eqs. 1.23, 1.24, 1.25) apply to surface gravity waves. Now we will assume small amplitude waves where the amplitude η is much less than the other characteristic lengths, namely the wavelength λ and the depth h: $\eta \ll \lambda$ and $\eta \ll h$. In this approximation the slope of the free surface, $\frac{\partial \eta}{\partial x}$, will be small. Also, the velocity component in the x-direction, $\frac{\partial \phi}{\partial x}$, will be small since surface waves have relatively low frequencies. In other words, any movement in the x-direction occurs within a long period of oscillation. Thus, terms that are quadratically small (e.g., $\frac{\partial \eta}{\partial x}\frac{\partial \phi}{\partial x}$) are considered negligible. Therefore, we can approximate the kinematic free surface boundary condition (eq. 1.23) as

$$\frac{\partial \eta}{\partial t}(x,t) \approx \frac{\partial \phi}{\partial z}(x,\eta,t).$$

We note that ϕ depends on x, η, and t. But since η is considered to be small, we can expand the following in terms of its Taylor series:

$$\frac{\partial \phi}{\partial z}(x,\eta,t) = \frac{\partial \phi}{\partial z}(x,0,t) + \eta\frac{\partial^2 \phi}{\partial z^2}(x,0,t) + O(\eta^2).$$

where the O term is the order of convergence (this is explained further in a subsequent section). Thus we can use the first term in this approximation, that is, a first order approximation, for the previous equation to obtain

$$\frac{\partial \eta}{\partial t}(x,t) \approx \frac{\partial \phi}{\partial z}(x,0,t). \tag{1.26}$$

In a similar fashion, keeping only the linear terms within the dynamic free surface boundary condition (eq. 1.24) results in

$$\frac{\partial \phi}{\partial t}(x,\eta,t) + \frac{P}{\rho} + g\eta(x,t) \approx F(t).$$

The $\frac{\partial\phi}{\partial t}(x,\eta,t)$ term can be expanded in a Taylor series (about $z = 0$) where we will retain only the first term. Additionally, we can absorb $F(t)$ into the velocity potential via $\phi(x,z,t) + \int F(t)\,dt \rightarrow \phi'(x,z,t)$ (e.g., Dean and Dalrymple, 1991) to get

$$\frac{\partial\phi'}{\partial t}(x,0,t) + \frac{P}{\rho} + g\eta(x,t) \approx 0.$$

Using $\phi'(x,z,t)$ in place of $\phi(x,z,t)$ results in no alteration of the previous boundary conditions (since both variables produce the same result), so we can switch back to $\phi(x,z,t)$:

$$\frac{\partial\phi}{\partial t}(x,0,t) + \frac{P}{\rho} + g\eta(x,t) \approx 0.$$

A more useful form of this equation is found by taking the derivative with respect to time and noting eq. 1.26:

$$\frac{\partial^2\phi}{\partial t^2}(x,0,t) + g\frac{\partial\phi}{\partial z}(x,0,t) \approx 0. \tag{1.27}$$

Note that the bottom boundary condition (eq. 1.25) remains the same since there is no need for linearization.

Wave Celerity From the Laplace and Boundary Conditions

So that later we can show a simple dispersion relation that relates wave celerity (phase speed relative to stationary water) to wavelength, we now list the Laplace equation (eq. 1.21), the approximated (small-amplitude linearized) free surface boundary conditions (eqs. 1.26, 1.27), and the bottom boundary condition (eq. 1.25):

$$\begin{aligned}
\text{Laplace Equation} &\rightarrow \frac{\partial^2\phi}{\partial x^2} + \frac{\partial^2\phi}{\partial z^2} = 0 \\
\text{Kin. Free Surface Condition} &\rightarrow \frac{\partial\phi}{\partial z}(x,0,t) = \frac{\partial\eta}{\partial t}(x,t) \\
\text{Dyn. Free Surface Condition} &\rightarrow \frac{\partial^2\phi}{\partial t^2}(x,0,t) + g\frac{\partial\phi}{\partial z}(x,0,t) = 0 \\
\text{Kin. Bottom Surface Condition} &\rightarrow \frac{\partial\phi}{\partial z}(x,-h,t) = 0.
\end{aligned} \tag{1.28}$$

Let us assume that the free surface takes the form of a sinusoidal wave

$$\eta(x,t) = A\sin(\kappa x - \omega t) = A\sin(\kappa x - \kappa c t)$$

where κ is the angular wavenumber, ω is the angular frequency, c is the wave celerity, and A is the amplitude. Now, if we utilize the kinematic free surface boundary condition we get

$$\frac{\partial\phi}{\partial z}(x,0,t) = \frac{\partial\eta}{\partial t}(x,t) = -A\kappa c\cos(\kappa x - \kappa c t).$$

This tells us that $\frac{\partial\phi}{\partial z}$ is trigonometric with respect to x and t. Note that $\frac{\partial\phi}{\partial z}$, which is the derivative with respect to z, results in a function that depends on x and t. This provides some insight into a solution for the Laplace equation (where, in this case, we would like to know ϕ); specifically, ϕ can be expected to be a function that is trigonometric with respect to x and t. When finding a solution to the Laplace equation using the separation of variables method, the separation constant should be the same for both x and z directions (e.g., Dean and Dalrymple, 1991). In this case, the separation constant is κ, which we know is a real, postive number. Furthermore, the solution to the Laplace equation will be trigonometric in x and exponential (or, equivalently, hyperbolic) in z. A solution is of the form (e.g., Owczarek, 1968; Dean and Dalrymple, 1991)

$$\phi(x,z,t) = \cos(\kappa x - \kappa c t)\left[C_1\sinh(\kappa z) + C_2\cosh(\kappa z)\right]. \tag{1.29}$$

Now that we have the general form of $\phi(x,z,t)$ we can implement the bottom boundary condition (and noting that *cosh* is an even function while *sinh* is an odd function) to get

$$\cos(\kappa x - \kappa ct)\left[\kappa C_1 \cosh(\kappa h) - \kappa C_2 \sinh(\kappa h)\right] = 0.$$

Since this condition must be satisfied for all x and t the bracketed term above must be zero, which gives

$$C_1 = C_2 \tanh(\kappa h).$$

Substituting the constants C_1 and C_2 back into the general form of $\phi(x,z,t)$ we have

$$\phi(x,z,t) = C_2 \cos(\kappa x - \kappa ct)\left[\tanh(\kappa h)\sinh(\kappa z) + \cosh(\kappa z)\right].$$

Now, if we apply the dynamic free surface boundary condition to the above equation, and rearranging terms, the result is

$$C_2 \cos(\kappa x - \kappa ct)\left[-(\kappa c)^2 + g\kappa \tanh(\kappa h)\right] = 0.$$

Since this condition must be satisfied for all x and t the bracketed term above must be zero, which gives

$$\begin{gathered}\frac{c^2}{gh} = \frac{1}{\kappa h}\tanh(\kappa h) \\ \text{or} \\ \frac{c^2}{gh} = \frac{\lambda}{2\pi h}\tanh\left(\frac{2\pi h}{\lambda}\right)\end{gathered} \tag{1.30}$$

where we have converted from the angular wavenumber to wavelength. This equation is the result of assuming a small amplitude A in relation to the other characteristic lengths: $A \ll \lambda$ and $A \ll h$. Therefore, it is a dispersion relation for small amplitude surface gravity

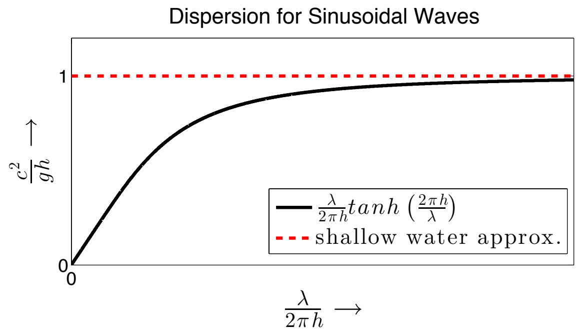

Figure 1.8: A dispersion relation for small amplitude sinuous waves with the prescribed boundary conditions. The propagation speed c depends on the acceleration due to gravity g, the water depth h, and the wavelength λ. The shallow water approximation is plotted as an asymptote as the wavelength becomes much larger than the water depth.

waves. A graphic of this relation is shown in Figure 1.8. By considering the Taylor series for hyperbolic sine and hyperbolic cosine we see that hyperbolic tangent has the following properties:

$$\tanh\left(\frac{2\pi h}{\lambda}\right) \approx 1 \text{ for large } \frac{2\pi h}{\lambda}$$

$$\tanh\left(\frac{2\pi h}{\lambda}\right) \approx \frac{2\pi h}{\lambda} \text{ for small } \frac{2\pi h}{\lambda}$$

A large value of $\frac{2\pi h}{\lambda}$ implies that the wavelength λ is much smaller than the fluid depth h, while a small value of $\frac{2\pi h}{\lambda}$ implies that λ is much larger than h. For these two endmember cases we can write

$$\frac{c^2}{gh} \approx \frac{\lambda}{2\pi h} \text{ for } A \ll \lambda \ll h \tag{1.31}$$

$$\frac{c^2}{gh} \approx 1 \text{ for } A \ll h \ll \lambda \tag{1.32}$$

Equation 1.31 is the dispersion relation for deep water, while equation 1.32 is the dispersion relation for shallow water. We are particularly interested in the shallow water approximation here, which directly becomes

$$c \approx \sqrt{gh}. \tag{1.33}$$

Thus, for large wavelength waves in shallow water (and small amplitude) we see that the wave celerity is only dependent on the acceleration due to gravity and the depth of the water (see Figure 1.8). This is an extremely fascinating, elegant result; it means that wave celerity for shallow water waves does not depend on wavelength (i.e., dispersion is not significant). In practice, shallow water theory often implies that λ is at least 20 times larger than h (e.g., Dean and Dalrymple, 1991).

The Shallow Water Wave Equations

Now we will show a derivation of the shallow water wave equations based on first principles. It is also possible to derive the shallow water wave equations from the momentum equation (eq. 1.19), the continuity equation (eq. 1.18), and the general kinematic free surface (eq. 1.23) and kinematic bottom (eq. 1.25) boundary conditions. For reference we state that such a derivation is done sufficiently well using the Leibniz integration rule to vertically integrate the continuity equation (e.g., Dean and Dalrymple, 1991). We do not show that derivation here. Instead, we start from intuitive conservation principles and show a somewhat more instructive derivation (e.g., Currie, 2013). Note that we are *not* assuming a sinusoidal wave here. However, Fourier analysis dictates that an arbitrarily shaped wave can be decomposed into a sum of sinusoidal waves with different amplitudes, frequencies, and wavelengths. Thus, for dispersion effects to be insignificant, shallow water theory implies that the smallest wavelength component is still large compared to the water depth. We are ignoring viscous effects and surface tension; although, surface tension is negligible for long waves in shallow water (e.g., Owczarek, 1968). Also, since we derive the equations for 2 spatial dimensions x and z, the conservation principles will be per unit length in the y-direction (into and out of the paper).

First, it is helpful to state the static equilibrium equation for a fluid. This equation is based on the balance of pressure variations and weight of some control volume in a homogeneous fluid (e.g., Halliday and Resnick, 1974):

$$p = p_0 + \int_z^\eta \rho g \, dz = p_0 + \rho g(\eta - z) \tag{1.34}$$

where p is pressure, p_0 is some reference pressure (usually taken at a free surface), g is the acceleration due to gravity, and $(\eta - z)$ is the vertical water column length. Note that we use the general convention that pressure is measured inward-normal to any surface. This needs to be remembered for consistency purposes.

For an arbitrarily-shaped wave that has significant dispersion effects (i.e., shorter wavelength components), the wave will disperse with time. However, when we appropriately employ the shallow water approximation dispersion has little effect on the initial waveform. In other words, the waveform does not significantly change shape with time. Therefore, we can use a 1-D propagation approximation. This means that the x-component of velocity is constant with depth, and the z-component of velocity is very small (i.e., the traveling waveform does not change much with time). If we consider a region under a progressive wave (Figure 1.9) we can determine conservation principles. Mass flow rate (per unit length in the y-direction) is defined as the density multiplied by the velocity across a surface multiplied by that same surface's area. Panel (b) of Figure 1.9 shows the mass flow rate into and out of the region of interest. The mass flow rate at the left is $\rho u(h+\eta)$. A truncated Taylor series results in the mass flow rate at the right being approximately $\rho u(h+\eta) + \frac{\partial}{\partial x}\left[\rho u(h+\eta)\right]\delta x$. The mass flow rate at the top is approximately $\rho \frac{\partial}{\partial t}(h+\eta)\delta x = \rho \frac{\partial \eta}{\partial t}\delta x$ if h is not changing

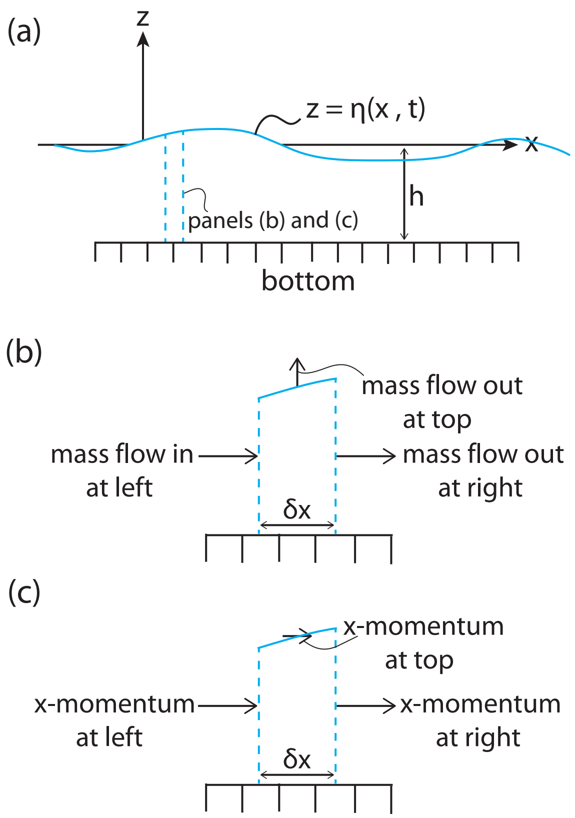

Figure 1.9: (a) A shallow water wave of arbitrary form. (b) The mass flows into a control volume and out of a control volume. (c) The momentum components, in the x-direction, are shown for the same region.

with time (i.e., for a stationary bottom), where we are assuming mass flow is essentially vertical there. Note that this is the same as determining how the volume (over the small interval δx) changes with time. Since this is an Eulerian specification, we are looking at a fixed region along the x-axis, so our volume will change shape by amplitude fluctuations along the z-axis. Intuitively, for an incompressible fluid, the mass flow rate into the region must equal the mass flow rate out of the region:

$$\rho u(h+\eta) \approx \rho u(h+\eta) + \frac{\partial}{\partial x}\left[\rho u(h+\eta)\right]\delta x + \rho \frac{\partial \eta}{\partial t}\delta x$$

or since the first terms on the LHS and RHS cancel, we can rearrange terms, divide by $\rho\delta x$, and let $\delta x \to 0$ to obtain

$$\frac{\partial \eta}{\partial t} + \frac{\partial}{\partial x}\left[u(h+\eta)\right] = 0. \tag{1.35}$$

This is the nonlinear *continuity equation* for shallow water waves over a stationary bottom.

Now we will focus on the nonlinear momentum equation for shallow water waves. Panel (c) of Figure 1.9 shows that we have x-axis components of momentum at the left, right, and top of the control volume region. Using Newton's second law, we can set the total rate of change in x-momentum (per unit length in the y-direction) equal to the total applied force in the x-direction (per unit length in the y-direction). We can find the x-component of momentum rate at the left by multiplying the mass flow rate by the velocity in the x-direction. Thus, the x-momentum rate at the left is $\rho u^2(h+\eta)$. A truncated Taylor series results in the x-momentum rate at the right being approximately $\rho u^2(h+\eta) + \frac{\partial}{\partial x}\left[\rho u^2(h+\eta)\right]\delta x$. Thus, the x-momentum rate changes from the left to the right by an amount approximately equal to $\frac{\partial}{\partial x}\left[\rho u^2(h+\eta)\right]\delta x$. We also need to incorporate x-momentum changes that result from changes in volume over the small interval δx. Note that any volume changes will result from fluctuations in amplitude along the z-axis. Thus, we need to multiply the volume by the velocity component in the x-direction and take the time derivative of this approximated quantity: $\frac{\partial}{\partial t}\left[\rho u(h+\eta)\right]\delta x$. This is, effectively, the same as multiplying the mass flow rate at the top surface by the velocity component in the x-direction, but with the velocity component included within the time derivative operation since we are examining changes in momentum. Thus, the total rate of change of x-momentum for the fluid element will be due to a difference in momentum rate (horizontally) across the element plus any rate of change of x-momentum for the top of the fluid element:

$$m\frac{Du}{dt} \approx \frac{\partial}{\partial x}\left[\rho u^2(h+\eta)\right]\delta x + \frac{\partial}{\partial t}\left[\rho u(h+\eta)\right]\delta x. \tag{1.36}$$

We need to set this equal to the net external force in the x-direction. The net external force in the x-direction comes from the hydrostatic pressure under the free surface (see Figure 1.10). We use the hydrostatic pressure because, by definition, shallow water theory implies surface waves with negligible vertical acceleration (that would lead to pressure fluctuations in time). Let us assume that there is a constant pressure p_0 at the free surface. Now, the force at the left (per unit length in the y-direction) that tends to accelerate the control volume in the positive x-direction (the pressure convention is inward-normal) is $F_{atLeft} = \int_{-h}^{\eta} p(x,z)\,dz$, and the force at the right (per unit length in the y-direction) that tends to accelerate the control volume in the negative x-direction is $F_{atRight} = \int_{-h}^{\eta} p(x+\delta x,z)\,dz$.

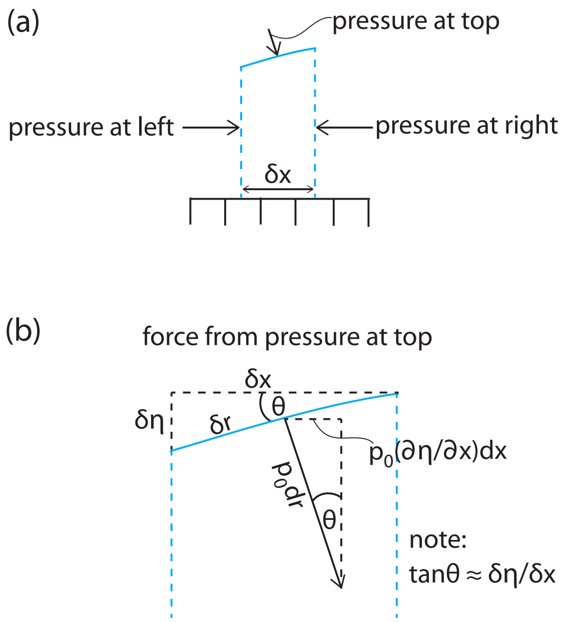

Figure 1.10: (a) Pressure on the left, right, and top of the control volume. (b) The force that results from pressure on the top.

From the *static* equilibrium equation we know that these forces are

$$\begin{aligned}
F_{atLeft} &= \int_{-h}^{\eta(x,t)} p(x,z)\,dz = \int_{-h}^{\eta(x,t)} \left[p_0 + \rho g(\eta(x,t) - z)\right]\,dz \\
&= p_0\left[h + \eta(x,t)\right] + \frac{\rho g \left[h + \eta(x,t)\right]^2}{2} \\
F_{atRight} &= -\int_{-h}^{\eta(x+\delta x,t)} p(x+\delta x,z)\,dz = -\int_{-h}^{\eta(x+\delta x,t)} \left[p_0 + \rho g(\eta(x+\delta x,t) - z)\right]\,dz \\
&= -p_0\left[h + \eta(x+\delta x,t)\right] - \frac{\rho g \left[h + \eta(x+\delta x,t)\right]^2}{2}.
\end{aligned}$$

The sum of these forces is

$$\begin{aligned}
F_{atLeft} + F_{atRight} = &-p_0\left[h + \eta(x+\delta x,t)\right] + p_0\left[h + \eta(x,t)\right] \\
&- \frac{\rho g \left[h + \eta(x+\delta x,t)\right]^2}{2} + \frac{\rho g \left[h + \eta(x,t)\right]^2}{2}.
\end{aligned}$$

This can be multiplied by $\frac{\delta x}{\delta x}$ to become

$$\begin{aligned}
F_{atLeft} + F_{atRight} = &\frac{-p_0\left[h + \eta(x+\delta x,t)\right] + p_0\left[h + \eta(x,t)\right]}{\delta x}\delta x \\
&+ \frac{-\rho g\left[h + \eta(x+\delta x,t)\right]^2 + \rho g\left[h + \eta(x,t)\right]^2}{2\delta x}\delta x
\end{aligned}$$

and we can write this as

$$F_{atLeft} + F_{atRight} = -p_0\frac{\delta(h+\eta)}{\delta x}\delta x - \frac{\rho g}{2}\frac{\delta(h+\eta)^2}{\delta x}\delta x. \tag{1.37}$$

Now we need to add the force at the top of the control volume as shown in panel (b) of Figure 1.10. If the pressure is p_0 everywhere along the free surface η then there is a force (per unit length in the y-direction), with components pointing in the -z and +x directions, that is equal to the length of the surface δr multiplied by p_0. As shown in panel (b) of Figure 1.10, $\tan(\theta) \approx \frac{\delta\eta}{\delta x}$. Thus, the positive x-component of this force (while noting that h is a constant) is

$$F_{atTop} \approx p_0\frac{\delta\eta}{\delta x}\delta x = p_0\frac{\delta(h+\eta)}{\delta x}\delta x. \tag{1.38}$$

Finally, we can add the left, right, and top x-component forces to get

$$\begin{aligned} F_{atLeft} + F_{atRight} + F_{atTop} &\approx -p_0\frac{\delta(h+\eta)}{\delta x}\delta x - \frac{\rho g}{2}\frac{\delta(h+\eta)^2}{\delta x}\delta x + p_0\frac{\delta(h+\eta)}{\delta x}\delta x \\ &= -\frac{\rho g}{2}\frac{\delta(h+\eta)^2}{\delta x}\delta x \\ &\approx -\frac{\rho g}{2}\frac{\partial(h+\eta)^2}{\partial x}\delta x \end{aligned} \tag{1.39}$$

Now, setting the total rate of change of momentum (eq. 1.36) equal to the sum of external forces in the x-direction (eq. 1.39) gives

$$\frac{\partial}{\partial x}\left[\rho u^2(h+\eta)\right]\delta x + \frac{\partial}{\partial t}\left[\rho u(h+\eta)\right]\delta x = -\frac{\rho g}{2}\frac{\partial(h+\eta)^2}{\partial x}\delta x.$$

Dividing the preceding equation by $\rho\delta x$, reordering the terms on the LHS, carrying out the first differentiation from the chain rule on the RHS, and letting $\delta x \to 0$ results in

$$\frac{\partial}{\partial t}\left[u(h+\eta)\right] + \frac{\partial}{\partial x}\left[u^2(h+\eta)\right] = -g(h+\eta)\frac{\partial\eta}{\partial x}. \tag{1.40}$$

This is the nonlinear *momentum* equation in shallow water. Therefore, the continuity and momentum equations for shallow water are

$$\begin{aligned} \frac{\partial\eta}{\partial t} + \frac{\partial}{\partial x}\left[u(h+\eta)\right] &= 0 \\ \frac{\partial}{\partial t}\left[u(h+\eta)\right] + \frac{\partial}{\partial x}\left[u^2(h+\eta)\right] &= -g(h+\eta)\frac{\partial\eta}{\partial x}. \end{aligned} \tag{1.41}$$

These equations are conservative forms since they are derived from conservation of mass and momentum. Many models employ an altered form of the momentum equation based on velocities. By differentiating the LHS of the momentum equation, while noting that $\left[u^2(h+\eta)\right]$ is the product of u with $u(h+\eta)$ and that h is a constant, we can write

$$\frac{\partial}{\partial t}\left[u(h+\eta)\right] + \frac{\partial}{\partial x}\left[u^2(h+\eta)\right] = (h+\eta)\frac{\partial u}{\partial t} + u\frac{\partial\eta}{\partial t} + u\frac{\partial}{\partial x}\left[u(h+\eta)\right] + u(h+\eta)\frac{\partial u}{\partial x}.$$

The second and third terms on the RHS are equal to the continuity equation multiplied by u, so they sum to zero. Thus, we get

$$\frac{\partial}{\partial t}\left[u(h+\eta)\right]+\frac{\partial}{\partial x}\left[u^2(h+\eta)\right]=(h+\eta)\frac{\partial u}{\partial t}+u(h+\eta)\frac{\partial u}{\partial x}.$$

We can substitute this expression into the momentum equation (eq. 1.41) to get:

$$\begin{aligned}\frac{\partial \eta}{\partial t}+\frac{\partial}{\partial x}\left[u(h+\eta)\right]&=0\\(h+\eta)\frac{\partial u}{\partial t}+u(h+\eta)\frac{\partial u}{\partial x}+g(h+\eta)\frac{\partial \eta}{\partial x}&=0.\end{aligned}\tag{1.42}$$

The terms in the momentum equation above all have a $(h+\eta)$ term that can be divided out. Therefore, this altered form of the continuity and momentum equations becomes

$$\begin{aligned}\frac{\partial \eta}{\partial t}+\frac{\partial}{\partial x}\left[u(h+\eta)\right]&=0\\\frac{\partial u}{\partial t}+u\frac{\partial u}{\partial x}+g\frac{\partial \eta}{\partial x}&=0.\end{aligned}\tag{1.43}$$

1.3 Numerical Methods

The computer codes used in the following studies utilize the Finite Difference Method (FDM) and the Finite Element Method (FEM) to numerically calculate movement (e.g., wave) properties in time. Therefore, it is critical to know, at a basic level, how the FDM and FEM serve to approximate physical processes. Because some physical processes can be described through continuous differential equations (e.g., the seismic wave equation, eq. 1.9), it can be useful to approximate those continuous equations with other equations over finite intervals. The FDM and FEM are two numerical techniques that approximate solutions to properly defined differential equations by using those differential equations to form discrete sets of algebraic equations (e.g., Hughes, 2000; Strang, 2007; LeVeque, 2007).

Below we briefly describe the FDM and then more fully describe the FEM in the form of a hydrodynamic example.

1.3.1 A Short Note on Finite Differences

Initial development of finite differences involves a classic definition of the derivative of a locally continuous function $f(x)$ from calculus (e.g., Strang, 2007):

$$\frac{d}{dx} f(x) := \lim_{h \to 0} \frac{f(x+h) - f(x)}{h}.$$

Removing the limit, so that we can operate over a discrete interval, we can write the *forward* (i.e., some value of x *plus* h) difference equation

$$FD := \frac{f(x+h) - f(x)}{h}$$

and the analogous *backward* (i.e., some value of x *minus* h) difference equation

$$BD := \frac{f(x) - f(x-h)}{h}$$

and the *centered* (i.e., some value of x *plus and minus* h) difference equation

$$CD := \frac{f(x+h) - f(x-h)}{2h}.$$

Of course, we can have difference equations operate on each other so that the result is differences of differences. For example, the backward difference can operate on the forward difference:

$$\begin{aligned} BD[FD] &= BD\left[\frac{f(x+h) - f(x)}{h}\right] \\ &= \frac{\left[\frac{f(x+h)-f(x)}{h}\right] - \left[\frac{f(x)-f(x-h)}{h}\right]}{h} \\ &= \frac{f(x+h) - 2f(x) + f(x-h)}{h^2}. \end{aligned}$$

To determine the *order of accuracy* of the above finite differences, we need to write the Taylor series for the function $f(x+h)$ as

$$f(x+h) = f(x) + h\frac{df}{dx} + \frac{h^2}{2!}\frac{d^2f}{dx^2} + \frac{h^3}{3!}\frac{d^3f}{dx^3} + \dots$$

and the Taylor series for the function $f(x-h)$ as

$$f(x-h) = f(x) - h\frac{df}{dx} + \frac{h^2}{2!}\frac{d^2f}{dx^2} - \frac{h^3}{3!}\frac{d^3f}{dx^3} + \dots$$

Therefore, we can substitute this expression for $f(x+h)$ into the forward difference equation to obtain

$$\begin{aligned}
FD &= \frac{f(x+h) - f(x)}{h} \\
&= \frac{f(x) + h\frac{df}{dx} + \frac{h^2}{2!}\frac{d^2f}{dx^2} + \frac{h^3}{3!}\frac{d^3f}{dx^3} + \dots - f(x)}{h} \\
&= \frac{df}{dx} + \frac{h}{2!}\frac{d^2f}{dx^2} + \frac{h^2}{3!}\frac{d^3f}{dx^3} + \dots \\
&= \frac{df}{dx} + O(h)
\end{aligned}$$

where we say that the forward difference equation is first order accurate since the error terms (big 'O' terms) contain h to the power of one as well as higher powers (LeVeque, 2007). Similarly, the backward difference formula is first order accurate. We can repeat this process for the centered difference formula, using the Taylor series for both $f(x+h)$ and $f(x-h)$:

$$\begin{aligned}
CD &= \frac{f(x+h) - f(x-h)}{2h} \\
&= \frac{f(x) + h\frac{df}{dx} + \frac{h^2}{2!}\frac{d^2f}{dx^2} + \frac{h^3}{3!}\frac{d^3f}{dx^3} + \dots - f(x) + h\frac{df}{dx} - \frac{h^2}{2!}\frac{d^2f}{dx^2} + \frac{h^3}{3!}\frac{d^3f}{dx^3} - \dots}{2h} \\
&= \frac{df}{dx} + \frac{h^2}{3!}\frac{d^3f}{dx^3} + \dots \\
&= \frac{df}{dx} + O(h^2)
\end{aligned}$$

where the centered difference equation is second order accurate since the error terms contain h to the power of two as well as higher powers. These finite difference equations are approximations of derivatives; therefore, it is somewhat evident that finite difference equations can approximate more complex differential equations that describe physical processes. We note that the functions being approximated can be functions of both time and space, and thus there can be difference equations with respect to each dimension. Of course, there are many different theoretical and numerical techniques for efficiently and accurately approximating such equations using the FDM (e.g., LeVeque, 2007), and we will not go into further detail here.

1.3.2 The Finite Element Method

In the following section we describe the finite element method (FEM) through an example of the 1-D (more specifically, 1 propagation dimension, 1 amplitude dimension, and 1 time dimension) shallow water wave equations (eq. 1.43). The FEM solution process involves the following key steps:

(1) Define the problem to be solved in the form of differential equations. This will ultimately involve an integral form of the differential equations. A critical part of defining the problem is to specify the boundary and initial conditions.

(2) Select the finite element type (e.g., lines, curves, etc. in 1-D; rectangles, triangles, etc. in 2-D).

(3) Define the mesh for the problem using the element type. This includes descriptions of node and element layouts for the model space.

(4) Select the shape function type (e.g., linear, quadratic, etc.) to be integrated over the

selected element type.

(5) Compute the system matrices and system vectors. For time-dependent problems, this involves finite difference techniques to perform numerical integration at each time step.

(6) Solve the resulting set of linear algebraic equations for the system variables.

(7) Save and output the results of the nodal and element variables.

To simplify the shallow water wave equations, we can define $H \coloneqq h + \eta$. Noting that h is a constant, we can write eq. 1.43 as

$$\begin{aligned} \frac{\partial H}{\partial t} + \frac{\partial}{\partial x}(uH) = 0 \\ \frac{\partial u}{\partial t} + u\frac{\partial u}{\partial x} + g\frac{\partial H}{\partial x} = 0 \end{aligned} \tag{1.44}$$

where these equations apply to our open model domain $\Omega = (0, L)$, where the origin $(x = 0)$ is the left edge of the domain and L is the right edge of the domain,. We can now define, for our example, boundary and initial conditions. We know that $u(x, t)$ is the particle velocity in the x-direction, and that $H(x, t)$ is the total fluid height. On the boundary $\sigma = \{0, L\}$ of our model, we set $u(0, t) = u(L, t) = 0$ and $H(0, t) = H(L, t) = H_0$ where H_0 is some constant. For the initial conditions (i.e., the first time node), we set $u(x, 0) = 0$ and $H(x, 0) = H_0 + Ae^{-B\left[\left(x-\frac{L}{2}\right)^2\right]}$ (i.e, a smooth Gaussian function plus a constant; although, we can model a variety of functions here). We can now define the problem in *strong* form:

$$(S)\begin{cases} \frac{\partial H}{\partial t} + \frac{\partial}{\partial x}(uH) = 0, & \text{on } \Omega \\ \frac{\partial u}{\partial t} + u\frac{\partial u}{\partial x} + g\frac{\partial H}{\partial x} = 0, & \text{on } \Omega \\ u(0,t) = u(L,t) = 0, & \text{on } \sigma \\ H(0,t) = H(L,t) = H_0, & \text{on } \sigma \\ u(x,0) = 0, & \text{on } \Omega \\ H(x,0) = H_0 + Ae^{-B\left[\left(x-\frac{L}{2}\right)^2\right]}, & \text{on } \Omega. \end{cases} \tag{1.45}$$

The strong form is the set of differential equations that directly describe the problem to be solved. We now transform the strong form into the *weak* form of the problem. In order to do so, we need to define collections of trial solutions of $u(x,t)$ and $H(x,t)$ as well as the collections of trial weighting functions $w(x)$ for the problem. Note that, unlike the trial solutions, the weighting functions are only functions of x (not time!). All of these collections u, H, and w need to be in a Sobolev space at a given point in time. In this case, a function f is in a Sobolev space if

$$\int_0^L f^2\,dx < \infty; \int_0^L \left(\frac{\partial f}{\partial x}\right)^2 dx < \infty.$$

In other words, we need to be able to properly integrate these functions and their derivatives over the domain. Such functions are often called H^1-functions (since the function itself and its *1st* derivative are square integrable), and this notation should not be confused with the fluid height H. The collection of trial solutions of u are

$$\mathcal{L} = \left\{u | u \in H^1, u(0,t) = u(L,t) = 0, u(x,0) = 0\right\}$$

and the collection of trial solutions for H and collection of trial weighting functions w are

$$\mathcal{M} = \left\{ H | H \in H^1, H(0,t) = H(L,t) = H_0, H(x,0) = H_0 + Ae^{-B\left[\left(x-\frac{L}{2}\right)^2\right]} \right\}$$

$$\mathcal{V} = \left\{ w | w \in H^1, w(0) = w(L) = 0, \text{where } w = w(x) \right\}.$$

The weighting functions are defined to be zero on the boundaries since we fix the values of u and H there. Approximations to these collections need to be employed within the FEM. Often, approximations are denoted by a superscript h such as u^h being an approximation of u. We will not be employing this notation, but each u, v, and w will be considered to be an approximation of the above collection when implementing the finite discretization below. The strong form of the continuity equation is

$$\frac{\partial H}{\partial t} + \frac{\partial}{\partial x}(uH) = 0.$$

Multiplying by our weighting function w and integrating from 0 to L we get

$$\int_0^L w \frac{\partial H}{\partial t}\, dx + \int_0^L w \frac{\partial}{\partial x}(uH)\, dx = 0.$$

For two functions $f(x)$ and $g(x)$ and constants a and b, integration by parts yields $\int_a^b g \frac{df}{dx}\, dx = fg|_a^b - \int_a^b f \frac{dg}{dx}\, dx$. Therefore, we can transform the second term in the above equation using integration by parts: $\int_0^L w \frac{\partial}{\partial x}(uH)\, dx = wHu|_0^L - \int_0^L Hu \frac{\partial w}{\partial x}\, dx$. However, $wHu|_0^L = 0$ due to our boundary conditions, so we can write the equation above as

$$\int_0^L w \frac{\partial H}{\partial t}\, dx - \int_0^L Hu \frac{\partial w}{\partial x}\, dx = 0. \tag{1.46}$$

This is the weak form of the continuity equation as it has been multiplied, integrated, and manipulated. The strong form of the momentum equation is

$$\frac{\partial u}{\partial t} + u\frac{\partial u}{\partial x} + g\frac{\partial H}{\partial x} = 0.$$

Multiplying by our weighting function w and integrating from 0 to L we get

$$\int_0^L w\frac{\partial u}{\partial t}\,dx + \int_0^L wu\frac{\partial u}{\partial x}\,dx + \int_0^L wg\frac{\partial H}{\partial x}\,dx = 0. \tag{1.47}$$

This is the weak form of the momentum equation.

One of the key aspects of the *Galerkin* approach to the FEM is that trial solutions and trial weighting functions are composed of the same spatial shape functions (or basis functions). We will explain this further now. We choose trial solutions and weighting functions that consist of linear combinations of the shape functions N_A, where A indicates the global node number in the mesh: $A = \{1, 2, 3, \ldots, n\}$. Each shape function N_A will have a value of 1 at node A and a value of *zero* at every other node (see Figure 1.11). As such, the weighting functions can be written as

$$w = \sum_{A=1}^{n} C_A N_A(x)$$

where the C_As are arbitrary constants. For the velocity $u(x,t)$, we define the total set of nodes as η and the set of nodes on the boundary σ as η_p. For the height $H(x,t)$, we define the total set of nodes as η and the set of nodes on the boundary σ as η_r. For each time step, we define

$$v = \sum_{B\in\eta-\eta_p} u_B(t)N_B(x)$$
$$q = \sum_{C\in\eta-\eta_r} H_C(t)N_C(x)$$

where u_B and H_C are nodal values that depend on time only. However, the shape functions do not depend on time, so we have separated the desired variables into time and space components. Additionally, we let

$$s = \sum_{B\in\eta_p} pN_B(x)$$

$$t = \sum_{C \in \eta_r} r N_C(x)$$

where p is the velocity boundary condition and r is the height boundary condition. From the strong form of the problem, we know that $p = 0$ and $r = H_0$, and we will utilize these variables now. Note that the shape functions are the same functions for each approximation (albeit a different subscript A, B, or C). Now we can write $u = v + s$, $H = q + t$, and w as

$$u = \sum_{B \in \eta - \eta_p} u_B(t) N_B(x) + \sum_{B \in \eta_p} p N_B(x) = \sum_{B \in \eta - \eta_p} u_B(t) N_B(x)$$

$$H = \sum_{C \in \eta - \eta_r} H_C(t) N_C(x) + \sum_{C \in \eta_r} r N_C(x) = \sum_{C \in \eta - \eta_r} H_C(t) N_C(x) + \sum_{C \in \eta_r} H_0 N_C(x)$$

$$w = \sum_{A \in \eta - \eta_r} C_A N_A(x) + \sum_{A \in \eta_r} 0 N_A(x) = \sum_{A \in \eta - \eta_r} C_A N_A(x).$$

Note that w can be written as containing non-zero values at nodes in either $\eta - \eta_r$ or $\eta - \eta_p$, since the boundary values for u and H lie on the same nodes. The weak form of the problem is the following: Given p and r are real, defined values, find $u \in \mathcal{L}$ and $H \in \mathcal{M}$ such that for all $w \in \mathcal{V}$

$$(W) \begin{cases} \int_0^L w \frac{\partial H}{\partial t}\, dx - \int_0^L H u \frac{\partial w}{\partial x}\, dx = 0 \\ \int_0^L w \frac{\partial u}{\partial t}\, dx + \int_0^L w u \frac{\partial u}{\partial x}\, dx + \int_0^L w g \frac{\partial H}{\partial x}\, dx = 0. \end{cases} \tag{1.48}$$

For this problem, we choose to use constant length, linear, one-dimensional elements along the x-axis. The shape functions are linear hat functions (see Figure 1.11). The approximated variables H and u will be made up of these shape functions; for example, see Figure 1.11 panel (b) for a cartoon schematic of H. Using the above definitions, we can re-write the weak form of the continuity equation (eq. 1.46) as

$$\int_0^L w \frac{\partial H}{\partial t}\, dx - \int_0^L H u \frac{\partial w}{\partial x}\, dx = 0$$

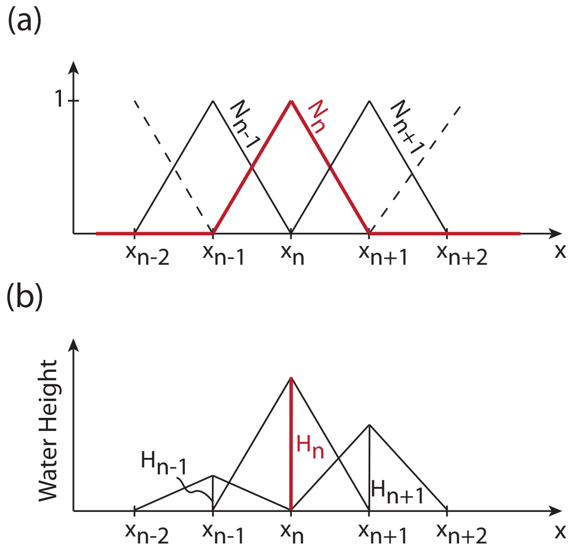

Figure 1.11: (a) Cartoon schematic of shape functions. (b) Cartoon schematic of the approximated water height.

and then transform the equation above into

$$\begin{aligned}\int_0^L \left[\sum_{A\in\eta-\eta_r} C_A N_A(x)\frac{\partial}{\partial t}\left(\sum_{C\in\eta-\eta_r} H_C(t)N_C(x) + \sum_{C\in\eta_r} H_0 N_C(x)\right)\right] dx \\ - \int_0^L \left[\left(\sum_{C\in\eta-\eta_r} H_C(t)N_C(x)\right.\right. \\ \left.\left. + \sum_{C\in\eta_r} H_0 N_C(x)\right)\left(\sum_{B\in\eta-\eta_p} u_B(t)N_B(x)\right)\left(\frac{\partial}{\partial x}\sum_{A\in\eta-\eta_r} C_A N_A(x)\right)\right] dx = 0.\end{aligned}$$

We can place the sum over C_As in the front of the terms to get

$$\begin{aligned}\sum_{A\in\eta-\eta_r} C_A \int_0^L \left[N_A(x)\frac{\partial}{\partial t}\left(\sum_{C\in\eta-\eta_r} H_C(t)N_C(x) + \sum_{C\in\eta_r} H_0 N_C(x)\right)\right] dx \\ - \sum_{A\in\eta-\eta_r} C_A \int_0^L \left[\left(\sum_{C\in\eta-\eta_r} H_C(t)N_C(x)\right.\right. \\ \left.\left. + \sum_{C\in\eta_r} H_0 N_C(x)\right)\left(\sum_{B\in\eta-\eta_p} u_B(t)N_B(x)\right)\left(\frac{\partial}{\partial x}N_A(x)\right)\right] dx = 0.\end{aligned}$$

Since the C_As are arbitrary constants, the other terms must sum to zero. Therefore, we have

$$
\begin{aligned}
&\int_0^L \left[N_A(x) \frac{\partial}{\partial t} \left(\sum_{C\in\eta-\eta_r} H_C(t) N_C(x) + \sum_{C\in\eta_r} H_0 N_C(x) \right) \right] dx \\
&\qquad - \int_0^L \left[\left(\sum_{C\in\eta-\eta_r} H_C(t) N_C(x) \right.\right. \\
&\qquad \left.\left. + \sum_{C\in\eta_r} H_0 N_C(x) \right) \left(\sum_{B\in\eta-\eta_p} u_B(t) N_B(x) \right) \left(\frac{\partial}{\partial x} N_A(x) \right) \right] dx = 0.
\end{aligned}
$$

Now the time derivative of $H_0 N_C$ is zero since H_0 is a constant and N_C does not depend on time, so we can write the equation above as

$$
\begin{aligned}
&\int_0^L \left[N_A(x) \frac{\partial}{\partial t} \left(\sum_{C\in\eta-\eta_r} H_C(t) N_C(x) \right) \right] dx \\
&\qquad - \int_0^L \left[\left(\sum_{C\in\eta-\eta_r} H_C(t) N_C(x) \right.\right. \\
&\qquad \left.\left. + \sum_{C\in\eta_r} H_0 N_C(x) \right) \left(\sum_{B\in\eta-\eta_p} u_B(t) N_B(x) \right) \left(\frac{\partial}{\partial x} N_A(x) \right) \right] dx = 0.
\end{aligned}
$$

The second term in square brackets can be broken up and we can write

$$
\begin{aligned}
&\int_0^L \left[N_A(x) \frac{\partial}{\partial t} \left(\sum_{C\in\eta-\eta_r} H_C(t) N_C(x) \right) \right] dx \\
&- \int_0^L \left[\left(\sum_{C\in\eta-\eta_r} H_C(t) N_C(x) \right) \left(\sum_{B\in\eta-\eta_p} u_B(t) N_B(x) \right) \left(\frac{\partial}{\partial x} N_A(x) \right) \right] dx \\
&- \int_0^L \left[\sum_{C\in\eta_r} H_0 N_C(x) \left(\sum_{B\in\eta-\eta_p} u_B(t) N_B(x) \right) \left(\frac{\partial}{\partial x} N_A(x) \right) \right] dx = 0.
\end{aligned}
\tag{1.49}
$$

This is the discretized form of the continuity equation. Using the same process, the discretized form of the momentum equation is

$$
\begin{aligned}
&\int_0^L \left[N_A(x) \frac{\partial}{\partial t} \left(\sum_{C \in \eta - \eta_p} u_C(t) N_C(x) \right) \right] dx \\
+ &\int_0^L \left[N_A(x) \left(\sum_{B \in \eta - \eta_p} u_B(t) N_B(x) \right) \frac{\partial}{\partial x} \left(\sum_{C \in \eta - \eta_p} u_C(t) N_C(x) \right) \right] dx \\
+ &\int_0^L \left[N_A(x) g \frac{\partial}{\partial x} \left(\sum_{C \in \eta - \eta_r} H_C(t) N_C(x) \right) \right] dx \\
+ &\int_0^L \left[N_A(x) g \frac{\partial}{\partial x} \left(\sum_{C \in \eta_r} H_0 N_C(x) \right) \right] dx = 0.
\end{aligned}
\tag{1.50}
$$

The reader may notice that in some integral terms there are two unknown variables u and H (i.e., there are multivariable integral terms). This is due to the nonlinear nature of the shallow water wave equations. We now use the method of Navon (1979) to quasilinearize these terms by approximating u, only in the nonlinear integral terms, with

$$u^* = u^{N+\frac{1}{2}} = \frac{3}{2}u^N - \frac{1}{2}u^{N-1} + O(\Delta t^2)$$

where the superscripts indicate the time node. We can re-write the discretized forms of the continuity (eq. 1.49) and momentum (eq. 1.50) equations, respectively, using u^*, using summation notation (while remembering whether sums are taken inside the domain or at the boundaries), and removing the explicit dependence on x and t, as

$$\begin{aligned}
\int_0^L N_A \frac{\partial H_C}{\partial t} N_C \, dx \\
-\int_0^L H_C N_C u_B^* N_B \frac{\partial N_A}{\partial x} \, dx \\
-\int_0^L H_0 N_C u_B^* N_B \frac{\partial N_A}{\partial x} \, dx = 0 \\
\text{and} \\
\int_0^L N_A \frac{\partial u_C}{\partial t} N_C \, dx \\
+\int_0^L N_A u_B^* N_B u_C \frac{\partial N_C}{\partial x} \, dx \\
+\int_0^L N_A g H_C \frac{\partial N_C}{\partial x} \, dx \\
+\int_0^L N_A g H_0 \frac{\partial N_C}{\partial x} \, dx = 0.
\end{aligned} \tag{1.51}$$

The u^* terms can be thought of as constants since they can be found from the previous time steps. Additionally, we couple the continuity and momentum equations in H by inputing the values for H calculated from the continuity equation, at a given time step, into the momentum equation at that same time step. Therefore, any summation over H in the momentum equation can be thought of as a constant. If we define the following *system* matrices and vectors as

$$M_{AC} = \int_0^L N_A N_C \, dx = \sum_e^{n-1} \int_{\Omega_e} N_A N_C \, dx$$

$$K1_{AC} = \int_0^L N_C u_B^* N_B \frac{\partial N_A}{\partial x} \, dx = \sum_e^{n-1} \int_{\Omega_e} N_C u_B^* N_B \frac{\partial N_A}{\partial x} \, dx$$

$$K11_A = \int_0^L H_0 N_C u_B^* N_B \frac{\partial N_A}{\partial x} \, dx = \sum_e^{n-1} \int_{\Omega_e} H_0 N_C u_B^* N_B \frac{\partial N_A}{\partial x} \, dx$$

$$K2_{AC} = \int_0^L N_A u_B^* N_B \frac{\partial N_C}{\partial x} \, dx = \sum_e^{n-1} \int_{\Omega_e} N_A u_B^* N_B \frac{\partial N_C}{\partial x} \, dx$$

$$K21_A = \int_0^L N_A g H_C \frac{\partial N_C}{\partial x}\, dx = \sum_e^{n-1} \int_{\Omega_e} N_A g H_C \frac{\partial N_C}{\partial x}\, dx$$

$$K22_A = \int_0^L N_A g H_0 \frac{\partial N_C}{\partial x}\, dx = \sum_e^{n-1} \int_{\Omega_e} N_A g H_0 \frac{\partial N_C}{\partial x}\, dx$$

where each matrix entry can be written as a sum of integrals over each element (i.e., piecewise integration). Note that each term in the RHS sum of each equation above represents an entry in the *element* matrices and vectors. We can write the continuity and momentum equations, respectively, using the system matrices and vectors, as

$$M_{AC}\frac{\partial H_C}{\partial t} - K1_{AC}H_C - K11_A = 0$$

$$\text{or}$$

$$M_{AC}\frac{\Delta H_C}{\Delta t} - K1_{AC}H_C - K11_A = 0$$

$$\text{and} \tag{1.52}$$

$$M_{AC}\frac{\partial u_C}{\partial t} + K2_{AC}u_C + K21_A + K22_A = 0$$

$$\text{or}$$

$$M_{AC}\frac{\Delta u_C}{\Delta t} + K2_{AC}u_C + K21_A + K22_A = 0.$$

A Crank-Nicolson finite difference scheme of order 2 in time (i.e., $O(\Delta t^2)$) (e.g., Navon, 1979) can be used for the time stepping that results in the following difference equations for the continuity and momentum equations:

$$\mathbf{M}\mathbf{H}^{n+1} - \frac{\Delta t}{2}\mathbf{K}1\mathbf{H}^{n+1} = \mathbf{M}\mathbf{H}^{n} + \frac{\Delta t}{2}\mathbf{K}1\mathbf{H}^{n} + \frac{\Delta t}{2}\mathbf{K}11 + + \frac{\Delta t}{2}\mathbf{K}11$$

$$\text{and}$$

$$\mathbf{M}\mathbf{u}^{n+1} + \frac{\Delta t}{2}\mathbf{K}2\mathbf{u}^{n+1} + \frac{\Delta t}{2}\mathbf{K}21^{n+1} = \mathbf{M}\mathbf{u}^{n} - \frac{\Delta t}{2}\mathbf{K}2\mathbf{u}^{n} - \frac{\Delta t}{2}\mathbf{K}21^{n} - \frac{\Delta t}{2}\mathbf{K}22 - \frac{\Delta t}{2}\mathbf{K}22. \tag{1.53}$$

where the superscripts indicate the time node. Following Hughes (2000), we compute element matrices and vectors (i.e., for each element), and then build the system matrices and vectors that are shown above. We can then solve for the variables H and u using the above FEM approach. First we find H from the continuity difference equation (using u^*), then we find u from the momentum difference equation using H and u^*, then update u^* and repeat the process. From the strong form of the problem, we use $p = 0$ (in velocity units), $H_0 = 1$ (in length units), $A = \frac{1}{10}$, $B = \frac{1}{20}$, $L = 100$ (in length units), and $g = 1$ (in acceleration units). Using these values along with an element size of 1 length unit and a time step size of $\frac{1}{4}$ time units, Figure 1.12 shows H and u at different points in time. According to shallow water wave theory, the surface wave should propagate at approximately 1 unit length per unit time, or $\sqrt{gh} \approx \sqrt{1} = 1$ unit length per unit time. We see that this is indeed true. Note that u is not the propagation speed, but the particle speed. The propagation speed is partial confirmation that our code is performing correctly.

1.4 Dynamically Modeling Earthquakes and Tsunamis

Above we discuss some of the basic principles and equations that help describe motion from earthquakes and tsunamis. Actual earthquake-generated tsunamis are among the most destructive natural hazards, with recent examples including the 2004 M_w 9.1 Sumatran-Andaman earthquake and tsunami (Lay et al., 2005) and the 2011 M_w 9.0 Tohoku-Oki earthquake and tsunami (Simons et al., 2011). Tsunamis like these that are generated along the Pacific Rim and other regions can can cause widespread devastation. In particular, tsunamis generated along the Alaskan-Aleutian megathrust offshore of the

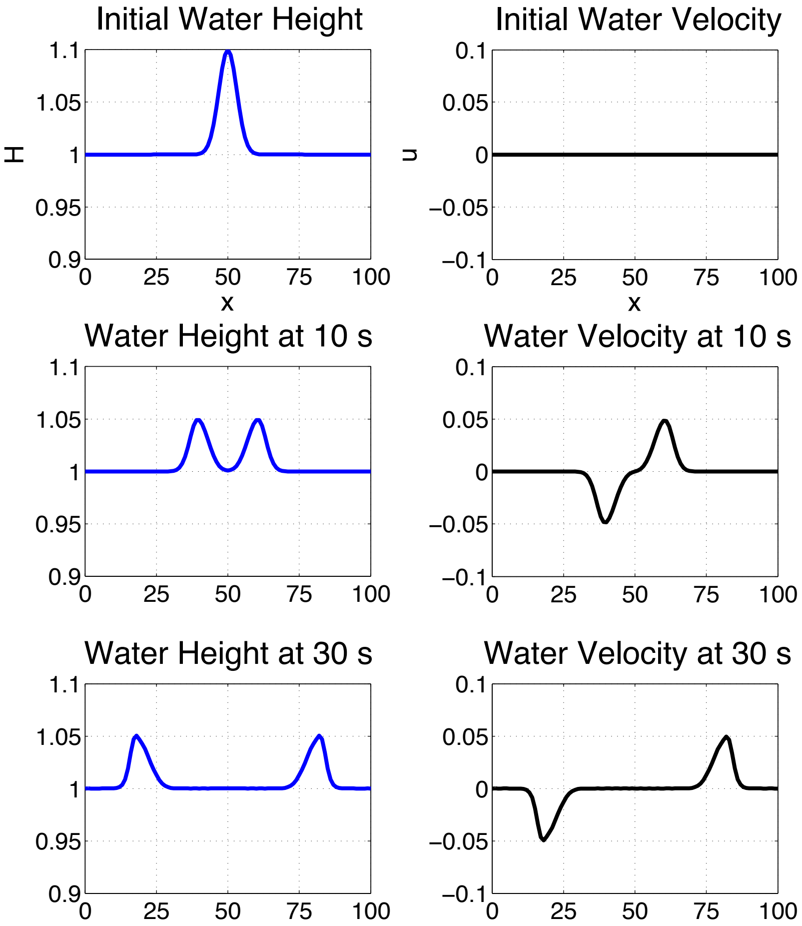

Figure 1.12: (left) Height of water surface at 0 s, 10 s, and 30 s. (right) Particle velocity of water surface at 0 s, 10 s, and 30 s.

Alaska Peninsula could have large adverse effects on Pacific coasts (Ryan et al., 2012). The earthquake source is one of the largest sources of uncertainty for earthquake-generated tsunami hazard analysis. The seismic moment, slip distribution, and time-dependent rupture path of future earthquakes are often poorly constrained, but these parameters produce a first-order effect on tsunami generation (Geist, 1998; Geist and Dmowska, 1999; Geist and Bilek, 2001; Geist, 2002; Wendt et al., 2009). Typical tsunami generation methods rely on static or kinematic models of the earthquake source, in which the seismic moment, slip distribution, and rupture path are assumed a priori, usually based on models of prior earthquakes and/or a probabilistic slip model (Kanamori, 1972; Satake, 1985; Satake, 2002; Geist, 2002). However, such models are not guaranteed to be consistent with any physically plausible faulting scenario, and may span a range of parameter space far beyond what is physically realistic. In addition, the historical record is incomplete for very large (M_w 9+) earthquakes, and may not encompass all the physically possible earthquake scenarios. One way to ensure that tsunami models are grounded in realistic physics and span a realistic range of earthquake sizes and slip patterns is to use spontaneous dynamic earthquake rupture models to simulate the earthquake source (e.g., Day, 1982; Olsen et al., 1997; Kame et al., 2003; Oglesby and Mai, 2012). Such models start with the fault geometry, the material properties, the loading stress on the system, and the frictional behavior on the fault. However, we note that these initial input parameters can be uncertain and in many cases such parameters involve assumptions that are difficult to constrain (e.g., the stress field within the real Earth is not known!). Based on these input parameters and physical laws, the earthquake rupture and ground motion processes (including the final size of the earthquake, the rupture path, the spatiotemporal slip distribution, and the near-source ground motion time history) are calculated results of the models. The ground motion can then be used directly as a boundary condition in tsunami models (Wendt et al., 2009).

Although large-magnitude earthquakes generate tsunamis that cause extensive destruction, smaller earthquakes can produce local tsunamis that provide little warning time and heavily damage restricted regions. The Ventura Basin in southern California is an area that is increasingly recognized to present a significant seismic and tsunami hazard.

The region contains several faults – in close proximity – that extend offshore, raising the possibility that they may rupture in a large multi-segment earthquake with moment magnitude potentially up to 7.8 (Hubbard et al., 2014). At least two large thrust faults – the Ventura/Pitas Point and Red Mountain – extend offshore, and may thus produce a significant local tsunami whether they rupture separately or in tandem. The Ventura Basin region is cut by several large thrust/reverse faults, including the Ventura, Pitas Point, Red Mountain, and San Cayetano faults (Sarna-Wojeicki et al., 1976; Perry and Bryant, 2002; Hubbard, 2014). Uplifted marine terraces (Rockwell, 2011) indicate single-event uplifts of 5-10 m, with fault slip potentially even larger. The coastline region has populated areas (such as metropolitan Ventura), so an earthquake and tsunami hazard assessment based on these faults is critically important; however, the hazard from such events is still under development. Dynamic earthquake and tsunami models can help constrain the range and distribution in the size of future earthquakes and locally generated tsunamis.

The exact mechanisms of at least a few severe tsunami disasters within the last few decades still remain inconclusive, with one example being the 1998 Papua New Guinea earthquake and tsunami that resulted in more than 2,000 casualties (Fujima et al, 1999; Matsuyama et al., 1999). Considerable discrepancies have been pointed out between tsunami models and tsunami observations, particularly in tsunami height and travel time (Ohmachi et al., 2001). Such discrepancies may result from uncertainties in earthquake source models that are based on seismic-wave and tsunami data (Imamura et al., 1994). Earthquake source parameters such as seismic moment and slip distribution have first-order effects on tsunami size (e.g., Geist, 1998), and these source parameters are related to the dynamic elastic wave field generated during earthquakes. By constraining earthquake source parameters from characteristics of the Rayleigh-wave field, one may also constrain tsunami properties such as size and wave train structure (Dutykh and Dias, 2008). When generated by tsunamigenic earthquakes, Rayleigh waves travel along the ocean floor with faster horizontal phase velocities than corresponding tsunamis (Okal, 1988). The possibility of a tsunami warning system using acoustic ocean waves has been previously suggested (Ewing et al., 1950; Yamashita and Sato, 1976), but accurate tsunami warning is still elusive due to large uncertainties in what causes the distribution of tsunami size and devastation. Tsunami disaster mitigation leads to a need for tsunami early warning, and constraining properties of the tsunami from leading Rayleigh waves can provide a route to more enhanced early warning that includes local effects from properties such as fault slip distribution and bathymetry.

Chapter 2

Modeling Seafloor Deformation and Tsunami Generation Offshore Southern Alaska Using Dynamic Finite Element Analysis

2.1 Abstract

Motivated by the 2011 M_w 9 Tohoku-Oki earthquake and potential earthquakes on the Alaskan-Aleutian Megathrust, we use computational simulations to investigate the effects of fault rupture dynamics on slip, free surface deformation, and resulting tsunami formation from scenario M_w 9 megathrust earthquakes. Unlike static dislocation models, dynamic models account for the force that the entire fault system exerts on each individual

element of the model for each time step, so that earthquake rupture takes a path that is consistent with the physics of the model. To isolate the effects of different physical variables, we model four different dynamic rupture scenarios: a spatially-homogenous prestress and frictional parameter scenario, two scenarios with rate-strengthening-like friction (e.g., Dieterich, 1992), and one scenario with spatially-heterogeneous prestress. Given geometric, material, and plate-coupling data along the Alaska-Aleutian megathrust assembled from the USGS-led Science Application For Risk Reduction (SAFRR) team (Bruns et al., 1987; Johnson and Satake, 1994; Santini et al., 2003; Wells et al., 2003; Wells et al., 2011; Hayes et al., 2012), we are able to dynamically model rupture of a M_w 9 earthquake. The homogeneous model shows an average fault slip of 18.6 m, with the same seismic moment as the source model used by the SAFRR team to investigate large-scale effects on western U.S. coastlines from a tsunami generated along the Alaskan-Aleutian subduction zone, and a maximum vertical free surface displacement of 5.77 m. However, adding a frictional-strengthening zone to an along-strike region of the fault reduces average fault slip to 14.6 m and the maximum vertical free surface displacement to 5.74 m, while significantly reducing the maximum free surface displacement in the area up-dip from the strengthening zone. Adding a frictional-strengthening zone to an updip region of the fault reduces average fault slip to 10.4 m and the maximum vertical free surface displacement to 2.86 m, while significantly reducing the maximum free surface displacement over the entire megathrust. A model with heterogeneous prestress results in a more heterogeneous slip distribution, relative to the homogeneous model; this slip distribution qualitatively matches the slip distribution of the source model used by the SAFRR team. The heterogeneous prestress model has the same average fault slip as the homogeneous model, and a maximum vertical free surface displacement of 7.04 m. Corresponding tsunami models, which use a finite difference method to solve linear long-wave equations (i.e., shallow water equations) (Shuto, 1991; Satake, 2002), match sea floor deformation, in time, to the free surface deformation from the rupture simulations (Tanioka and Satake, 1996). Tsunami models show reduced peak amplitudes in the area above the frictional-strengthening zones, relative to the homogeneous case. A tsunami resulting from a heterogeneous fault prestress model results in peak amplitudes immediately above the hanging wall that are spatially more varied than the homogeneous model, but the overall beaming pattern and maximum amplitudes along the local coasts are similar. All tsunami models also show the resultant gravity wave from the breakout of the earthquake rupture to the sea floor (Oglesby et al., 2000). Tsunamis generated in this region could have large adverse effects on Pacific coasts (Ryan et al., 2012).

2.2 Introduction

Megathrust earthquakes in subduction zones are known generators of large, transoceanic tsunamis (e.g., Kanamori, 1972). Ryan et al. (2012) demonstrated that a tsunami resulting from a large megathrust earthquake on the Alaskan-Aleutian subduction zone (their Figure 1) would propagate across the Pacific Ocean and bombard the U.S west coast, potentially causing significant damage to ports and other populated areas. Due to its earthquake and tsunami hazard, the Alaskan-Aleutian subduction zone has been well studied seismically and geodetically (e.g., Freymueller et al., 2008). Using GPS measurements, Freymueller and Beavan (1999) show that the western Shumagin segment of the Alaskan-

Aleutian subduction zone is creeping (their Figure 1). They further suggest that the entire downdip extent of this section of the megathrust may be unlocked, and thus slipping at the local plate convergence rate. Surface deformation along the Alaskan-Aleutian megathrust is a complex process that results from different mechanisms, including postseismic deformation, spatial variations in plate coupling, and movement of large crustal blocks (Freymueller et al., 2008). Additionally, Freymueller et al. (2008) find that both the width of the seismogenic zone and the distribution of locked and creeping zones vary substantially along strike throughout the Alaskan-Aleutian subduction zone.

The distribution of locked and creeping sections along subduction zones is important for tsunami generation and coastline inundation. Kanamori (1972) notes that sediments in the trench could be a mechanism for tsunami earthquakes – earthquakes that produce relatively small ground shaking but larger than expected tsunamis. Specifically, sediments could alter the frictional properties of the fault, making it a locally creeping (stable sliding) section, as well as producing slower rupture propagation during earthquakes. Hyndman et al. (1997) point out that stable sliding regions can be caused by unconsolidated sediments updip and either higher temperature or hydrated serpentinite at depth, and that global seismogenic zones typically lie between 10 km and 40 km depth. Bilek and Lay (2002) show, for 525 earthquakes around the circum-Pacific including earthquakes along the Alaskan-Aleutian subduction zone, longer rupture durations for shallow (< 15 km) thrust events than for deeper (> 15 km) thrust events. Furthermore, they suggest that conditionally stable and fully stable sliding zones located on the most updip section of a thrust fault can be a valid mechanism to slow rupture velocity and increase duration.

Dynamic rupture models of dip-slip faults are extremely helpful in understanding the free surface deformation that leads to tsunami generation. Specifically, using seafloor deformation from rupture dynamics as time-dependent boundary conditions for tsunami generation may provide insight into tsunami formation and local propagation. Standard dislocation models use a static slip distribution to model the resulting tsunami (Okada, 1985), while for dynamic models the slip distribution is not known before hand, rather, it is a calculated result of the model. Dynamic models can validate existing dislocation models by using realistic friction parameterizations and fault geometry to match the slip distribution of the dislocation model and to analyze the resulting tsunami in time. Although dynamic modeling cannot replace the utility of standard dislocation modeling, it can be a useful complement.

Numerical and experimental models show that dip-slip faults exhibit normal stress fluctuations from seismic wave reflections off the free surface (Brune, 1996; Nielsen, 1998; Oglesby et al., 1998; Oglesby and Archuleta, 2000; Oglesby et al., 2000). For non-vertical dip-slip faults, the free surface allows seismic waves to reflect back and hit the fault again, altering the stress field on the fault near the free surface. Oglesby et al. (1998) show that as rupture approaches the free surface along a thrust/reverse fault, there is an increase in normal stress ahead of the crack tip and a decrease in normal stress behind the crack tip; this effect leads to amplified fault motion near the surface (relative to a normal or strike-slip fault rupture). Furthermore, when rupture travels updip along a dip-slip fault and reaches the free surface, it produces a breakout phase (a slip pulse traveling back downdip) and a strong Rayleigh wave traveling along the surface (Burridge and Halliday, 1971; Oglesby et al., 1998), with reverse/thrust faults having stronger breakout phases than normal or strike-slip faults. The particle displacement is also greatly enhanced on the hanging wall relative to the footwall. In agreement with numerical models, Brune's (1996) laboratory thrust foam block models also produce these effects. Enhanced slip near the trench is capable of generating larger amplitude tsunamis than equivalent slip at depth (Geist, 1998; Geist and Bilek, 2001; Geist, 2002).

In the first part of this work, we use the dynamic finite element code FaultMod (Barall, 2009) to show that simple slip-weakening friction (e.g., Ida, 1972) can serve as a very accurate proxy for rate-strengthening friction as derived from the rate-state framework (Dieterich, 1978, 1979; Ruina, 1980, 1983; Linker and Dieterich, 1992). With this approach to friction thus validated, we then use the dynamic finite element code EQDyna (Duan and Oglesby, 2006) to model 3-D ruptures, using time-weakening friction (Andrews, 2004), along a megathrust approximating a portion of the Alaskan-Aleutian subduction zone. We parameterize time-weakening friction as a proxy for rate-strengthening friction. In order to model megathrust faults more realistically, it is important to simulate unstable and stable sliding zones (e.g., outer boundaries of seismogenic zones); such models typically use a rate- and state-dependent (RS) friction parameterization (e.g., Hyndman et al., 1997; Scholz, 1998) to capture the physics of slip under varying degrees of frictional stability. In particular, an increase in the steady-state friction coefficient with slip rate can characterize the stable sliding zones that border the seismogenic zones.

The general form of RS friction is (Dieterich, 1978, 1979; Ruina, 1980, 1983):

$$\tau = \left[\mu_0 + a\ln\left(\frac{V}{V_0}\right) + b\ln\left(\frac{\theta}{\theta_0}\right)\right]\sigma_{\text{eff}} \tag{2.1}$$

where τ is the shear stress, μ_0 represents a constant reference value for the coefficient of friction; a and b are constitutive parameters estimated from laboratory experiments; V_0 and θ_0 are reference values for slip rate and the state of the sliding surface, respectively, such that when $V = V_0$ and $\theta = \theta_0$ the friction coefficient is μ_0; θ abstractly represents the average age of contacts at some sliding velocity; and σ_{eff} is the effective normal stress. Within the RS formulation, a positive rate-strengthening parameter $(a - b)$, where a and b are experimentally determined (Dieterich, 1978, 1979) through observed stress drop, indicates velocity strengthening or stable slip, and a negative parameter indicates velocity weakening or the potential for unstable slip. For reverse/thrust faults it has been suggested that such rate-strengthening zones can simulate weak zones in the inner margin of the trenches, possibly characterized by large amounts of sedimentation. Sliding experiments on ultrafine-grained quartz (Chester and Higgs, 1992) suggest that rate-weakening behavior occurs between 100^o and 300^o C under wet conditions, while higher temperatures lead to a rate-strengthening parameter $(a-b)$ of 0.03. Experiments on granite (Blanpied et al., 1998) found rate-weakening at lower slip speeds (e.g., 1 $\frac{\mu m}{s}$) with a rate-strengthening parameter of approximately 0.004 and rate-strengthening at higher slip speeds (e.g., 1000 $\frac{\mu m}{s}$) with a rate-strengthening parameter of approximately 0.01.

Real faults likely have heterogeneous stress regimes in addition to distributed frictionally stable and unstable sliding zones; these features can lead to complex stress interactions during rupture. In order to reproduce accurate slip distributions from real earthquakes, dynamic modeling studies incorporate heterogeneous prestress distributions (e.g., Olsen et al., 1997; Peyrat et al., 2001; Guatteri et al., 2003; Olsen et al., 2009). However, the resulting total slip distributions typically are much smoother than prestress distributions, due to stress interactions from large portions of the fault slipping simultaneously. Beroza and Mikumo (1996) suggest that slip duration for a point on a fault can decrease in cases of high prestress heterogeneity due to a self-healing mechanism. Thus, modeling earthquakes with heterogeneous prestress should result in both heterogeneous rupture propagation (i.e., highly variable rupture speed) and heterogeneous slip distributions.

Tsunami generation and propagation are influenced by the slip distribution, geometry, and material properties along the tsunami-generating fault (Geist, 1998; Geist and Dmowska, 1999; Geist and Bilek, 2001; Geist, 2002). These studies indicate that slip distribution near the trench most significantly affects tsunami generation, amplitude and local runup, versus slip distribution further downdip. Geist and Dmowska (1999) show that dip-directed slip variations affect the maximum amplitude and steepness of the local tsunami, whereas along-strike slip variations result in strike-parallel amplitude changes in the tsunami that are conserved during local propagation, altering the beaming pattern of the tsunami. Geist and Bilek (2001) point out that estimates of initial tsunami size depend on shear modulus estimates with depth. They analyzed 360 circum-Pacific subduction zone earthquakes and found that in order to match observed source time functions, a relative reduction in shear modulus as well as an increase in slip near the trench is needed.

Additionally, megathrust earthquakes can incorporate complex slip distributions on multiple fault segments. Thrust events involving rupture of a splay fault can greatly affect the distribution of seafloor deformation and the resultant tsunami (Cummins and Kaneda, 2000). DeDontney and Rice (2012) suggest that the 2004 Indian Ocean tsunami may have resulted from two major areas of uplift, the main thrust and a splay fault, and further note that splay faults with steeper dip angles require less slip to produce the same vertical seafloor deformation as the main thrust fault. Whether or not a rupture can propagate onto a splay fault can depend on the dynamics of the earthquake (Wendt et al., 2009). Wendt at al. (2009) dynamically modeled the time-dependent earthquake and tsunami generation process, on a large thrust fault with a connected, steeper splay fault. They show that if a barrier is introduced on the main thrust fault, rupture can propagate onto the smaller splay fault and produce larger vertical seafloor deformation and correspondingly larger (local) maximum tsunami wave heights.

2.3 Method Part 1: Friction Parameterizations

In this study we simulate zones of weak fault coupling for an updip portion and for an along-strike portion of the Alaska-Aleutian megathrust (Figure 2.2). Although the primary finite element method (FEM) code EQDyna (Duan and Oglesby, 2006) used in this study can model 3-D, shallow dipping, megathrust ruptures, it does not incorporate rate-state friction. Thus, in order to approximate rate-strengthening frictional properties from rate-state friction using a simple slip-weakening-type friction formulation (e.g., time-weakening friction, Andrews, 2004), we test three different friction laws using a secondary 2-D FEM code FaultMod (Barall, 2009) that does incorporate rate-state friction: linear slip-weakening (SW) friction and two forms of rate- and state-dependent friction: ageing law (RS-AL), and slip law (RS-SL). We use results from the secondary code FaultMod to model mode II (slip parallel to rupture propagation) dynamic rupture, with a frictional interface, along a planar fault in a half space (Figure 2.1, top). Generally, finite element codes divide a given continuum of mass (e.g., the Earth's surface) into a number of elements that can then be used to run computations on applied forces, assuming elasticity and a frictional parameterization. FaultMod has been validated in SCEC/USGS rupture benchmark problems (Barall, 2009; Harris et al., 2009; Harris et al., 2011). The code incorporates artificial viscous damping (Dalguer and Day, 2007) as well as algorithmic damping to help damp spurious oscillations, and energy-absorbing boundary conditions along the mesh edges to avoid artificial reflections from the model boundaries.

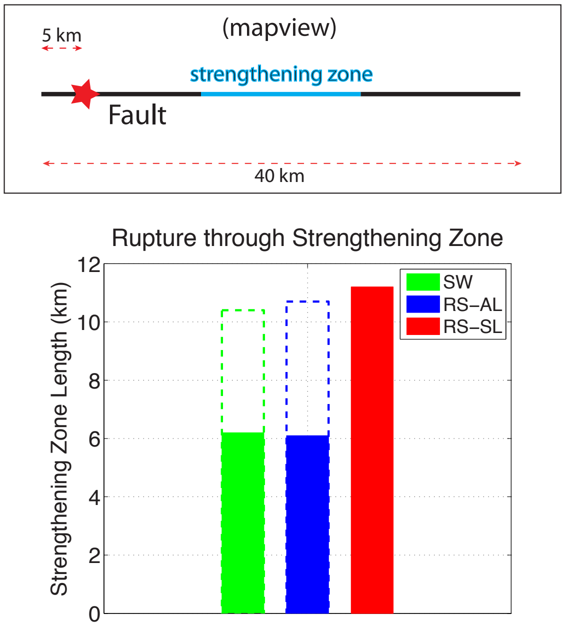

Figure 2.1: (top) We model a frictional-strengthening zone in the middle of a homogeneous, planar, 2-D fault in a whole space using slip-weakening (SW), rate-state ageing law (RS-AL), and rate-state slip law (RS-SL) friction parameterizations in finite element code FaultMod. The red star denotes the nucleation zone (1.5 km radius). We increase the size of the strengthening zone, for each friction formulation, until rupture cannot tunnel through the entire strengthening zone. (bottom) SW (green) and RS-AL (blue) models tunnel through similar maximum-sized strengthening zones with equivalent slip-weakening distances (solid bars), while SW (green), RS-AL (blue), and RS-SL (red) models tunnel through similar maximum-sized strengthening zones with equivalent fracture energy (dashed bars). For our models, the condition for strengthening using slip-weakening friction is eq. 2.8.

The criterion for linear slip-weakening friction is as follows (Ida, 1972):

$$\mu = \begin{cases} \frac{\mu_k - \mu_s}{d_0} u + \mu_s, & \text{if } u < d_0 \\ \mu_k, & \text{if } u \geq d_0 \end{cases} \tag{2.2}$$

where u is the cumulative slip, and where the friction coefficient μ drops from a static value to a kinetic value over a slip-weakening distance d_0.

Following Lapusta et al. (2000), we use a modified form of the bracketed term in eq. 2.1 that does not become singular for very small slip velocities:

$$\mu = a \operatorname{arcsinh}\left[\frac{V}{2V_0} e^{\left(\frac{\mu_0+\psi}{a}\right)}\right] \approx \mu_0 + a \ln\left(\frac{V}{V_0}\right) + \psi. \tag{2.3}$$

This form of the RS law closely approximates eq. 2.1 for slip velocities of seismological interest. Note that the right hand side of eq. 2.3 has the form of the effective friction coefficient in eq. 2.1 with $\psi = bln\left(\frac{\theta}{\theta_0}\right)$, or conversely, $\theta = \theta_0 e^{\left(\frac{\psi}{b}\right)}$. Conceptually, ψ represents the strength of contacts. For the RS-AL, the state variable evolves according to the equation:

$$\frac{d\theta}{dt} = \frac{-1}{\theta_{ss}}\left(\theta - \theta_{ss}\right). \tag{2.4}$$

In the RS-SL, the state variable evolves according to the equation

$$\frac{d\psi}{dt} = \frac{-V}{L}\left(\psi - \psi_{ss}\right). \tag{2.5}$$

Both the RS-AL (eq. 2.4) and the RS-SL (eq. 2.5) reduce to the standard formula for steady-state sliding:

$$\psi_{ss} = -b \ln\left(\frac{V}{V_0}\right). \tag{2.6}$$

Rupture is constrained to take place on a 40 km fault (Figure 2.1, top). We add a frictional-strengthening zone to the center of the fault. For the rate-state simulations this is a rate-strengthening zone governed by the steady state equation

$$\frac{d\mu_{ss}}{d\ln V} = a - b \tag{2.7}$$

such that when constitutive parameter b is larger than constitutive parameter a, the steady state friction value decreases as velocity increases, and thus represents a velocity-weakening zone. However, when constitutive parameter b is smaller than constitutive parameter a, the steady state friction value increases with increasing velocity, and represents a velocity-strengthening zone. Dieterich (1978; 1979) experimentally determined a and b values to be on the order of 0.01; we use values of 0.008 and 0.012 for parameters a and b, respectively, to simulate rate-weakening. We use values of 0.016 and 0.012 for parameters a and b, respectively, to represent a region of rate-strengthening. The length of strengthening zone is variable and allows us to determine the maximum strengthening zone length rupture can tunnel through for each of the three friction laws. We find that the friction coefficients in linear slip-weakening (SW) friction can be tuned to match the rate-state models, so that each friction law tunnels through a similar-sized strengthening zone. Specifically, by analyzing stress-versus-slip weakening curves for the rate-state models within the rate-strengthening zones and within the rate-weakening zones (black segments in Figure 2.1), we tune μ_s and μ_k so that the three friction laws have similar stress-versus-slip weakening curves. For equivalent slip-weakening distances, both SW friction and RS-AL models can tunnel through similar-sized strengthening zone lengths (Figure 2.1, bottom) and result in similar slip distributions. We note that the relatively nonlinear RS-SL tunnels though larger strengthening zones, but that with equivalent fracture energy (Andrews, 1976, Guatteri and Spudich, 2000) all three models tunnel through similar-sized zones and result in similar slip distributions. The general equation required by SW friction to match RS formulations in the strengthening zone is

$$\tau_0 < \mu_k \sigma_0 \tag{2.8}$$

where τ_0 is the initial shear stress, μ_k is the kinetic friction coefficient, and σ_0 is the initial normal stress. Thus, we have found a useful approximation for rate-strengthening friction using a simpler slip-weakening formulation. Note that this is not the same as slip-hardening, which requires the kinetic friction coefficient to be larger than the static friction coefficient. In this study, we simulate rate-strengthening behavior by altering μ_k within the strengthening zones. Under our configuration, shear stress will ultimately increase with slip, assuming no normal stress change. However, dip-slip faults involve dynamic normal stress fluctuations, including reductions that could result in a shear stress drop even in the presence of rate-strengthening.

2.4 Method Part 2: Earthquake and Tsunami Models

In this study we use the 3-D finite element method (FEM) code EQDyna (Duan and Oglesby, 2006) to model mode II dynamic rupture, with a frictional interface along a megathrust intersecting the free surface (Figure 2.2, top), and the corresponding free surface deformation. Rupture is constrained to take place only on the fault. The megathrust is 358 km along strike, 205.1 km downdip, and 35.6 km in depth, with a constant dip angle of 10^o (Kirby et al., 2013). EQDyna also has been validated in SCEC/USGS rupture benchmark problems (Harris et al., 2009; Harris et al., 2011). The code incorporates artificial damping (Duan and Day, 2007) to help reduce spurious oscillations. Additionally, we implement a large enough buffer around the fault so that a P-wave cannot travel to the edge of the model and back to the fault within the model duration, 200 s. We consider fault ruptures with model and material properties given in tables 2.1 and 2.2.

We note that the nucleation zone (shown as a red star in Figure 2.3) used in all models in this study has a radius of 16 km (as indicated by Table 2.1). The nucleation zone size is small relative the size of the modeled megathrust, and does not significantly affect the overall slip distribution in our models; for example, there are no obvious asymmetric slip patterns near or around the nucleation zone in Figure 2.6. Additionally, we implement a finite element size of approximately 2 *km* along the modeled fault. Decreasing the element size is not possible due to computational limitations. However, we have tested smaller fault models (34 *km* along strike and 20 *km* downdip) – with the same homogeneous input parameters used in this study – for grid-size dependent results. We found similar slip distributions, slip rates, and rupture velocities for these earthquake models using 0.5 *km*, 1 *km*, 1.5 *km*, and 2 *km* element sizes. We therefore assume that a 2 *km* element size is reasonable and appropriate in this study of a much larger modeled fault, although we cannot directly test this. For simplicity we use a homogeneous material structure with average mid-crustal material properties (e.g., Harris et al., 2009), although future models will incorporate 3-D material structure heterogeneity. We use a time-weakening friction law (Andrews, 2004; Duan and Day, 2008), in which the stress at a point drops from its static to sliding frictional level over a characteristic time. This friction law produces behavior similar to that of slip-weakening friction, with an effective slip-weakening distance d_0 that is proportional to the square root of rupture velocity multiplied by the distance rupture has propagated:

$$d_0 \propto \frac{\Delta\tau}{G}\sqrt{\frac{V_{rupt} t_0 L}{k}} \tag{2.9}$$

where $\Delta\tau$ is the stress drop, G is the shear modulus, V_{rupt} is the rupture velocity, t_0 is the time over which the friction coefficient drops from its static value to its kinetic value, L is

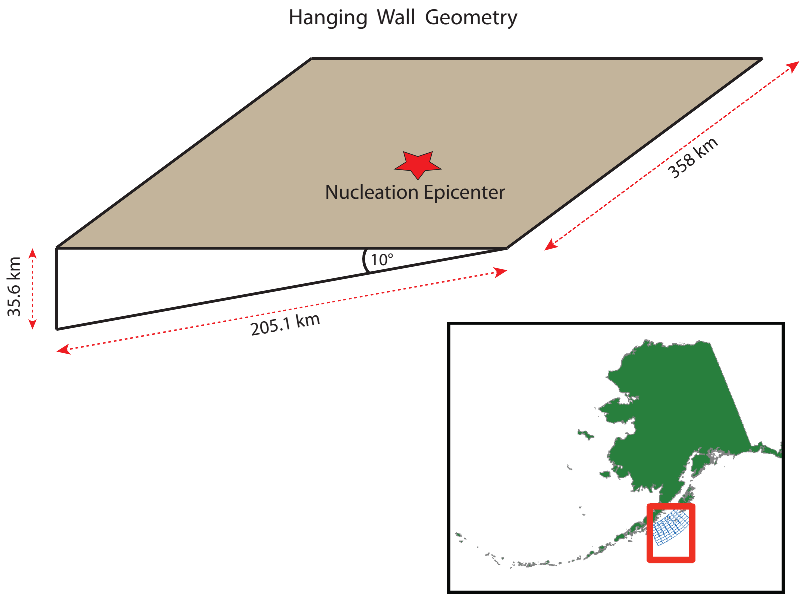

Figure 2.2: (top) Cartoon fault geometry of the hanging wall using 3-D finite element code EQDyna (Duan and Oglesby, 2006). We use a planar fault geometry with a constant dip of 10^o, an along-strike distance of 358 km, a depth of 35.6 km, and a downdip distance of 205.1 km. The fault intersects the free surface. Each element along the fault surface is approximately 2 km along strike and 2 km downdip. Additionally, we implement a buffer zone around the fault to ensure waves do not reflect off the model boundary and return to the fault. (bottom-right) Geographic region of interest with the section of the Aleutian-Alaskan megathrust we are approximating (image from SAFRR Earthquake Source working group).

the distance rupture has propagated, and with different values of k depending on the shape of the stress-slip weakening curve. As recommended by Andrews (2004), we use a time-weakening value t_0 that is the amount of time it would take for an S-wave to traverse more than three elements (we use 5 elements) along the fault interface. This parameterization allows us to achieve accuracy and smoothness of the breakdown zone as the rupture front increases in speed and amplitude away from the nucleation zone. As noted above, the computer code EQDyna does not incorporate rate- and state-dependent friction, so we use time-weakening friction with eq. 2.8 as a proxy for rate-strengthening-like zones.

Table 2.1: Model and material properties for all simulations in this study.

Density	2670 kg/m^3
Shear Modulus	40.00 GPa
Bulk Modulus	66.67 GPa
S-wave speed	3.871 km/s
P-wave speed	6.704 km/s
Fault Area	73,426 km^2
Nucleation Depth	15.50 km
Nucleation Radius	16.00 km
Nucleation Speed	2.000 km/s
Nucleation Location (along strike)	22.38 km
Nucleation Location (downdip)	-89.26 km
Element Size (along fault)	≈2 km
Time Step	0.01 s
Distance Along-Strike	358.0 km
Distance Downdip	205.1 km
Dip Angle	10°
t_o	2.600 s
Hydrodynamic Grid Size	2 km
Hydrodynamic Time Step	0.1 s

In this study we use four different rupture models: a spatially-constant prestress and frictional coefficient model (hereinafter referred to as the homogeneous model), two models with frictional-strengthening zones, and a spatially-heterogeneous prestress model. For frictional-strengthening zone models, we use eq. 2.8 with time-weakening friction to simulate rate-strengthening-like zones on updip and along-strike portions of the megathrust (Figure 2.3, see Table 2.2 for friction coefficients). Specifically, we implement frictional-strengthening zones in either the western-most portion of the fault (100 km to 179 km along strike) or the updip-most portion of the fault (0 km to -50 km downdip). As an example of how time weakening in these models corresponds to either rate-weakening or

Table 2.2: Initial shear stress τ_0, initial normal stress σ_0, the static friction coefficient μ_s, the kinetic friction coefficient μ_k, and the strengthening friction coefficient μ_k (strength) (if applicable) for all four models in this study.

	τ_o [MPa]	σ_o [MPa]	μ_s	μ_k	μ_k (strength)
Homogeneous Prestress/Friction	3.172	11.06	0.5630	0.1333	
West Frictional-strengthening	3.172	11.06	0.5630	0.1333	0.3218
Updip Frictional-strengthening	3.172	11.06	0.5630	0.1333	0.3218
Heterogeneous Prestress	0 – 24.26	1.090 – 84.60	0.5630	0.1333	

rate-strengthening, Figure 2.4 shows stress-slip weakening curves for a point in a frictional-weakening zone and a point in a frictional-strengthening zone for the western frictional-strengthening zone model (locations marked in Figure 2.8). There is a clear stress drop from the initial stress in the weakening zone, and a stress increase in the strengthening zone. However, we note that a stress increase may not occur for all points in our frictional-strengthening zone, since large dynamic reductions in normal stress can still result in a shear stress drop during sliding. For the heterogeneous prestress model, we divide the fault into 64 subfault sections, each section with a different prestress. The objective of this model is to qualitatively match the slip distribution used by the Earthquake Source working group within the SAFRR Tsunami Scenario team (Kirby et al., 2013). Previous studies show that scaling the prestress distribution in dynamic earthquake models is one way to match observed slip distributions (e.g., Olsen et al., 1997; Olsen et al., 2009).

A dynamic finite element code produces not just a rupture pattern on a fault; it also produces the full wave field and surface deformation. After dynamically modeling earthquake rupture, we feed the resulting time-dependent free surface (i.e., seafloor) dis-

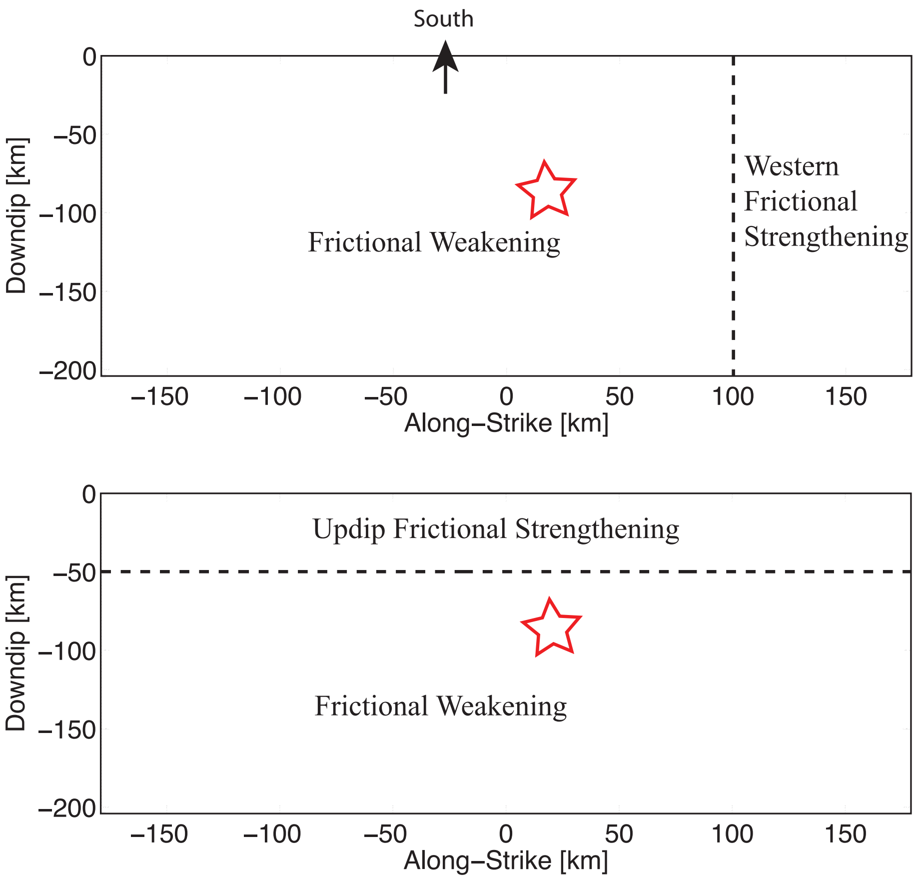

Figure 2.3: We implement two models with frictional-strengthening zones in the (top) western most portion and the (bottom) updip most portion of the fault. Note that the point of view is from above the hanging wall, perpendicular to the fault surface. Stars indicate the nucleation zone that is at the same location for all models. The strengthening areas are $16,203\ km^2$ and $17,900\ km^2$ for the top and bottom models, respectively. See Table 2.2 for frictional coefficients.

placements into a hydrodynamic code using a 2-D (i.e., waves propagate in two spatial dimensions) finite difference method to solve linear long wave equations (Shuto, 1991; Satake, 2002). In this way, we may model the generation of a tsunami from our dynamic earthquake models. Specifically, time dependent 3-D seafloor deformation from our earthquake models is used as a time-dependent boundary condition for our hydrodynamic models, assuming that the water surface is displaced due to the combined effects from vertical and horizontal

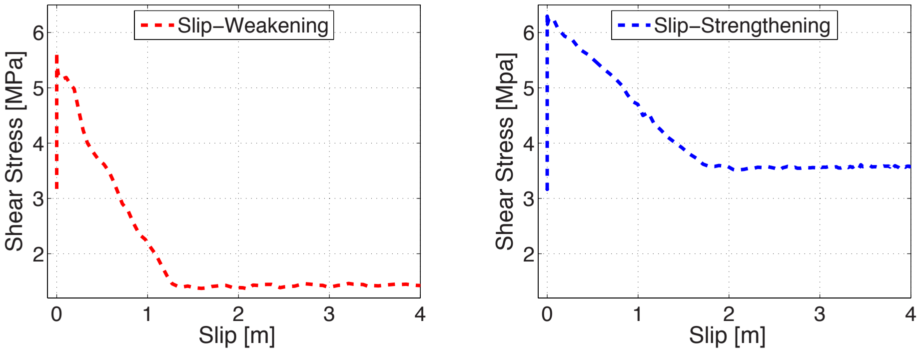

Figure 2.4: Shear stress-versus-slip weakening curves for a point in the weakening zone (red, left) and a point in the strengthening zone (blue, right), using time-weakening friction to model a 3-D megathrust earthquake within the Alaskan-Aleutian subduction zone. Point locations are marked by red and blue stars in Figure 2.8 below (3rd panel down). Results show a decrease in shear stress within the frictional-weakening zone, and an increase in shear stress in the frictional-strengthening zone. Note that shear stress depends on both friction coefficient and normal stress during sliding.

seafloor displacement (Tanioka and Satake, 1996). The leap-frog, finite difference method of computing of tsunami propagation, described by Satake (2007), is used with the ETOPO1 digital elevation model (http://www.ngdc.noaa.gov/mgg/global/global.html). Incorporation of both dynamic codes allows us to simulate tsunami formation and local propagation in time. Hydrodynamic model parameters are given in Table 2.1.

2.5 Results

In this study we focus on rupture dynamics, fault slip distribution, free surface deformation, and the resulting tsunami for four different models: a homogeneous set of prestress and frictional conditions, a western frictional-strengthening zone, an updip frictional-strengthening zone, and a heterogeneous prestress condition (Figures 2.3 through 2.17). Both the homogeneous and heterogeneous prestress models match the seismic moment of the dislocation model determined by the Earthquake Source working group within the SAFRR Tsunami Scenario team (Kirby et al., 2013). For each model, differences in the rupture dynamics ultimately result in different tsunami formations, local maximum water wave amplitudes, and tsunami beaming patterns. We note two key parameters: the maximum vertical free surface displacement Z_{max} and the average fault slip $<S>$ for each model (Table 2.3) that affect maximum tsunami height and the initial tsunami height distribution.

Table 2.3: Maximum vertical free surface displacements Z_{max} and average fault slip $<S>$ for all four models in this study.

	Z_{max} [m]	**<S> [m]**
Homogeneous Prestress/Friction	5.77	18.6
West Frictional-strengthening	5.74	14.6
Updip Frictional-strengthening	2.86	10.4
Heterogeneous Prestress	7.04	18.6

2.5.1 Homogeneous Stress and Friction

Figure 2.5 shows slip-rate snapshots of the homogeneous earthquake rupture at 27 s, 52 s, and 70 s into the simulation. The fault experiences large slip rate pulses near the free surface due to dynamic unclamping of the fault and geometric asymmetry of the hanging wall/footwall (Brune, 1996; Nielsen, 1998; Oglesby et al., 1998; Oglesby and Archuleta, 2000; Oglesby et al., 2000), resulting in a strong breakout phase and the generation of an oceanic Rayleigh wave. Rupture proceeds over the entire fault zone. Fault slip (top) and total vertical free surface deformation (bottom) for the homogeneous model are shown in

Figure 2.6. The largest amount of slip is near the surface, corresponding to large vertical displacement on the surface near the fault trace. Average fault slip is 18.6 m, and maximum vertical surface displacement is 5.77 m. Figure 2.7 displays local peak tsunami amplitude resulting from the homogeneous earthquake rupture model, in the geographic region of interest. Water height corresponds well with free surface deformation, and the largest tsunami amplitudes are located closest to the trench. In the model, the Shumagin Islands, Alaska Peninsula, and Kodiak Island are particularly hit with large wave height from the local tsunami. The tsunami amplitude has a strong southward beaming effect, indicating potential damage to coastlines in Hawaii and the western U.S. as well as other coastlines around the Pacific rim in the simulation.

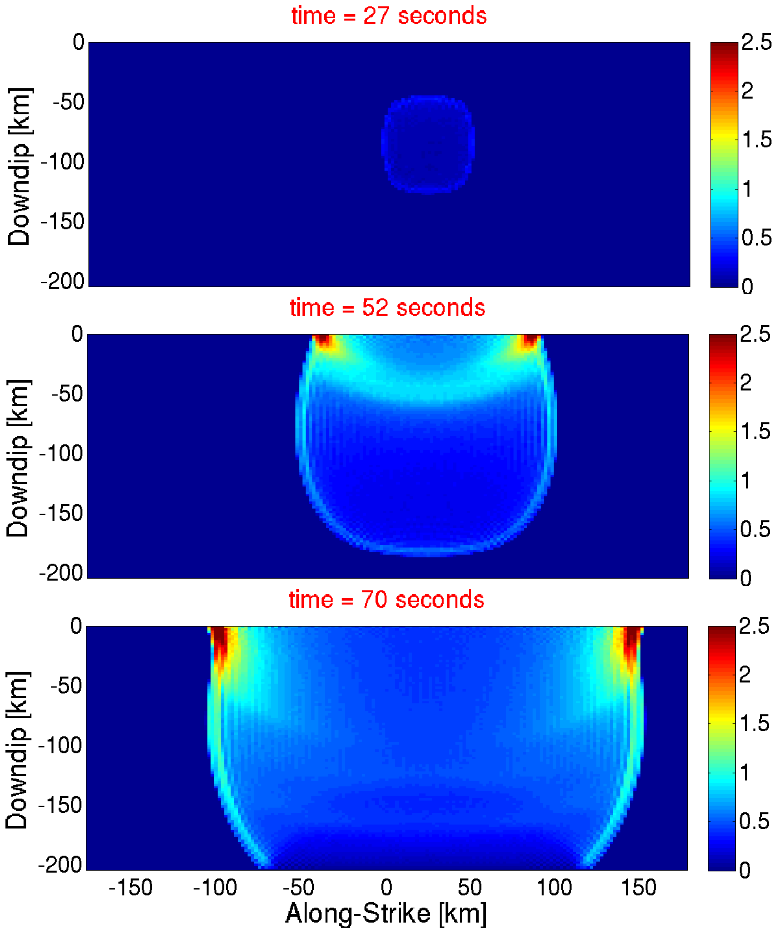

Figure 2.5: Snapshots of slip rate (i.e., rupture propagation) in $\frac{m}{s}$ for a homogeneous (spatially-constant prestress, dip angle, and frictional coefficients) model. Rupture shows large slip rate pulses nearest the free surface. Rupture proceeds over the entire fault zone (entire region shown), beginning at the nucleation zone (indicated in Figure 2.3).

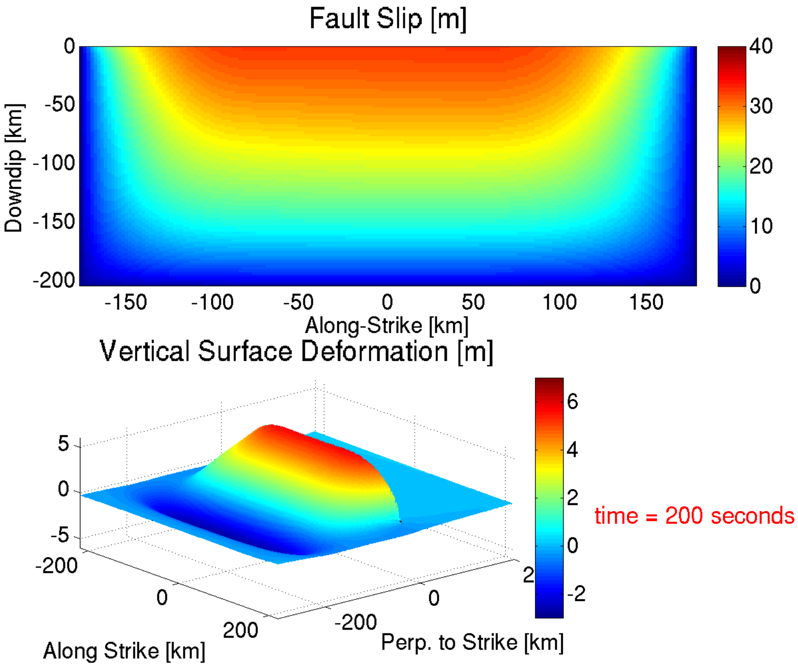

Figure 2.6: Fault slip (top) and total vertical free surface deformation (bottom) for the homogeneous model. The largest amount of slip is near the surface, corresponding to large vertical displacement on the surface near the fault trace. Average fault slip is 18.6 m, and maximum vertical surface displacement is 5.77 m.

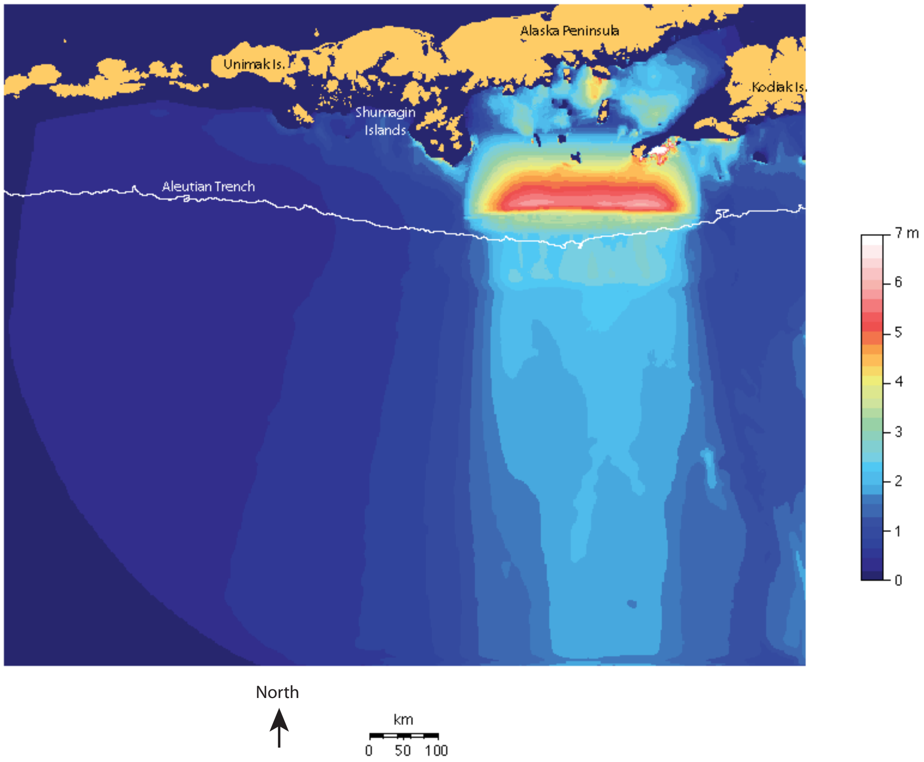

Figure 2.7: Peak tsunami amplitudes resulting from the homogeneous earthquake rupture model in the geographic region of interest. The white line represents the Aleutian trench. Water height corresponds well with free surface deformation (Figure 2.6, bottom). The Shumagin Islands, Alaska Peninsula, and Kodiak Island are particularly bombarded with large water height from the local tsunami. Additionally, the tsunami amplitude has a strong southward beaming effect.

2.5.2 Western Frictional-Strengthening Zone Rupture

The above model assumes homogeneous frictional conditions along the entire extent of the fault. Realistically, however, faults are likely heterogeneous in frictional properties as well as in their initial stress conditions. GPS models show an unlocked (plate) section that borders our study area to the west known as the Shumagin Gap (Freymueller and Beavan, 1999; Freymueller et al., 2008). In an effort to incorporate a more realistic frictional regime, we implement a frictional-strengthening zone in the western-most 79 *km* of the megathrust (Figure 2.3, top) as a proxy that characterizes the Shumagin creeping section. Figure 2.8 shows slip-rate snapshots of rupture propagation for a model with a western frictional-strengthening zone. This model shows large slip rate pulses nearest the free surface like the homogeneous model, however, the strengthening zone diminishes the slip rate pulse significantly relative to the homogeneous model. Note the difference in slip rate between the two models at 70 s. Rupture proceeds over the entire fault, including through the strengthening zone. The largest slip in the strengthening zone occurs near the free surface, most likely due to dynamic unclamping and the geometric asymmetry near the free surface. We note that the extent that rupture can penetrate a frictional-strengthening zone depends on fault geometry, friction coefficients, initial stress regimes, and location of the nucleation zone. While a strengthening zone in principle releases no seismic energy, slip can still occur, and is driven by seismic energy released on other (weakening) parts of the fault. Figure 2.9 illustrates fault slip (top) and total vertical free surface deformation (bottom) for the western frictional-strengthening zone model. Average fault slip is decreased by 4 m (18.6 to 14.6 m), relative to the homogeneous model. Surface deformation is substantially decreased in the region above the strengthening zone, relative to the homogeneous model; however, the maximum vertical surface displacement is decreased only marginally (from 5.77 to 5.74 m). The local peak modeled tsunami amplitudes resulting from the western frictional-strengthening zone model are shown in Figure 2.10. Water height corresponds well with vertical free surface deformation, with the largest tsunami amplitude distributed above the frictional-weakening zone. Converting a western portion of the fault to a frictional-strengthening zone greatly reduces tsunami amplitude locally north of the strengthening zone in the Shumagin Islands region of the heterogeneous model, and redirects the beaming pattern of the basin-propagating (far-field) tsunami slightly in a counterclockwise direction, but with similar maximum amplitude, relative to the homogeneous model.

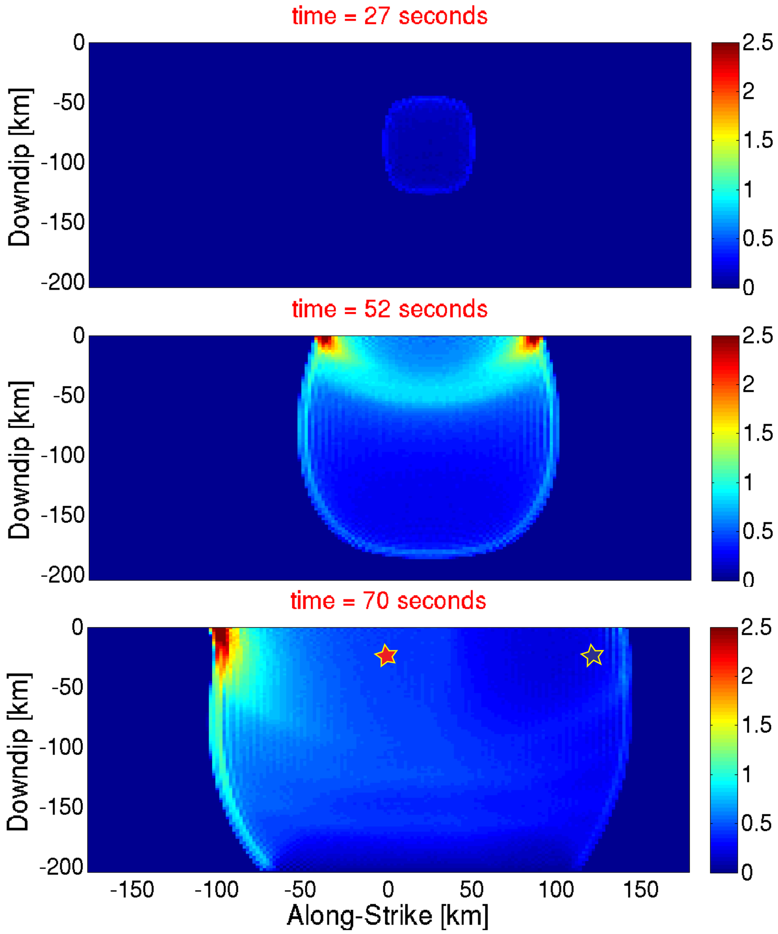

Figure 2.8: Snapshots of slip rate (i.e., rupture propagation) in $\frac{m}{s}$ for a model with a frictional-strengthening zone from 100 to 179 km along-strike and over the entire downdip extent of the model (see Figure 2.3, top), motivated by GPS models showing an unlocked (plate) section that borders our study area to the west (Freymueller and Beavan, 1999). Rupture shows large slip rate pulses nearest the free surface, however, the strengthening zone diminishes the slip rate pulse substantially, relative to the homogeneous model. Note the difference in slip rate between this model and the homogeneous model at 70 s. Rupture proceeds over the entire strengthening zone. The red and blue stars correspond to the sampling points for the stress weakening plots in Figure 2.4.

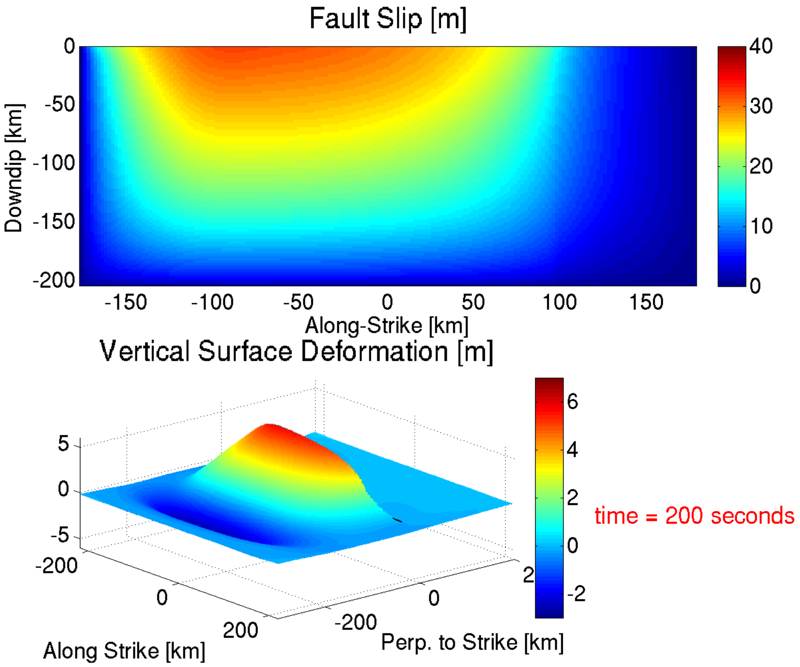

Figure 2.9: Fault slip (top) and total vertical free surface deformation (bottom) for the western frictional-strengthening zone model. Average fault slip is decreased by 4 m (18.6 to 14.6 m) in the strengthening model, relative to the homogeneous model. Surface deformation is substantially decreased in the region above the strengthening zone, relative to the homogeneous model; however, the maximum vertical surface displacement is decreased marginally (5.77 to 5.74 m).

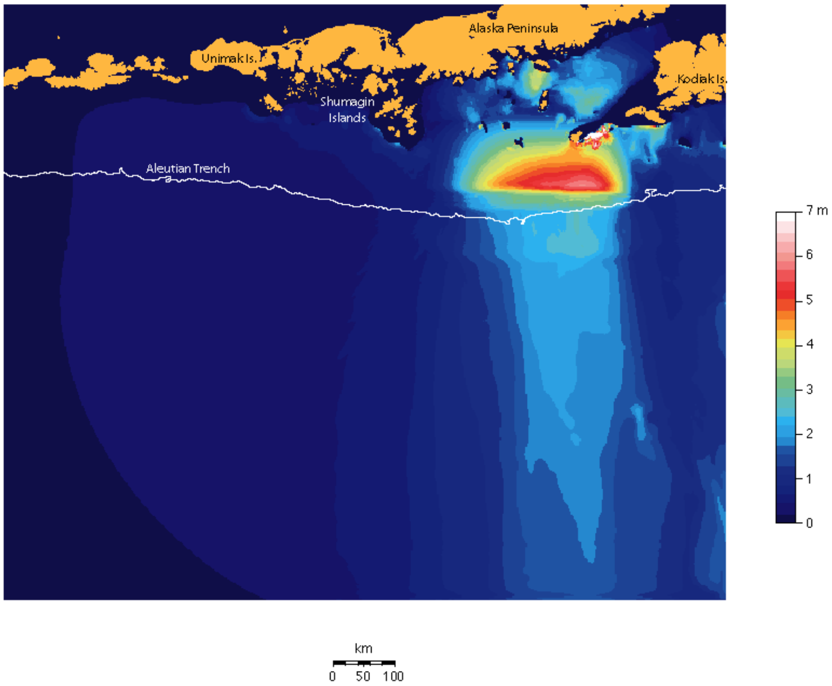

Figure 2.10: Peak tsunami amplitudes resulting from the western frictional-strengthening zone model. Water height corresponds well with free surface deformation (Figure 2.9, bottom). Converting a western portion of the fault to a frictional strengthening zone greatly reduces tsunami amplitudes locally above the strengthening zone in the Shumagin Islands region and alters the beaming pattern of the basin-propagating (far-field) tsunami to a more counterclockwise direction, relative to the homogeneous model. Also, peak amplitudes are reduced near the coasts of the Shumagin Islands.

2.5.3 Updip Frictional-Strengthening Zone Rupture

It has been suggested that subduction zones can have frictional-strengthening regimes close to the trench due to material and frictional properties (e.g., Kanamori, 1972; Hyndman et al., 1997). As a first-order effort to model such a frictional regime, we implement a frictional-strengthening zone in the updip-most 50 km of the megathrust (Figure 2.3, bottom). Figure 2.11 shows slip-rate snapshots for this model. In contrast to the models discussed above, the fault experiences its largest slip rate pulses at roughly 100 km downdip from the free surface, and the slip rate pulse is dramatically reduced over the entire fault relative to the homogeneous model. Note the difference in slip rate between the homogeneous and updip frictional-strengthening models at 52 and 70 s. Rupture proceeds over the entire fault, including through the strengthening zone. Within the strengthening zone, the largest slip rates occur along the free surface. Figure 2.12 displays fault slip (top) and total vertical free surface deformation (bottom) for the updip frictional-strengthening zone model. Average fault slip is decreased by 8.2 m (18.6 to 10.4 m) in the updip strengthening model, relative to the homogeneous model. Surface deformation is decreased broadly along the free surface, relative to the homogeneous model, and the maximum vertical surface displacement is decreased (5.77 to 2.86 m). Adding an updip frictional-strengthening zone reduces slip across the entire fault more than a western strengthening zone with similar area and the same frictional coefficients. Local peak tsunami amplitudes resulting from the updip frictional-strengthening zone model are shown in Figure 2.13. Water height corresponds well with vertical free surface deformation, showing a broad decrease in the local maximum tsunami height, compared to the homogeneous model. Adding a strengthening zone to the updip portion of the fault greatly reduces tsunami amplitudes locally above the strengthening zone near the trench, and reduces the maximum amplitude of the southward beam, but does not change the beam direction of the far-field tsunami, relative to the homogeneous rupture.

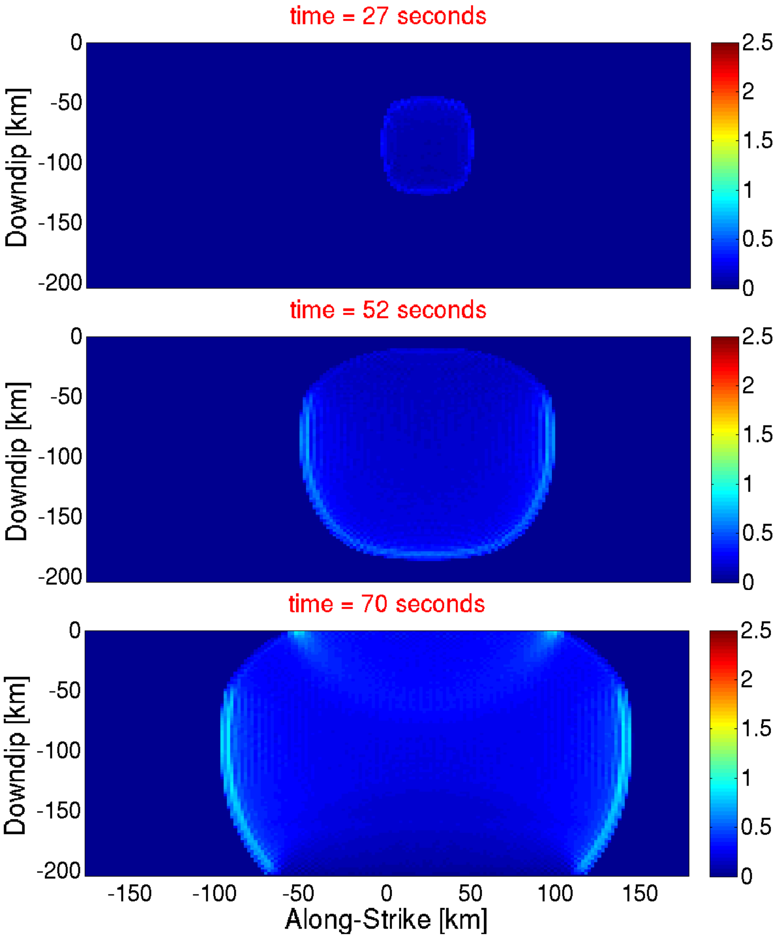

Figure 2.11: Snapshots of slip rate (i.e., rupture propagation) in $\frac{m}{s}$ for a model with a frictional-strengthening zone from 0 to -50 km downdip and across the entire along-strike extent of the model (see Figure 2.3, bottom). Rupture shows largest slip rate pulses around 100 km downdip from the surface, and the slip rate pulse is dramatically reduced over the entire fault, relative to the homogeneous model. Note the difference in slip rate between this and the homogeneous models at 52 and 70 s. Rupture proceeds through the entire strengthening zone.

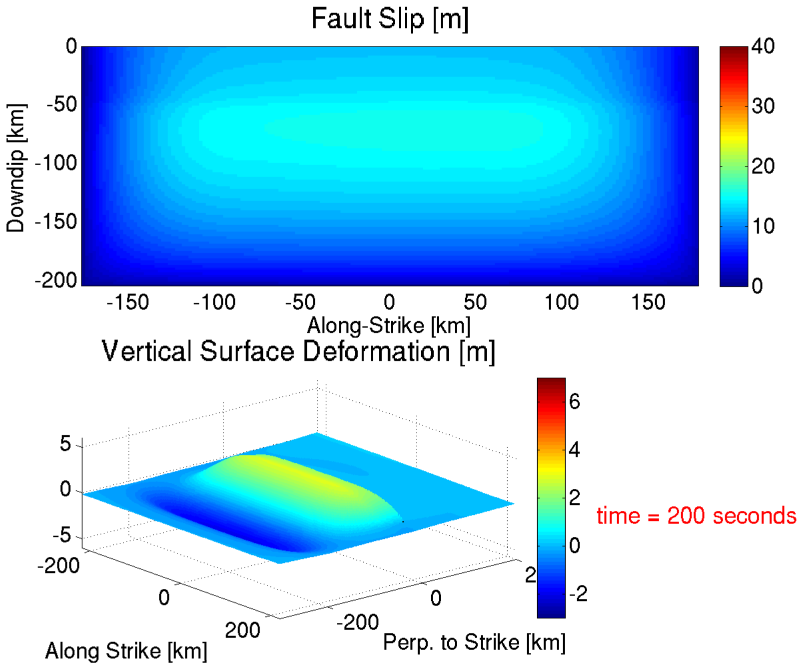

Figure 2.12: Fault slip (top) and total vertical free surface deformation (bottom) for the updip frictional-strengthening zone model. Average fault slip is decreased by 8.2 m (18.6 to 10.4 m) in the strengthening model, relative to the homogeneous model. Surface deformation is decreased broadly along the free surface, relative to the homogeneous model, and the maximum vertical surface displacement is significantly decreased (5.77 to 2.86 m). Note that adding an updip strengthening zone reduces slip across the entire fault – much more so than a western strengthening zone with similar area.

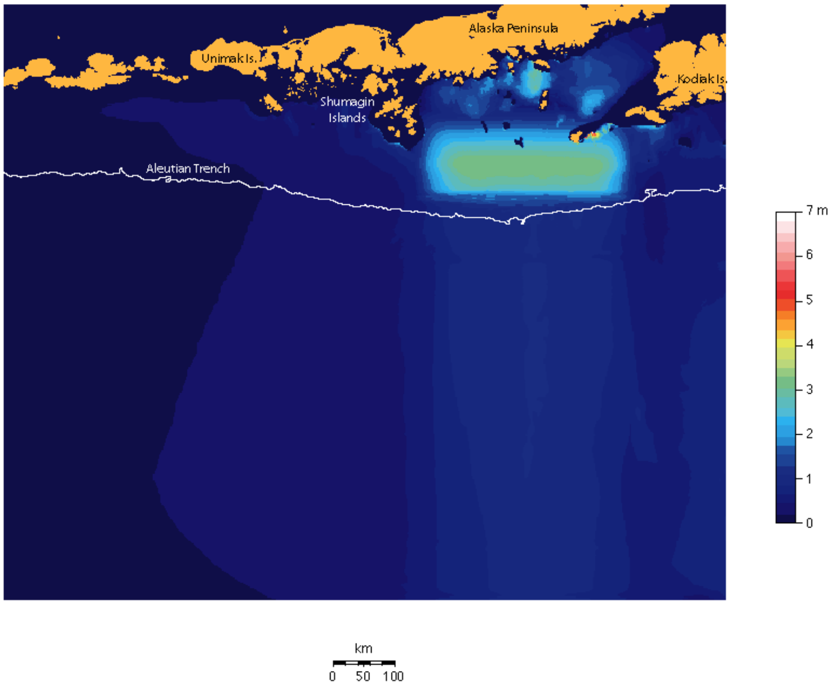

Figure 2.13: Peak tsunami amplitude resulting from the updip frictional-strengthening zone model. Water height corresponds well with free surface deformation (Figure 2.12, bottom). Adding a strengthening zone to the updip portion of the fault greatly reduces tsunami amplitude locally above the strengthening zone as well as broadly above the free surface, relative to the homogeneous model, and reduces the amplitude of the far-field beaming pattern. In addition, peak amplitudes are substantially reduced near the coasts of the Shumagin Islands, the Alaska Peninsula, and Kodiak Island.

2.5.4 Heterogeneous Prestress Rupture

The above models assume homogeneous prestress conditions along the entire extent of the fault. However, observational data imply that earthquakes typically have strongly heterogeneous slip distributions that further imply heterogeneous prestress (e.g., Olsen et al., 1997). Indeed the SAFRR tsunami models use a heterogeneous slip model motivated by the 2011 Tohoku-Oki event, and supported by seismic, geodetic, and geologic data along the Alaskan-Aleutian subduction zone (Kirby et al., 2013). Figure 2.14 shows slip-rate snapshots of rupture propagation for a heterogeneous prestress model designed to qualitatively match the SAFRR dislocation model. As in the case of the homogeneous stress distribution, the fault experiences large slip-rate pulses nearest the free surface. However, due to some high-stress areas down-dip, it also experiences high slip rate in other locations. Additionally, the main slip pulse is spatially heterogeneous; it does not have roughly elliptical symmetry, reflecting a rupture speed that varies across the fault. Note the difference in slip rate between the homogeneous model and heterogeneous prestress model for each snapshot. Rupture proceeds over the entire fault zone for the heterogeneous prestress model. Figure 2.15 shows shear prestress (top) and normal prestress (bottom) distributions. The limiting values are shown in Table 2.2. Figure 2.16 displays the slip distribution used in the SAFRR Tsunami Scenario (Kirby et al., 2013) (top), as well as fault slip (middle) and total vertical free surface deformation (bottom) for the dynamic heterogeneous prestress model. Average fault slip is the same as the homogeneous model (18.6 m), and the maximum vertical surface displacement is increased (5.77 to 7.04 m), relative to the homogeneous model. The heterogeneous prestress leads to a more heterogeneous slip distribution and vertical free surface deformation, compared with the homogeneous model. For comparison, the top panel shows the slip distribution model from the Earthquake Source working group within the SAFRR Tsunami Scenario (Kirby et al., 2013). The slip distribution from the dynamic model (middle panel) and the top panel are qualitatively similar, indicating that the slip distribution used by Kirby et al. (2013) is self-consistent from a physical standpoint: it is possible to obtain such a slip distribution using relatively rigorous physics from a heterogeneous prestress pattern. The total slip distribution is spatially much smoother (Figure

2.16, middle) than our initial stress configurations. We note that tuning initial prestress to get a certain slip distribution is an iterative process, and that further tuning would likely result in a more closely matched slip distribution to the top panel in Figure 2.16, but with gradually diminishing returns. Figure 2.17 shows local peak tsunami amplitudes resulting from the heterogeneous prestress model. Water height corresponds well with vertical free surface deformation, showing peak tsunami amplitudes above regions of the fault nearest the trench with maximum slip. Although the peak amplitudes immediately above the hanging wall are spatially more varied than the homogeneous model, the overall beaming patterns and maximum amplitudes along the local coasts are similar.

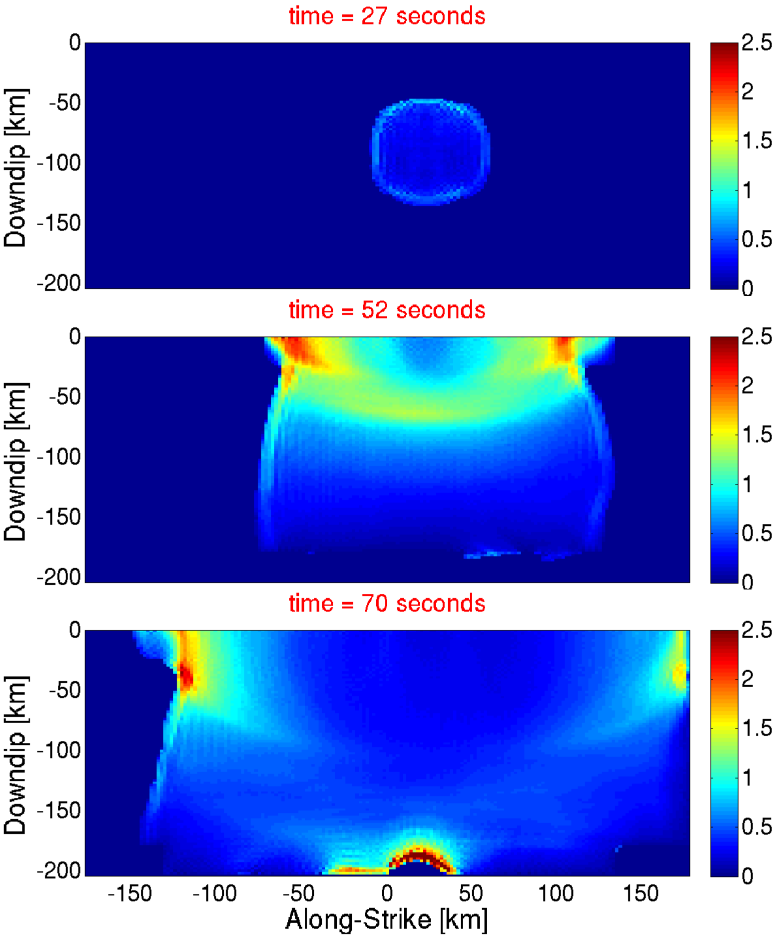

Figure 2.14: Snapshots of slip rate (i.e., rupture propagation) in $\frac{m}{s}$ for a heterogeneous prestress model. The fault experiences large slip rate pulses nearest the free surface, and for some areas downdip (in contrast to the homogeneous model). Note the difference in slip rate between the homogeneous model and heterogeneous prestress model for each snapshot. Rupture proceeds over the entire fault zone.

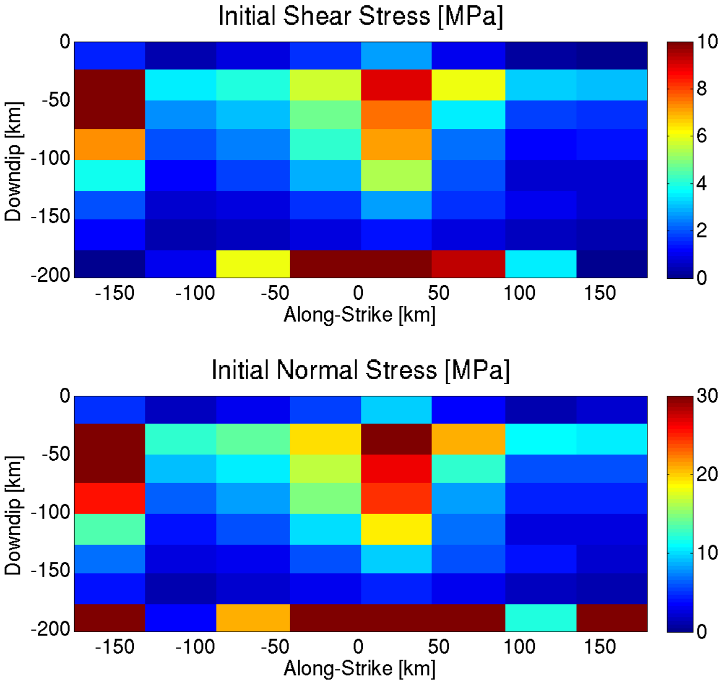

Figure 2.15: Initial shear stress (top) and normal stress (bottom) for the heterogeneous prestress model. The limiting values of stress are shown in Table 2.2. The total slip distribution is spatially much smoother (Figure 2.16, middle) than our initial stress configuration.

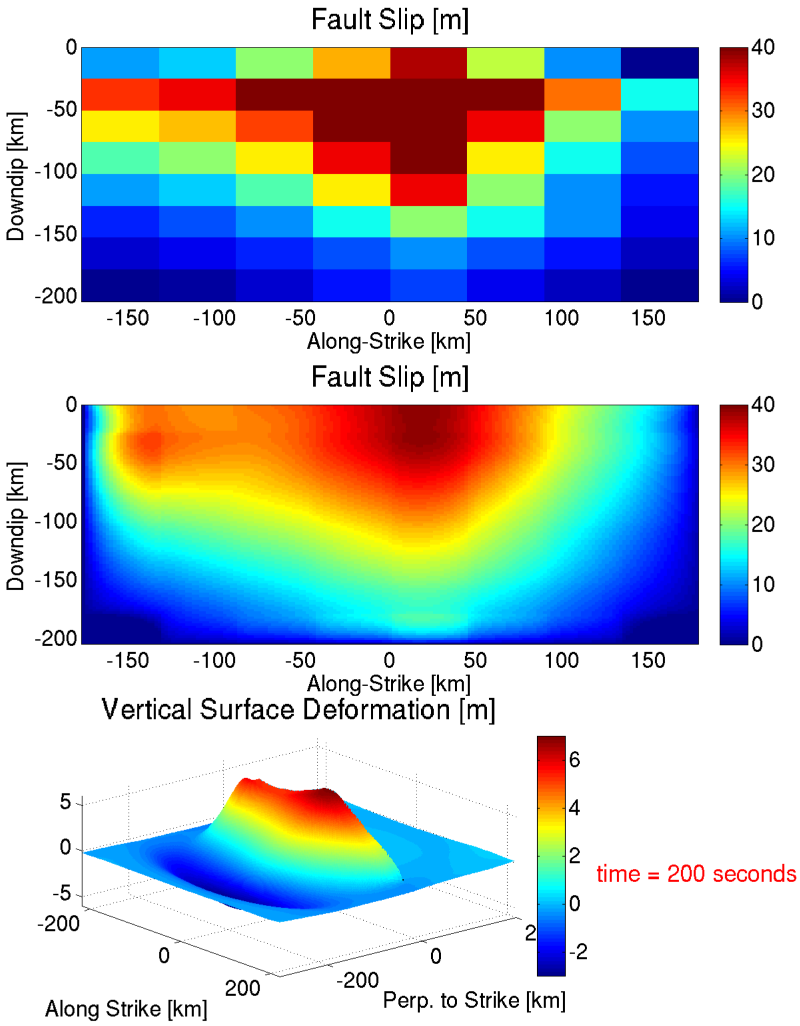

Figure 2.16: The slip distribution used in the SAFRR Tsunami Scenario (top). Fault slip (top) and total vertical free surface deformation (bottom) for the dynamic heterogeneous prestress model. Average fault slip is the same as the homogeneous model (18.6 m), and the maximum vertical surface displacement is increased (5.77 to 7.04 m) relative to the homogeneous model. The heterogeneous prestress leads to a more heterogeneous slip distribution and vertical free surface deformation, compared with the homogeneous model. The dynamic slip distribution (middle panel) qualitatively resembles the top panel.

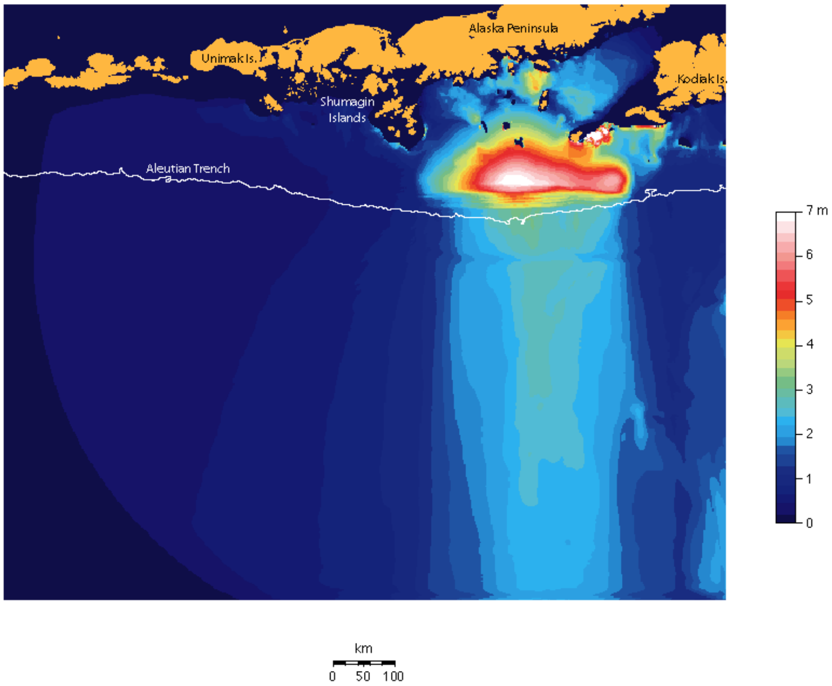

Figure 2.17: Peak tsunami amplitudes resulting from the heterogeneous prestress model. Although the peak amplitudes immediately above the hanging wall are spatially more variable than the homogeneous model, the overall beaming patterns and amplitudes along the local coasts are similar.

2.6 Discussion

The four earthquake rupture models in this study generate four different tsunami models along a portion of the Alaskan-Aleutian subduction zone. How a tsunami is locally generated in this region affects inundation and runup on local coasts (i.e., Alaska Peninsula) and could affect propagation across the Pacific Ocean onto coastlines along the Pacific Rim. For the homogeneous model, there are large slip pulses near the free surface (Figure 2.5) that result from the dynamic unclamping of the fault and the geometric asymmetry of the hanging wall/footwall. In turn, this effect results in large slip near the free surface, and therefore large vertical free surface deformation near the trench (Figure 2.6). The consequent modeled tsunami most significantly propagates northward/southward into/from the Alaska Peninsula (Figure 2.7). A completely homogeneous pre-stress and frictional parameter earthquake rupture model that produces the largest slip near the trench has important implications for the resulting tsunami, since sea floor displacement is most sensitive to fault slip near the trench (Okada, 1985). Large amplitude tsunamis can be generated by slip distributions localized near the trench.

Including a frictional-strengthening segment (emulating rate-strengthening behavior) along the Shumagin sector in the model significantly affects the slip distribution and initial tsunami wave field. The rupture propagates through the entire strengthening zone, but with greatly reduced slip rate, and this effect reduces the overall average slip on the fault commensurately (Figures 2.8 and 2.9). The surface deformation is consequently scaled downward in this zone of lower slip. Importantly, the beaming pattern of the far-field tsunami is shifted for the western strengthening rupture, relative to the homogeneous rupture (Figure 2.10). Therefore, far-field tsunami propagation can shift, potentially changing inundation and runup on coastlines along the Pacific Rim. It is interesting to note that the computationally simulated rupture can penetrate a strengthening zone that is as large as 80 km wide along-strike. The dynamic reduction of normal stress due to the dip-slip geometry may facilitate this rupture propagation near the free surface. In other words, in our models time-dependent normal stress induced by the free surface may allow thrust rupture to more easily penetrate a rate-strengthening region near the surface. This result raises the prospect that rupture might be able to propagate through such a zone into another frictional weakening zone in future earthquakes, generating a larger earthquake and tsunami.

Including a frictional-strengthening segment updip near the trench also significantly affects the slip distribution and initial tsunami wave field (Figures 2.11 through 2.13). Adding a strengthening zone updip more significantly affects average fault slip than a strengthening zone along strike. Without a frictional-strengthening zone updip (e.g., the homogeneous model), rupture propagates energetically updip, sending radiation to the entire fault, promoting slip. Because it prevents the strong seismic radiation from the most updip section of a thrust fault during rupture, there are broad effects on slip and slip rate for the rest of the fault from a frictional-strengthening zone updip. As a result, we see a broad decrease in maximum tsunami amplitude, but with a similar beaming pattern when compared to the homogeneous rupture. Slip distributions near the trench are known to be important for tsunami generation (Geist, 1998; Geist and Dmowska, 1999; Geist and Bilek, 2001; Geist, 2002). Our results show slowed rupture propagation in frictional-strengthening zones with a lower peak slip rate, but these zones still have significant slip in those regions. This result hints at a possible mechanism for tsunami earthquakes (Kanamori, 1972).

We note that adding a frictional-strengthening zone along strike or updip does not preclude the ruptures from having static stress drops. Static stress drop depends on the rupture dynamics. It is possible to obtain a stress drop in a frictional-strengthening zone due to a large free-surface-induced reduction in normal stress (Ryan, 2012; Kozdon and Dunham, 2013), since the sliding frictional resistance is equal to the friction coefficient multiplied by the normal stress.

A heterogeneous prestress model significantly affects the slip distribution and initial tsunami wave field, with the largest peak tsunami amplitudes above portions of the fault with the largest slip (Figure 2.16). Although average slip is the same between the homogeneous rupture and the heterogeneous prestress rupture, the latter has a larger maximum vertical free surface displacement because slip is more localized. Nonetheless, the beaming pattern of the far-field tsunami is similar for both models (Figures 2.7 and 2.17). We match the seismic moment in the heterogeneous prestress model to the source model used by Kirby et al. (2013) through a trial and error process. We also qualitatively match the slip distribution of the dynamic model to the source model (Figure 2.16). The total slip distribution is spatially much smoother than the initial stress configurations (Figures 2.15 and 2.16), in agreement with previous studies (Olsen et al., 1997; Olsen et al., 2009). Considering all four rupture models in this study as well as previously studied and observed megathrust events in other parts of the world (e.g., Ammon et al., 2011), the SAFRR Tsunami Scenario dislocation model appears to be self-consistent as a tsunami source, even when modeled as a complex rupture that involves frictional-strengthening updip and/or along strike as well as a heterogeneous prestress. Adding more precise source parameters in 3-D (e.g., complex fault geometry, material properties, and stochastic stress fields) would further this study and help produce more realistic modeled seafloor deformation.

We use a simple planar fault geometry in this study; however, previous work by Oglesby and Archuleta (2003) suggests that fault slip and low-frequency ground motion are relatively unchanged for a nonplanar thrust fault with an abrupt change in dip when compared to a planar fault with an equivalent dip near the free surface. This result suggests that the shallow dipping rupture process is most important in producing ground motion. Combined with the strong dependence of tsunami generation on slip near the trench (an area that generally has the shallowest dip for a subduction zone), we feel comfortable (at least to first order) using a planar fault with a small dip in this study to study effects on local tsunami generation. However, to better model the dynamics of the rupture process as well as the resultant tsunami, more accurate fault geometry should be used in future modeling efforts.

Using dynamic earthquake rupture models coupled, in time, with hydrodynamic models can be a very useful tool. We show that rupture dynamics on a megathrust can play an important role in tsunami generation and local propagation. It is true that tsunami formation is relatively insensitive to the temporal evolution of rupture. In other words, taking the final seafloor deformation as an initial condition for tsunami generation would produce a tsunami not tremendously different from one produced by the time-dependent seafloor deformation. However, this does not mean that the tsunami generation is insensitive to the spatiotemporal details of the rupture process. Indeed, the rupture path and overall slip distribution (which are first-order determinants of the tsunami) crucially depend on dynamic stress interactions (e.g., Harris and Day, 1993), and thus on these spatiotemporal effects. For thrust faults in particular, it very instructive to analyze results from dynamic models, since time-dependent normal stress fluctuations that arise from the free surface affect slip rates and slip distribution. Additionally, rupture propagation through stable-sliding zones can be accurately modeled dynamically, and therefore may be used in future endeavors to simulate tsunami earthquakes.

Chapter 3

Dynamic Models of an Earthquake and Tsunami Offshore Ventura, California

3.1 Abstract

The Ventura basin in southern California includes coastal dip-slip faults that can likely produce earthquakes of magnitude 7 or greater, and significant local tsunamis (Rockwell, 2011; Hubbard et al., 2014). We construct a 3-D dynamic rupture model of an earthquake on the Pitas Point and Lower Red Mountain faults to model low-frequency ground motion and the resulting tsunami, with a goal of elucidating the seismic and tsunami hazard in this area. Our model results in an average stress drop of 6 MPa, an average fault slip of 7.4 m, and a M_w of 7.7, consistent with regional paleoseismic data (Rock-

well, 2011). Our corresponding tsunami model uses final seafloor displacement from the rupture model as initial conditions to compute local propagation and inundation, resulting in large peak tsunami amplitudes northward and eastward due to site and path effects. Modeled inundation in the Ventura area is significantly greater than that indicated by state of California's current reference inundation line (`http://www.conservation.ca.gov/cgs/geologic_hazards/tsunami/inundation_maps/`).

3.2 Introduction

Earthquakes are among the chief sources of tsunamis – long ocean waves sustained by gravity that increase in amplitude as water depth decreases. Therefore, such waves are particularly hazardous along populated coastlines near offshore faults that produce vertical displacement of the seafloor and water column. Although the hazard from earthquake-generated tsunamis offshore southern California has received relatively little attention, there have been reports of several significant local tsunamis in the past 200 years (Townley and Allen, 1939; Ulrich, 1942; Lander et al., 1993; Borrero et al., 2001). Lander et al. (1993) explain that both locally generated tsunamis (e.g., tsunamis generated from the 1812 and 1854 Santa Barbara earthquakes and possible submarine landslides) as well as far-field generated tsunamis (e.g., the tsunami generated from the 1946 Aleutian earthquake) have impacted the California coast. In particular, the 1812 Santa Barbara earthquake (that likely occurred in the Santa Barbara Channel), estimated to have a local magnitude (M_L) of 7 (e.g., Hamilton et al., 1969), created a tsunami throughout the region that was reported as a "huge" sea wave (Townley and Allen, 1939), while the earthquake ground motion significantly damaged Mission San Buenaventura in Ventura (Townley and Allen, 1939).

Due to propagation speeds of 700 $\frac{km}{hour}$, tsunamis generated by distant sources allow for early coastal warning on the order of hours. However, tsunamis generated locally by faulting and landslides offshore California can impact the California coastline in a matter of minutes, making it imperative to understand the likelihood of such events. Ross et al. (2004) examined seismic and secondary hazards (e.g., tsunamis and liquefaction) along the coast of Ventura County, California, suggesting that the area is at risk of damaging tsunamis from both the far field (e.g., offshore Alaska) and the near field (e.g., Santa Barbara Channel). Wilson et al. (2014) conducted a California statewide survey to examine possible evidence from tsunami impacts along the coastline, including 20 coastal marshlands. Potential tsunami deposits were assessed at the Carpinteria Salt Marsh Reserve in Santa Barbara County. In particular, at this location they found sand layers consistent with tsunami deposition. However, observed microfossils in those same sand layers did not have a marine origin. Therefore, current evidence of prehistoric tsunamis impacting the Carpinteria Salt Marsh Reserve is somewhat ambiguous.

The ground motion from submarine earthquakes can generate tsunamis, and studies have shown that the ground motion distribution depends quite strongly on the geometric pattern of ruptured faults (e.g., Nason, 1973; McGarr, 1984; Cocco and Rovelli, 1989; Abrahamson and Somerville, 1996; Oglesby et al., 1998). Therefore, fault geometry can have first-order effects on tsunami generation (Wendt et al., 2009). The distribution of slip on a fault can have important effects on the generated tsunami as well (Geist, 1998, Geist and Dmowska, 1999; Geist 2002). Unfortunately, the rupture path and slip pattern of an earthquake on a complex fault system are not easy to estimate a priori. Dynamic earthquake rupture models are a useful way of providing realistic earthquake scenarios on geometrically complex faults; such models are physics-based and do not assume a fault slip distribution or ground motion a priori; rather, slip distribution and ground motion are calculated results of the models based on estimates of fault stress, geometry, and material properties. The use of such methods in tsunami modeling is quite new; very few studies (e.g., Wendt et al., 2009) have used dynamic rupture modeling to estimate tsunami generation from geometrically complex faults. Furthermore, there have been few tsunami modeling studies offshore Ventura, California (see Figure 3.1). Borrero et al. (2001) perform hydrodynamic

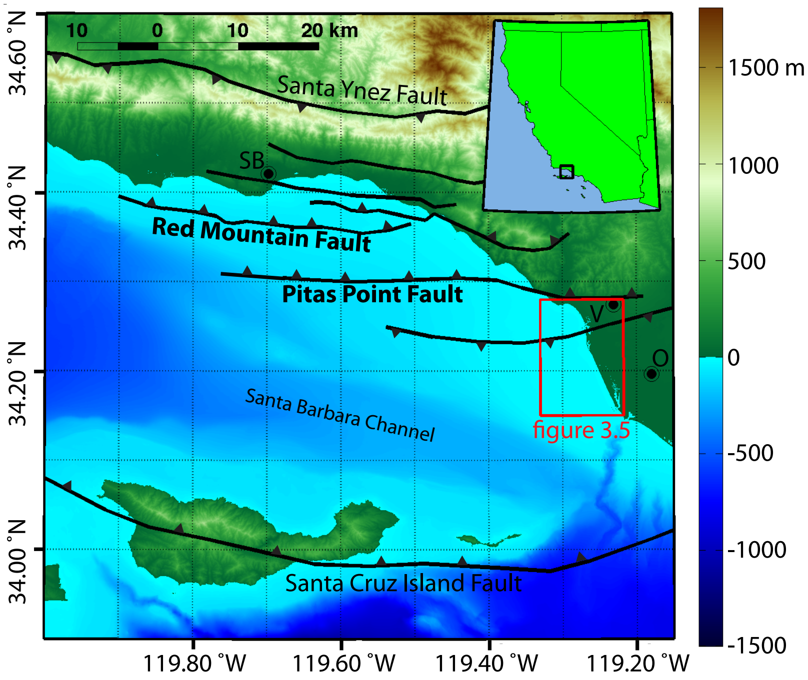

Figure 3.1: Topographic/bathymetric map of onshore/offshore southern California, with height and depth in meters. The Red Mountain and Pitas Point faults are considered in this study. Triangles indicate direction of dip; faults without triangles are considered strike-slip. Letters show approximate (central) city locations: SB = Santa Barbara; V = Ventura; O = Oxnard. The rectangle outlined in red contains the geographic region for Figure 3.5. Inset shows the map boundary in black.

analysis from a locally generated tsunami offshore southern California on the Channel Islands Thrust system, a north-dipping fault that is located approximately 50 km south of Santa Barbara. Assuming a homogeneous slip distribution on a planar fault, they find regional tsunamis with about 2 m of runup from a moment magnitude (M_w) 7.3 earthquake source, and up to 15 m of local runup from submarine landslides that could be triggered from nearby earthquakes. However, they do not incorporate any geometrical complexity or spatially-heterogeneous slip in their earthquake models, nor do they investigate potential tsunamis from other offshore reverse faults in the region, including the Red Mountain and Pitas Point faults, which are closer to some populated regions. The Pitas Point and Red Mountain faults are north-dipping and generally trend east-west (e.g., Fisher et al., 2009). Hubbard et al. (2014) used several available datasets, including industry seismic profiles as well as their own seismic profiles to improve the subsurface fault model for this fault system. The model presented by Hubbard et al. (2014) suggests a complex, segmented fault system that extends to seismogenic depth (roughly 20 km). Rockwell (2011) used aerial photography to identify marine terraces in the Ventura region along the coast of southern California, suggesting discrete movements in the past with 5-10 m of uplift, with the last event occurring approximately 800 years ago. Therefore, a proper tsunami hazard analysis should incorporate modeled earthquakes that produce deformation consistent with such events.

3.3 Dynamic Rupture on the Pitas Point and Lower Red Mountain Faults

We use a 3-D finite element method (FEM) (Barall, 2009) to model earthquake rupture on a connected, nonplanar Pitas Point and Lower Red Mountain fault geometry (see Figures 3.1 and 3.2) with spatially constant initial traction and a homogeneous linear elastic Earth structure. The output consists of the rupture pattern on the fault as well as the full seismic wave field and surface deformation. A key input is the fault system geometry. Plesch et al. (2007) developed a new 3-D community fault model for southern California that consists of major fault systems defined by geologic and seismic evidence (e.g., surface traces and seismicity). Hubbard et al. (2014) further improved upon fault geometries both on and offshore Ventura County by utilizing additional datasets, including seismic reflection profiles and drill-hole data. Therefore, we use a fault system geometry consistent with Hubbard et al. (2014) to dynamically model earthquake rupture on the Pitas Point and Lower Red Mountain faults offshore Ventura. In particular, we utilize a fault geometry that connects the Pitas Point fault at depth to the deeper Lower Red Mountain fault via a more horizontal section of fault (see Figure 3.2). We employ a relatively curved fault geometry (e.g., the transition from the Lower Red Mountain fault to the Pitas Point fault is curved) that can result in a relatively smoother rupture transition along dip and slightly smoother ground deformation when compared to the kinked fault geometry in Hubbard et al. (2014) with analogous fault rupture. The resultant tsunami is not likely to be sensitive to these small spatial and temporal wavelength features. The utilized material properties (e.g.,

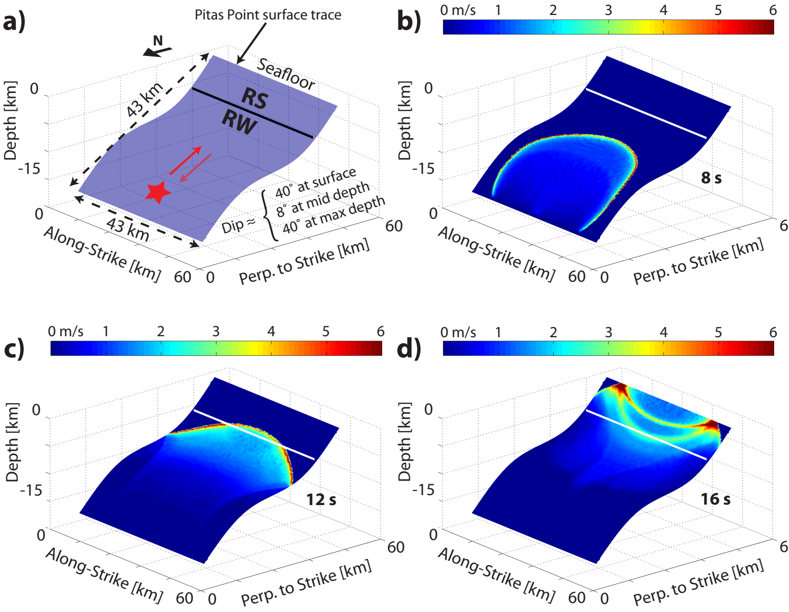

Figure 3.2: Fault geometry and slip rate snapshots. Panel A shows the fault geometry of the connected Pitas Point and Lower Red Mountain faults with the rate-strengthening (RS)/rate-weakening (RW) boundary indicated by the solid black line (see methods section), the nucleation zone indicated by the red star, and the approximate direction of fault slip indicated by the red arrows (i.e., reverse fault motion). Note that the Pitas Point fault intersects the seafloor and that fault dip is northward. Panels B through D show dip-slip rate snapshots in m/s at 8 s, 12 s, and 16 s after earthquake nucleation, respectively. Solid white line indicates the RS/RW boundary.

Christensen and Mooney, 1995), prestress regime, and computational parameters (Table 3.1) are quite generic, and are not tuned to produce a worst-case earthquake. FaultMod is validated in rupture benchmarks published by the Southern California Earthquake Center and the US Geological Survey (Barall, 2009; Harris et al., 2009). The code incorporates artificial viscous damping (Dalguer and Day, 2007) as well as algorithmic damping to help damp spurious oscillations, and energy-absorbing boundary conditions along the mesh edges to avoid artificial seismic wave reflections from the model boundaries. Friction is a crucial part of earthquake processes. We use an empirically based rate- and state-dependent friction law (Dieterich, 1978; 1979; Ruina, 1983) that is controlled by physical parameters such as

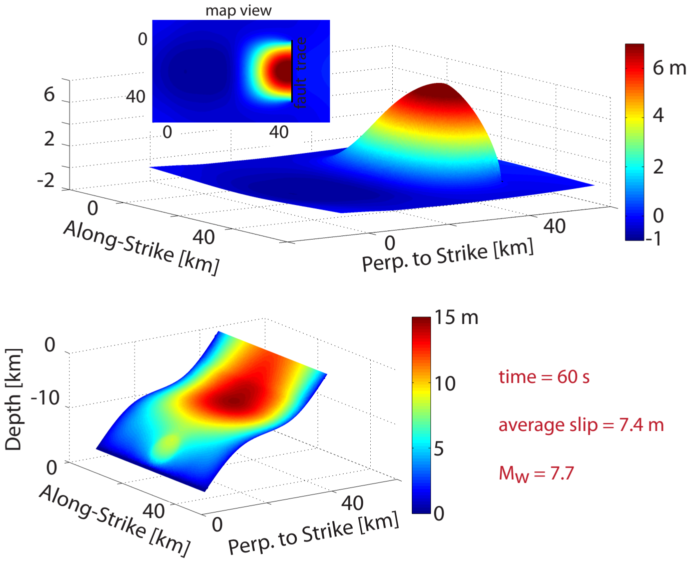

Figure 3.3: Vertical free surface deformation and total slip. Top: Vertical surface (i.e., seafloor) deformation resulting from slip on the fault system, with a maximum vertical displacement of over $+7$ m. The map view inset shows the same vertical deformation and indicates the fault trace by a solid black line. Bottom: Amplitude of slip on the fault system, with an average of 7.4 m. Note that the final deformation and slip are shown at 60 s after nucleation. The M_w for the earthquake is 7.7.

slip rate and time evolution of contact surfaces. Following the work of Lapusta et al. (2000) and Harris et al. (2009), we employ a modified version of the rate-state ageing law that is computationally stable at very small slip rates (Ryan and Oglesby, 2014), with the bulk of the fault having rate-weakening (unstable) friction, and the top most 5 km of the fault having rate-strengthening (stable sliding) properties (see Figure 3.2).

The depth extent of the modeled rate-strengthening zone is consistent with inferred stable sliding zones at subduction zones and crustal faults (e.g., Scholz, 1998). We note that an analogous model without the rate-strengthening zone (i.e., completely rate-weakening) has twice the average slip and twice the maximum vertical seafloor displacement, approximately, when compared to the model that incorporates the rate-strengthening zone.

Rupture nucleation (see red star in Figure 3.2 panel a) is achieved by increasing the shear stress over an expanding front in time; following nucleation, rupture propagates along the rest of the fault spontaneously. The dynamic rupture code treats the seafloor as a traction-free surface and does not model the water movement (i.e., compressional waves through the water column are not modeled). The rupture model produces final seafloor displacement, which is then used as input for the tsunami modeling code.

The Cornell Multi-grid Coupled Tsunami (COMCOT) Model (Liu et al., 1995; Wang and Liu, 2006) solves the discretized, nonlinear shallow-water wave equations, using an explicit leap-frog finite-difference algorithm. The nonlinear convection term in the momentum equation is discretized using an upwind scheme. Attenuation from shear stress along the sea floor is included using Manning's formulation, where a constant Manning's coefficient of 0.013 is used. Runup and inundation over initially dry cells are also included through the implementation of moving boundary conditions. The merged bathymetric and topographic digital elevation models (DEMs) used for the tsunami model are from 1 and 3 arc-second resolution Southern California Coastal Relief Model version 2 from the National Geophysical Data Center. The reference elevation for both DEMs is mean sea level (MSL). A mean high water (MHW) vertical datum is used for the calculations by adjusting the DEMs according to the MHW-MSL difference listed at the Santa Barbara tide gauge station. The duration of the simulation is 160 $min.$, sufficient for the maximum amplitude to be recorded in the model domain. Because the phase speed of tsunami waves is much slower than the velocity of the rupture front, particularly in the shallow ocean above the Pitas Point fault, the time-varying effects of tsunami generation are small (cf. Geist et al., 2007). Therefore, the instantaneous initial condition for tsunami generation is thought to be an adequate approximation.

The dynamic rupture model using the parameters listed in Table 3.1 results in a M_w 7.7 earthquake scenario on the Pitas Point and Lower Red Mountain faults. The fault geometry causes strong perturbations in slip rate that result from dynamic normal-stress perturbations as rupture travels updip (e.g., Oglesby et al., 1998), with an average final slip of 7.4 m and an average static stress drop of approximately 6 MPa. Figure 3.2 shows the fault geometry and dip-slip rate snapshots at 8 s, 12 s, and 16 s. As rupture propagates updip, slip rate fluctuates owing to changes in fault geometry and consequent changes in dynamic normal stress. As rupture propagates through the first main bend, slip on the basal segment results in reduced normal stress (unclamping) on the connecting (nearly horizontal) section, which in turn results in increased slip rate on that connecting segment. As the rupture rounds the second fault bend the steeper updip section of fault is dynamically clamped, inhibiting fault slip; however, the rupture is strong enough to continue updip. At 12 s, the rupture is propagating into the rate-strengthening (stable) zone, resulting in reduced slip rate. Rupture extends to the free surface, with a breakout shown at 16 s. A breakout phase occurs when the rupture penetrates or “breaks out of” the free surface (i.e., seafloor) (e.g., Oglesby et al., 1998). At and around 16 s, there is a reduction in normal stress that corresponds to the breakout phase with an accompanying increase in slip rate.

Figure 3.3 shows vertical surface (i.e., seafloor) displacement and total slip resulting from the earthquake model. The largest vertical displacement, over 7 m, occurs on the

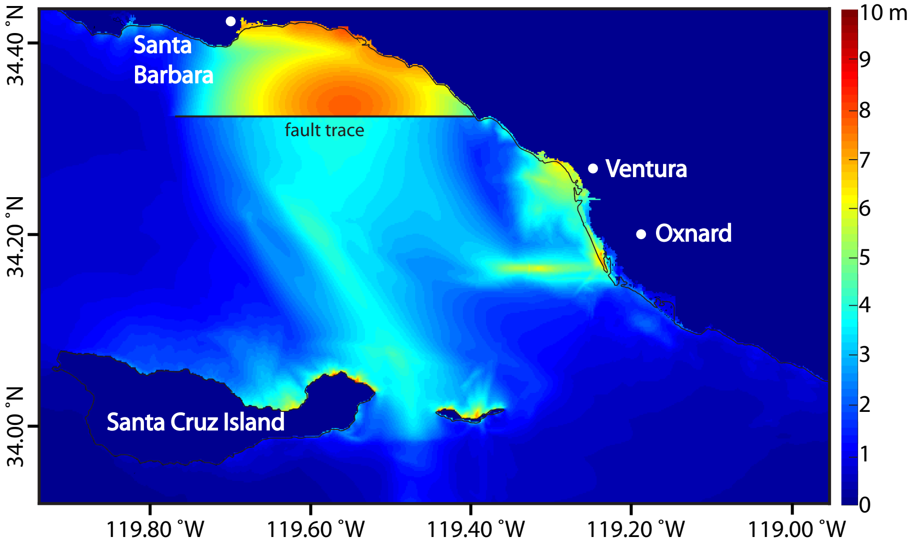

Figure 3.4: Map of regional peak tsunami amplitude in meters resulting from an earthquake on the Pitas Point and Lower Red Mountain fault system. The thin solid black line indicates the coastline and the thick black line indicates the fault trace. Note that significant regional tsunami inundation occurs.

hanging wall (north) side of the fault, consistent with observations of the Ventura fault – the onshore fault that is likely connected to the Pitas Point fault (e.g., Rockwell, 2011; Hubbard et al., 2014). The largest slip on the fault occurs updip from the nucleation zone ($> -12\ km$ depth), with somewhat reduced slip on the most updip section due to rate-strengthening friction. These results indicate that unclamping of normal stress induced by the updip-propagating rupture allows rupture to penetrate a rate-strengthening region near the surface (Ryan, 2012; Kozdon and Dunham, 2013). Additionally, the curved fault geometry and constant traction result in an energetic rupture that produces significant slip within the surficial rate-strengthening zone, similar to that inferred in the 2011 Tohoku, Japan Earthquake (Yamazaki et al., 2011).

3.4 Local Tsunami Propagation and Inundation

The tsunami resulting from our modeled rupture on the Pitas Point and Lower Red Mountain faults was modeled using COMCOT. Table 3.2 indicates the hydrodynamic model parameters. The vertical displacement field calculated by the dynamic rupture models at 60 s provides the instantaneous initial condition for the tsunami model. Almost all of the fault slip occurs within the first 20 s of the model; the vertical displacement field at 60 s is the static configuration of the seafloor. The vertical seafloor displacement from the earthquake scenario produces a strong local tsunami wave train. Coastal areas with the largest local amplitude are northward (i.e., Santa Barbara) and eastward (i.e., Ventura and Oxnard) of the surface rupture (see Figure 3.4). Large amplitudes northward result from the direct propagation of the northward-directed tsunami toward decreasing water depth as the tsunami approaches the coastline. The more unexpected large amplitudes to the east result from two main effects: strong eastward refraction of the southward-directed tsunami wave train as the waves encounter deeper water to the south in the Santa Barbara Channel (Figure 3.1), and focusing of the waves guided by bathymetry (e.g., intersection of slower near-shore waves with faster deep-water waves in the channel). Figure 3.5 shows localized peak tsunami amplitude around Ventura and Oxnard, CA. Figure 3.1 outlines the area in Figure 3.5 in red. The solid black line indicates the coastline, and the solid red line is the statewide tsunami inundation border used by the California Emergency Management Agency (`http://www.conservation.ca.gov/cgs/geologic_hazards/tsunami/inundation_maps/`). Letters indicate key geographic locations, including Santa Barbara, Ventura Harbor, the Santa Clara River Mouth, McGrath State Beach, and the Channel

Islands Harbor Entrance. Our modeled tsunami inundation exceeds the state estimate in multiple locations. For comparison, Figure A.1 in the appendix shows orthographic imagery of coastline indicated in Figure 3.5, with modeling results removed. Supplementary movie 1 shows how tsunami propagation from variations in the regional bathymetry leads to strong northward and eastward beaming effects. Note that inundation is not shown in the movie; the supplementary movie is intended to show only propagation properties of the modeled tsunami. At less than 1 *min.*, the surface break is apparent, with the tsunami splitting into 2 main waves propagating north and south. At approximately 9 *min.* there are strong reflections of the northward wave off the northward shore, and refraction (i.e., rotation counter clockwise) of the southward beaming tsunami due to water depth changes. Focusing occurs to the east (toward Ventura and Oxnard), shown at about 17 *min.*, due to this refraction and reflection off local shorelines.

This study describes one potential earthquake and tsunami scenario along the Pitas Point and Lower Red Mountain faults, but it is not intended to give an overall distribution of all possible earthquake and tsunami hazards in this region. The size of future earthquakes, their slip patterns, and thus their seafloor displacement are largely unknown a priori. It is therefore extremely helpful to combine dynamic earthquake models, which provide physically plausible earthquake scenarios in which the slip is a calculated result of the model, with tsunami models to study effects from tsunami generation and propagation; such models can help to fill in gaps in the historic and prehistoric record of earthquakes and tsunamis. Additionally, it is possible that a potential earthquake rupture on the Pitas Point fault would not penetrate the seafloor. Therefore, we provide one alternative model

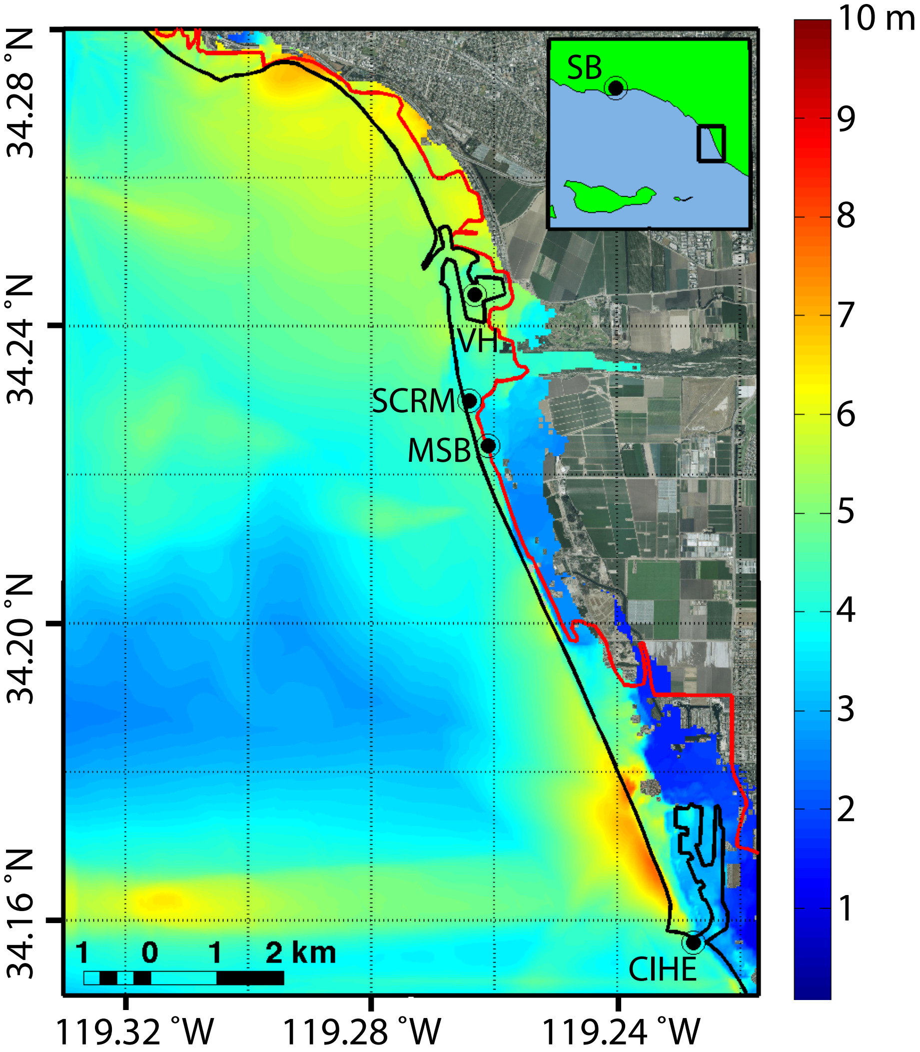

Figure 3.5: Map (red box shown in Figure 3.1) of localized peak tsunami amplitude, in *m* (around Ventura, CA), resulting from slip on the Pitas Point and Lower Red Mountain fault system. The solid black line indicates the coastline. The sold red line is the statewide tsunami inundation map coordinated by the California Emergency Management Agency. Letters indicate example locations (approximate): SB = Santa Barbara; VH = Ventura Harbor; SCRM = Santa Clara River Mouth; MSB = McGrath State Beach; CIHE = Channel Islands Harbor Entrance. Inset shows the map boundary in black. Note that inundation from the model is significantly greater in many places than the statewide estimate.

set that is the same configuration as previously discussed with the exception that the fault terminates 1 *km* below the seafloor. The appendix shows figures for fault slip (Figure A.2), vertical seafloor deformation (Figure A.2), maximum regional tsunami amplitude (Figure

A.3), and localized maximum tsunami amplitude for the Ventura/Oxnard region (Figure A.4). In that case, significant local inundation still occurs, albeit on a somewhat lower level.

3.5 Implications for Tsunami Hazard Offshore Southern California

Generally, tsunamis can show complex wave effects, including reflection and refraction due to changes in topography/bathymetry along shorelines. Such wave properties have implications for tsunamis propagating along the southern California coastline. Results from the models in this study indicate that the coastal areas of Santa Barbara, Ventura, and Oxnard are particularly vulnerable to earthquake and tsunami hazard from rupture on the Pitas Point and Lower Red Mountain faults. Our modeled inundation exceeds, in most places, the state estimate of inundation in Ventura and Oxnard, owing to a combination of the seafloor displacement from our scenario earthquake, refraction, focusing, and flat topography that facilitates water flowing inland. Therefore, the tsunami hazard in Ventura and Oxnard may be higher than has been previously inferred. Additionally, we note that our earthquake model is not a worst-case scenario, since we use 1) a stress parameterization that is not an outlier in terms of overall stress drop when compared to calculated stress drops in the southern California area (Hauksson, 2014), and 2) a somewhat conservative estimate for the spatial extent of the Pitas Point Fault (which may in fact connect to the Ventura fault on shore). However, it is worth noting that the hypothetical earthquake scenario in this study would be among the top three or four largest magnitude earthquakes ever recorded in California, dating back to the mid eighteenth century (`http://earthquake.usgs.gov/earthquakes/eqarchives/`). The probability of such an event in a given time frame is low compared to smaller earthquake events. Nonetheless, it is crucial to investigate the possible effects from such rare but plausible earthquake and tsunami scenarios so that a full hazard assessment can be made. While the details of an actual future event are likely to be more complex, our model likely captures many important aspects for the purposes of tsunami generation. Results from these modeling efforts can help reveal potential regions of high tsunami hazard. Additionally, further development of this methodology in tsunamigenic regions worldwide can contribute to hazard assessments.

We acknowledge some limitations in this study so that future studies can expand on the current results. The marine terraces along the coast could be the result of localized rupture effects since the uplift measurements are taken over a limited area (Hubbard et al., 2014). Additionally, multi-fault ruptures including, for example, the Ventura, Pitas Point, Red Mountain, and San Cayetano faults along the Ventura coast could produce the large amount of average slip needed to produce the terraces. The historical record for ruptures on the faults within this study is not well characterized; however, the available data suggest the possibility of large earthquakes with long recurrence intervals in this area, including multi-segment ruptures producing earthquakes up to M_w 7.8 (Hubbard et al., 2014). Therefore, it will be important to model several different rupture scenarios on such fault systems, since the complete earthquake history of these faults is unknown. More comprehensive trenching onshore, sediment coring offshore, and sediment analysis onshore (i.e., sand grain analysis) to determine the occurrence of earthquakes and tsunami in this region is an area of active research (Wilson et al., 2014). Other regional reverse faults certainly have the capability of tsunamigenesis. The Santa Cruz Island and Anacapa-Dume faults, the largest known offshore fault zone near Ventura, CA, is roughly 30 *km* to the south of the Pitas Point fault, and is thought to be capable of generating large earthquakes with M_w greater than 7 (e.g., Pinter et al., 1998; Ross et al., 2004). Incorporating the upper Red Mountain fault, which branches off near the intersection of the lower Red Mountain and Pitas Point faults, could strongly affect local tsunami properties in this area (Fisher et al., 2005). Finally, the current study assumes constant traction across the fault. However, we note that smaller magnitude stress regimes near the free surface would decrease the amount of energy available for seismic wave radiation and therefore would decrease, relative to the current model, fault slip near the free surface. Incorporating spatially varying initial stress distributions on the faults may provide valuable insight into a broader range of scenario ruptures. Earthquake size, rupture propagation, and slip distribution are directly dependent on nucleation location and stress regime (e.g., Oglesby et al., 2008). In addition, including elastic properties and plausible stress distributions from Global Positioning System (GPS) models (e.g., Marshall et al., 2013) may help provide robust, interdisciplinary earthquake and tsunami scenarios. We also note that submarine landslides can generate large tsunamis in and near the Santa Barbara Channel, and some landslides are documented in this region (Ross et al., 2004; Fisher et al., 2005). In fact, modeling of the “Goleta Slide” indicates that a tsunami with local wave heights between 2 and 20 *m* could have been generated (Borrero et al., 2001). Our simple model is not complete enough to provide a true quantitative measure of tsunami hazard or the precise spatial extent of the inundation zone in the Ventura and Oxnard region; such a calculation would require the contribution of multiple faulting and landslide scenarios from a variety of near- and far-field sources. However, the current model gives an indication of what may be possible in this region, and points toward future work to ameliorate the effects of tsunamis here and elsewhere around the globe.

Table 3.1: Stress values, material properties, model properties, and friction parameters used for the earthquake model.

τ_o (initial shear stress)	49.14 MPa
σ_o (initial normal stress)	78.64 MPa
τ_o (initial shear stress in nucleation zone)	65.80 MPa
Density	2700 kg/m^3
S-wave speed	3162 m/s
P-wave speed	5477 m/s
Nucleation Radius	4000 m
Nucleation Speed	2000 m/s
Fault element Size	~200 m
Off-fault element size (~2 km away from fault)	~600 m
Rupture time step	1.000e-2 s
ψ_{ini} (initial state variable for friction)	0.1355
V_{ini} (initial slip speed for friction)	1.000e-12 m/s
V_o (reference slip speed for friction)	1.000e-6 m/s
a (constitutive value in rate-weakening zone)	8.000e-3
b (constitutive value in rate-weakening zone)	1.200e-2
a (constitutive value in rate-strengthening zone)	1.600e-2
L (length parameter in rate-state ageing law)	2.330e-2 m
μ_o (reference friction coefficient)	0.6000
α (normal stress dependence of state variable)	0 (no σ dependence)

Table 3.2: Model properties and friction parameter used for the hydrodynamic model.

Hydrodynamic element size	30 m to 150 m
Hydrodynamic time step	5.370e-1 s
Manning's coefficient	1.300e-2

Chapter 4

Rayleigh-Wave Breakout Phases from 2-D Thrust/Reverse Fault Geometries Under Equivalent Prestress Conditions

4.1 Abstract

The asymmetric geometry of thrust/reverse faults leads to greater slip and greater peak slip rate near the free surface (e.g., the surface of the Earth) (Nielsen, 1998; Oglesby et al., 1998; Oglesby et al., 2000) than analogous vertical faults. Furthermore, when rupture travels updip along a dip-slip fault and reaches the free surface, it produces a Rayleigh-wave breakout phase, a pulse traveling back downdip and along the free surface (Savage,

1965; Burridge and Halliday, 1971; Oglesby et al., 1998; Madariaga, 2003) that has the potential to be readily observed. Properties of the Rayleigh-wave breakout phase are undoubtedly related to the fault slip distribution, and the details of this relationship are not well understood. In particular, these breakout phases are related to fault slip near the free surface, which efficiently generates tsunamis when submarine faults rupture (Okal, 1988; Geist and Bilek, 2001; Geist 2002). We begin to evaluate 2-D earthquake source parameters from characteristics of the Rayleigh-wave field by running 2-D dynamic rupture models on thrust/reverse faults that vary in dip angle and fault curvature, and with equivalent prestress conditions such as constant traction across the fault or variable prestress distributions. We compare traveling Rayleigh-wave breakout properties (vertical amplitude) with fault rupture parameters (e.g., slip distribution) for a variety of fault geometries and two prestress conditions. Preliminary results show that a curved fault geometry with an average dip angle of 30° (15° to 45° dip with constant curvature), relative to a straight fault with a constant 30° dip, shows larger slip rates near the free surface and a larger vertical amplitude of the Rayleigh-wave breakout phase. Additionally, using this average dip angle comparison, curved fault geometries result in reduced free surface deformation and reduced slip. For constant prestress models, and for faults with constant dip, preliminary results show that steeper dip angles produce greater peak vertical displacements, greater slip in most cases, and smaller maximum vertical amplitudes of Rayleigh-wave breakout phases along the footwall; whereas for curved faults, preliminary results show that larger average fault dip angles produce smaller peak vertical displacements, smaller slip, and smaller maximum vertical amplitudes of Rayleigh-wave breakout phases along the footwall. Similar results are seen for variable (decreased shear and normal stress near the free surface) prestress models, but with reduced peak vertical displacements, slip, and maximum vertical amplitude of Rayleigh-wave breakout phases. Such Rayleigh-wave analysis has implications for early estimation of far-field tsunami amplitude, since source parameters are directly related to tsunami generation and propagation.

4.2 Introduction

Numerical models of dip-slip faults show normal stress fluctuations from the free surface boundary condition as rupture propagates updip (e.g., toward the seafloor) (Nielsen, 1998; Oglesby et al., 1998; Oglesby and Archuleta, 2000; Oglesby et al., 2000). Specifically, seismic waves from the rupture hit the free surface, bounce off the free surface, and return to the fault again during the rupture process thereby altering the dynamic stress field on the fault. Moreover, as rupture travels updip along a dip-slip fault and reaches the free surface, a breakout phase results (the rupture front "breaks out" of the elastic material), part of which is a strong Rayleigh wave traveling along the free surface and fault surface (Burridge and Halliday, 1971; Oglesby et al., 1998). These surface waves are directly related to fault slip, and in turn, slip distribution is directly related to tsunami formation. Ma and Archuleta (2006) use dynamic rupture modeling to show that a large fraction of seismic radiation is in the forward direction of rupture propagation (i.e., for surface waves this would be toward the free surface of the footwall) implying that ocean-bottom sensors on the seaward side of subduction zones can potentially record strong Rayleigh waves. Experimental and observational studies provide complementary evidence that reverse faults can produce strong ground motion, with a possible mechanism being the free surface effect described above. Brune (1996) shows that experiments on foam block fault models indicate enhanced slip for reverse fault models relative to normal fault models. Observationally, the 1994 Northridge, California and 1971 San Fernando, California earthquakes – both of which were thrust events – produced larger ground motion than expected (Nason, 1973; Abrahamson and Somerville, 1996).

In this current precursory work, we begin to investigate earthquake source properties in relation to Rayleigh waves so that more robust relationships between earthquakes, tsunamis, and detectable surface waves can be developed. Correlating observed surface waves with accurate faulting properties such as earthquake magnitude and slip distribution is an interesting and ongoing challenge in seismology (Satake, 1985). Additionally, dynamic Rayleigh-wave analysis in relation to earthquake and tsunami properties is in its infancy, with few studies combining realistic time-dependent seafloor movement with tsunami formation and propagation (e.g., Ohmachi et al., 2001). Theoretical studies on seismic seafloor deformation point to areas in earthquake/tsunami science that are in need of further investigation. For example, Kajiura (1970) notes that generated wave energy varies for gravity versus compressional water waves depending on the duration of seafloor deformation, with relatively shorter durations (seconds) resulting in possibly transferring more energy to compressional waves than gravity waves. Similarly, characteristics of tsunamis (e.g., initial wave height distribution) depend on earthquake source parameters such as rise time, fault geometry, and slip distribution (Yamashita and Sato, 1974). However, there are complex and unintuitive relationships between earthquake properties and tsunami properties. Yamashita and Sato (1976) point out that large tsunamis can result from relatively small earthquakes, and small tsunamis can result from relatively large earthquakes. As an example, the 1946 M_s 7.4 Aleutian earthquake (and possible submarine landslide) generated an unexpectedly large tsunami offshore Alaska with wave heights above 100 ft, destroying a lighthouse 45 ft tall at Unimak Island (Yamashita and Sato, 1976). Okal (1988) found effects on tsunami amplitude from temporal and spatial earthquake properties such as directivity due to rupture propagation along the fault, which can produce changes in tsunami radiation patterns.

4.3 Method

We use the 2-D FEM to model dynamic earthquake rupture on both planar and nonplanar thrust/reverse faults as well as their corresponding surface wave fields. Specifically, we use planar fault geometries with constant dip angles of 15°, 30°, 45°, and 60° (green lines, Figure 4.1), and curved fault geometries with dip angles of 15° (shallow) to 30° (deep), 15° to 45°, and 15° to 60° (red lines). The total downdip distance is 40 km for each fault geometry, and each fault intersects the free surface. Artificial nucleation occurs as an expanding rupture front by raising the shear stress to the yield value at 35 km downdip and spreads 3 km (in each direction) along dip from the center nucleation point. We utilize linear slip-weakening friction (e.g., Andrews, 1976), in which the friction coefficient drops, linearly, from a yield value to a kinetic value over a characteristic slip-weakening distance, $d_0 = 0.6\ m$. See Table 4.1 for model and material parameters. Fault shear and normal prestress configurations are both set up to be either completely homogeneous across each fault geometry (horizontal solid and dashed lines in Figure 4.2), or to be constant to a depth of 5 km and then decrease toward the free surface (horizontal solid lines and tilted dashed lines in Figure 4.2). Therefore each fault model starts with either constant shear and normal stress configurations, or variable shear and normal stress configurations near the free surface and constant prestress below a depth of 5 km.

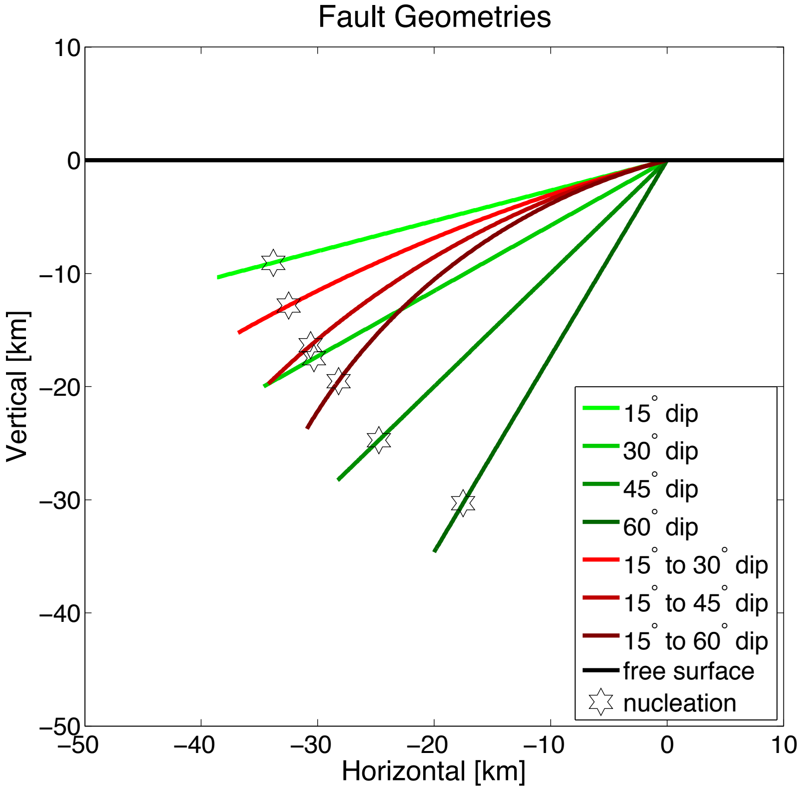

Figure 4.1: Cartoon fault geometries of thrust/reverse faults with constant dip angles of 15°, 30°, 45°, and 60° (green lines), and curved fault geometries with dip angles of 15° (shallow) to 30° (deep), 15° to 45°, and 15° to 60° (red lines). Stars indicate the nucleation zone for each fault.

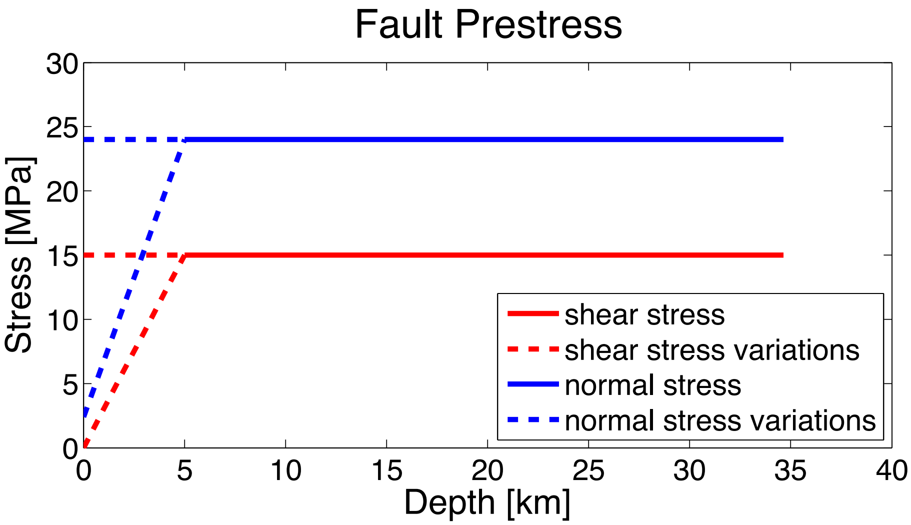

Figure 4.2: Fault shear and normal prestress configurations are set up to be either completely homogeneous across each fault geometry (horizontal solid and dashed lines), or to be constant to a depth of 5 *km* and then decrease toward the free surface (horizontal solid lines and tilted dashed lines).

Table 4.1: Stress values, material properties, model properties, and friction parameters.

τ_o (initial shear stress)	0 to 15.00 MPa
σ_o (initial normal stress)	2.400 to 24.00 MPa
τ_{nuc} (nucleation shear stress)	20.00 MPa
Density	2670 kg/m^3
P-wave speed	6.000 km/s
S-wave speed	3.464 km/s
Nucleation Radius	3.000 km
Nucleation Speed	2.000 km/s
Element Size (along fault)	100.0 m
Time step	3.333e-3 s
Distance Downdip	40.00 km
Dip Angle	15° to 60°
μ_{yield}	0.8299
$\mu_{dynamic}$	0.5487
d_o	0.6000 m

4.4 Results

4.4.1 Rupture Propagation and Vertical Free Surface Deformation

Rupture propagation and vertical free surface deformation for both a straight fault geometry with a constant dip of 30° and a curved fault geometry with variable dip from 15° to 45° and an average dip of 30° are shown in Figures 4.3 through 4.6. Both faults are parameterized with constant prestress. For the planar 30° dipping fault (green curves in Figures 4.3 through 4.6), rupture propagates updip at 4 *s*, 10 *s*, and 16 *s* with increased slip rate (Nielsen, 1998; Oglesby et al., 1998; Oglesby and Archuleta, 2000; Oglesby et al., 2000). Rupture penetrates to the free surface after 16 *s*, and a Rayleigh-wave breakout phase can be seen at 31 *s* (see Figure 4.6) traveling along the hanging wall (HW) and footwall (FW) surfaces. For the nonplanar 15° to 45° dipping fault (red curves in Figures 4.3 through 4.6), rupture propagates updip at 4 *s*, 10 *s*, and 15 *s*, with increased slip rate and with increased amplification relative to the straight fault. Rupture penetrates to the free surface after 15 *s*, and a Rayleigh-wave breakout phase can be seen at 30 *s* traveling along the hanging wall (HW) and footwall (FW) surfaces. Rupture on the curved fault produces hanging wall deformation that is less peaked than the straight fault geometry. Note that we plot the maximum vertical Rayleigh-wave amplitude at 100 *km* perpendicular to strike along the footwall (see for example, Figure 4.3, black dots) in Figures 4.7 and 4.8 for constant and variable prestress configurations, respectively.

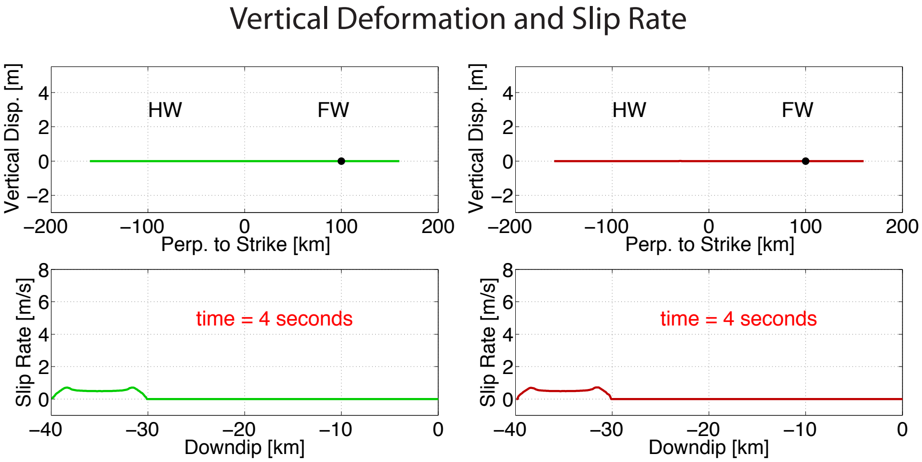

Figure 4.3: Rupture propagation and vertical free surface deformation, at 4 s, for a straight fault geometry (left) with a constant dip of 30° and a curved fault geometry (right) with variable dip from 15° to 45° (with an average dip of 30°). Both geometries have a constant prestress regime.

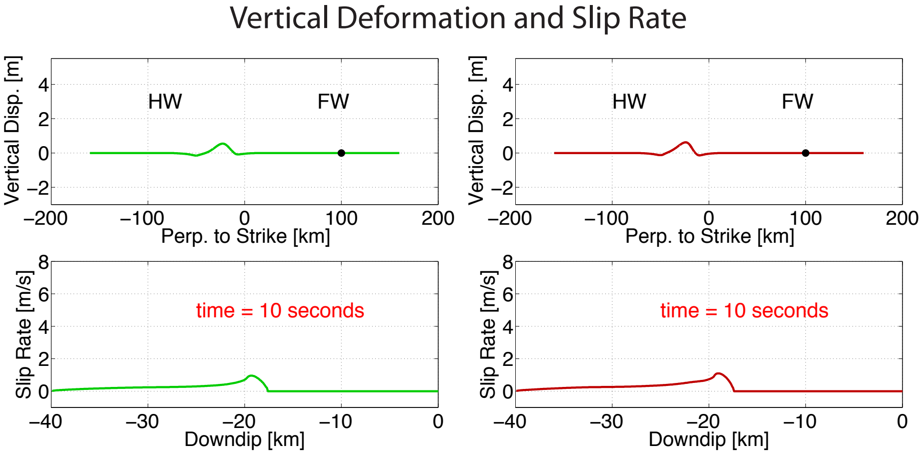

Figure 4.4: Rupture propagation and vertical free surface deformation, at 10 s, for a straight fault geometry (left) with a constant dip of 30° and a curved fault geometry (right) with variable dip from 15° to 45° (with an average dip of 30°). Both geometries have a constant prestress regime.

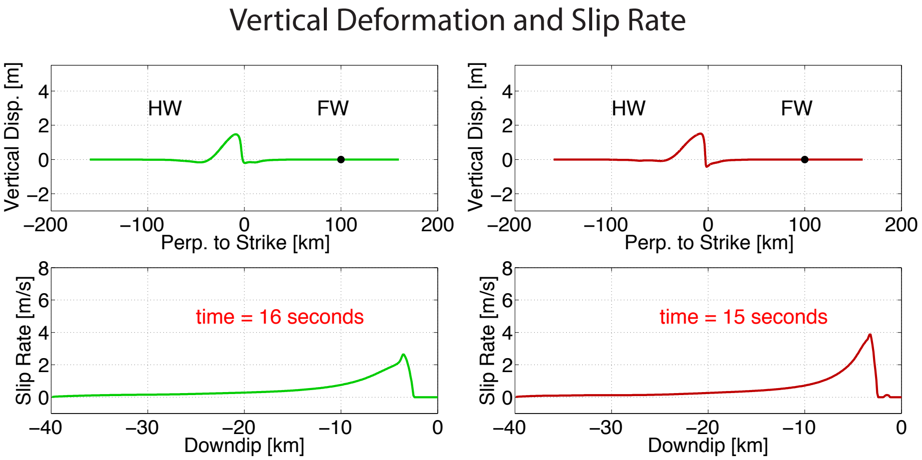

Figure 4.5: Rupture propagation and vertical free surface deformation, at 16 s and 15 s, respectively, for a straight fault geometry (left) with a constant dip of 30° and a curved fault geometry (right) with variable dip from 15° to 45° (with an average dip of 30°). Both geometries have a constant prestress regime.

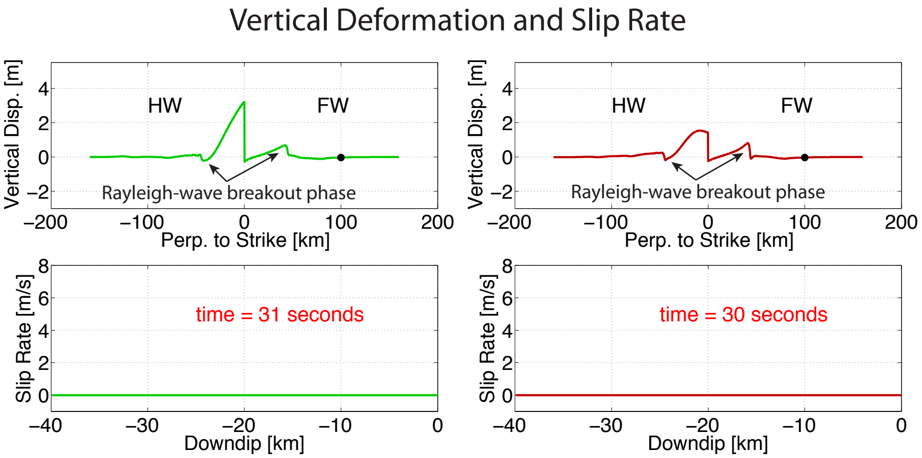

Figure 4.6: Rupture propagation and vertical free surface deformation, at 31 s and 30 s, respectively, for a straight fault geometry (left) with a constant dip of 30° and a curved fault geometry (right) with variable dip from 15° to 45° (with an average dip of 30°). Both geometries have a constant prestress regime.

4.4.2 Vertical Free Surface Deformation, Total Slip, and Maximum Vertical Rayleigh-wave Amplitude

Vertical free surface deformation, total slip, and maximum vertical Rayleigh-wave amplitude at 100 *km* perpendicular to strike along the footwall (see, for example, Figure 4.3, black dots) for thrust/reverse faults with constant normal and shear prestress configurations are shown in Figure 4.7. For constant dip models, larger dip angles produce greater (positive and negative) peak vertical surface displacements, greater slip, and smaller maximum vertical amplitudes of Rayleigh-wave breakout phases along the footwall. With respect to total slip, an exception occurs for the 15° dipping fault which shows the greatest slip, possibly due to the fault's proximity to the free surface (i.e., reduced normal stress for a significant portion of the fault during the rupture process). For variable dip models, larger average fault dip angles produce smaller (positive and negative) peak vertical surface displacements, smaller slip, and smaller maximum vertical amplitudes of Rayleigh-wave breakout phases along the footwall. Vertical free surface deformation, total slip, and maximum vertical Rayleigh-wave amplitude at 100 *km* perpendicular to strike along the footwall (see, for example, Figure 4.3, black dots) for thrust/reverse faults with variable normal and shear prestress configurations are shown in Figure 4.8. For constant dip models, larger dip angles produce greater (positive and negative) peak vertical displacements, greater slip, and smaller maximum vertical amplitudes of Rayleigh-wave breakout phases along the footwall. For variable dip models, larger average fault dip angles produce smaller (positive and negative) peak vertical displacements, smaller slip that tends to converge near the free surface, and smaller maximum vertical amplitudes of Rayleigh-wave breakout phases along the footwall. Overall, models with reduced shear and normal prestress near the free surface show reduced maximum vertical amplitudes of Rayleigh-wave breakout phases, but have a pattern corresponding to dip angle that is similar to that of the constant prestress models.

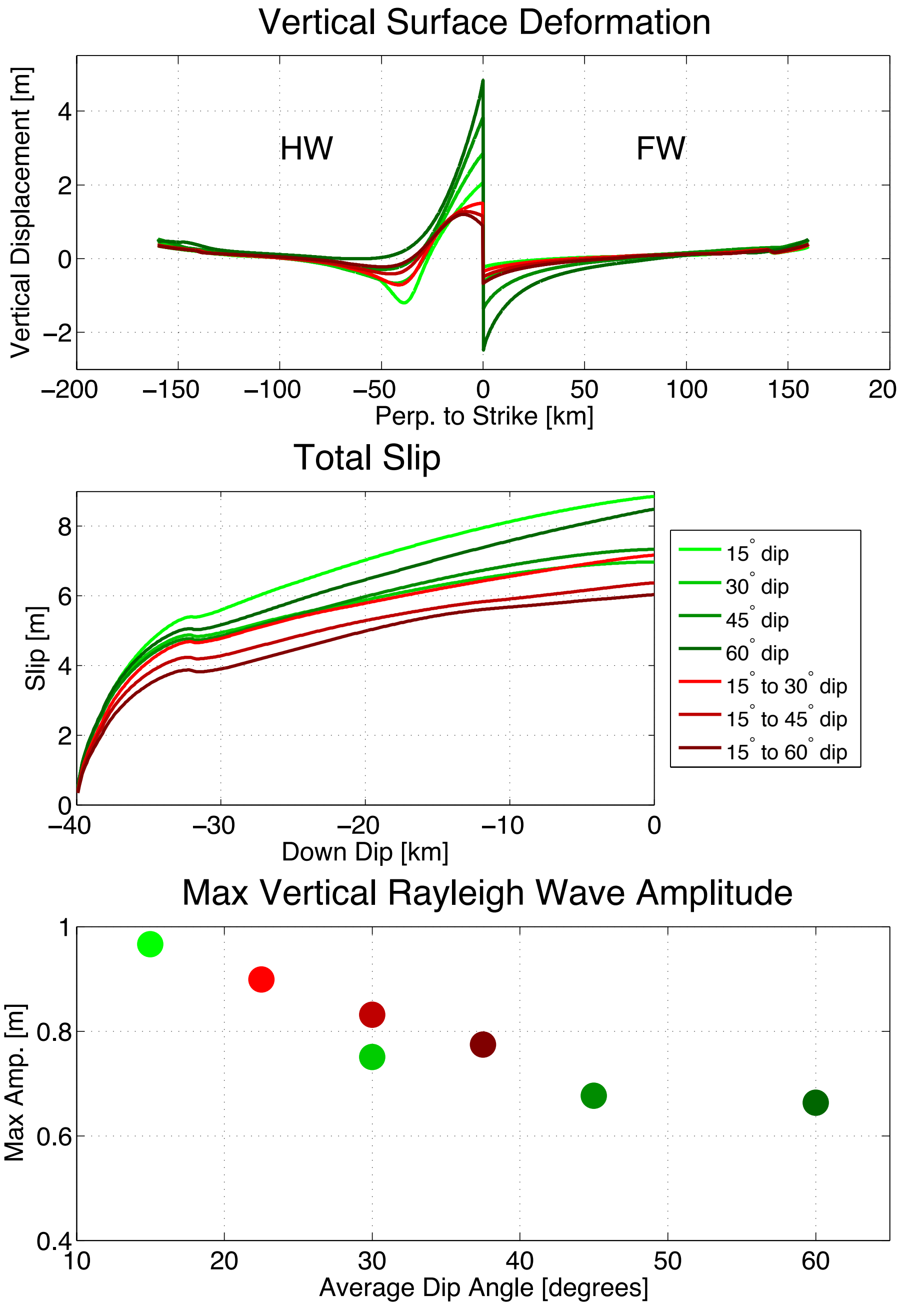

Figure 4.7: Vertical free surface deformation, total slip, and maximum vertical Rayleigh-wave amplitude at 100 km perpendicular to strike along the footwall (see, for example, Figure 4.3, black dots) for thrust/reverse faults with constant normal and shear prestress configurations (Figure 4.2).

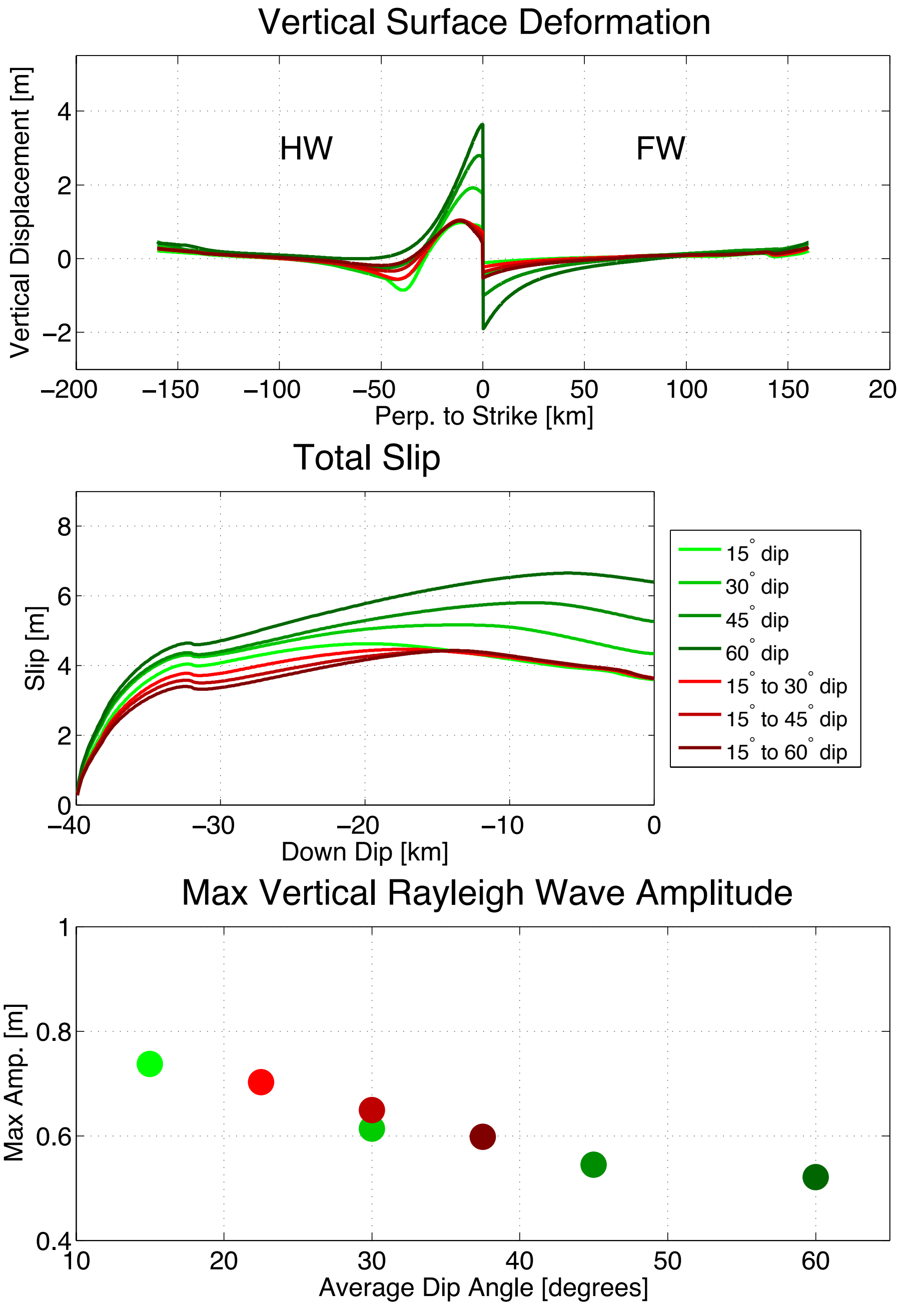

Figure 4.8: Vertical free surface deformation, total slip, and maximum vertical Rayleigh-wave amplitude at 100 *km* perpendicular to strike along the footwall (see, for example, Figure 4.3, black dots) for thrust/reverse faults with variable normal and shear prestress configurations (Figure 4.2).

4.5 Conclusions and Future Work on Rayleigh Waves and Tsunamis

We evaluate source parameters and Rayleigh-wave breakout phases for 2-D thrust/reverse faults that vary in dip angle and fault curvature, and with equivalent prestress conditions such as constant traction across the fault or variable prestress distributions. We compare traveling Rayleigh-wave breakout (vertical) amplitudes with earthquake source parameters – including slip distribution and vertical free surface deformation – for a variety of fault geometries and two prestress conditions. Overall, models with larger slip near the free surface result in greater vertical amplitude Rayleigh waves (Figures 4.7 and 4.8). Using an average dip angle comparison, curved fault geometries result in reduced free surface deformation and slip, but increased slip rate near the free surface and greater amplitude Rayleigh-wave breakout phases (Figures 4.3 through 4.6), relative to the straight fault geometries. For constant prestress models, and for faults with constant dip, steeper dip angles produce greater peak vertical displacements, greater slip, and smaller maximum amplitudes of Rayleigh-wave breakout phases along the footwall (with the exception of the 15°-dipping fault; whereas for faults with variable dip, larger average fault dip angles produce smaller peak vertical displacements, smaller slip, and smaller maximum amplitudes of Rayleigh-wave breakout phases along the footwall. Similar results are seen for models with decreased shear and normal stress near the free surface, but with reduced peak vertical displacements, slip, and maximum amplitudes of Rayleigh-wave breakout phases. Models like these can provide a foundation for future work on the dynamics of submarine earthquakes, their Rayleigh wave fields, and corresponding tsunamis. One important factor in this study appears to be the shallowest dipping faults. For the faults that dip at 15°, this relatively small dip angle appears to have a very strong influence on the displacement and particle velocity fields. Further investigation is needed to determine how the dynamic fluctuations in normal stress contribute to these results. For curved fault geometries, the radius of curvature may have significant effects on fault slip distribution and free surface displacement, and this needs to be explored further as well.

Considerable discrepancies have been pointed out between tsunami models and tsunami observations, particularly in tsunami height and travel time (Ohmachi et al., 2001). Such discrepancies may result from uncertainties in earthquake source models that are based on seismic-wave and tsunami data (Imamura et al., 1994). Future work will involve stochastic prestress distributions that decrease (to zero) in magnitude toward the fault edges (e.g., Andrews and Barall, 2011). Additionally, we will use the time-dependent free surface deformation from the rupture models as input into a tsunami code. Lastly, we plan to compare our results to observed earthquakes and tsunamis – such as the 2012 Haida Gwaii Earthquake and Tsunami – that appears to have Rayleigh-wave phases recorded on ocean bottom pressure sensors ahead of the main tsunami (`http://www.ndbc.noaa.gov/dart.shtml`). Such Rayleigh-wave analysis has implications for early estimation of far-field tsunami amplitude, since source parameters are directly related to tsunami generation and propagation.

Chapter 5

Conclusions

It is important to combine physics-based, dynamic earthquake models, which do not prescribe fault slip, with tsunami models. This method is still in its infancy, and as such needs to be explored more extensively. The potential occurrence of earthquakes and tsunamis offshore southern Alaska is relatively high and is one prime location for modeling efforts to examine effects from earthquake-generated tsunamis (e.g., Ryan et al., 2012). The physical properties of the plate interface, such as the functional form of the friction coefficient during sliding, can have significant effects on rupture dynamics (e.g., Harris and Day, 1993). We are able to incorporate rate-strengthening-like zones in dynamic earthquake rupture models by tuning the friction coefficients in time-weakening friction. Ultimately, strengthening zones result in a reduction in fault slip, and therefore a reduction in tsunami amplitude above and near the strengthening zone. The location of the strengthening zone can have a great impact on the overall slip distribution, and for strengthening zone models, the beaming pattern of the near-field tsunami is significantly altered, which could have implications for distant coastlines. Future work will involve more accurate integration of plate coupling data from GPS models (e.g., Freymueller et al., 2008). Additionally, we will implement stochastic prestress (e.g., Andrews and Barall, 2011) and stochastic frictional zones that are likely more representative of natural stress and friction distributions. Including a more accurate fault geometry (e.g., changing dip angle with depth) and material properties (e.g., velocity structure models) into the earthquake rupture code can also make modeling efforts more realistic.

In addition to large megathrust earthquakes and their associated tsunamis, smaller earthquakes are capable of generating devastating local tsunamis that do not provide much warning time. For southern California, the Ventura Basin and surrounding coastal region pose a significant earthquake and tsunami threat (Rockwell, 2011; Hubbard et al., 2014). Earthquake sources on the Pitas Point and Red Mountain faults should be included in tsunami hazard assessments offshore California. Our dynamic models show large northward and eastward tsunami amplitudes from rupture on the Pitas Point and Lower Red Mountain faults. However, this parameterization results in a large earthquake that is less likely, in a given time frame, than smaller earthquake scenarios on this fault system. A range of dynamic earthquake and tsunami models is needed for this area so that we can begin to robustly determine earthquake/tsunami scenarios that are more likely versus scenarios that are less unlikely. Such suites of models will involve different prestress and velocity distributions, different friction distributions, and may encompass several regional faults.

Constraining properties of the tsunami from leading Rayleigh waves can provide a route to more enhanced early warning that includes local effects from properties such as fault slip distribution and bathymetry. We have begun to evaluate some source parameters and Rayleigh-wave breakout phases for 2-D thrust/reverse faults that vary in dip angle and fault curvature, and with equivalent prestress conditions such as constant traction across the fault or variable prestress distributions. Models with larger slip near the free surface result in greater vertical amplitude Rayleigh waves. Using an average dip angle comparison, curved fault geometries result in reduced free surface deformation and slip, but increased slip rate near the free surface and greater amplitude Rayleigh-wave breakout phases, relative to the straight fault geometries. For constant prestress models, and for faults with constant dip, steeper dip angles produce greater peak vertical displacements, greater slip, and smaller maximum amplitudes of Rayleigh-wave breakout phases along the footwall; whereas for faults with variable dip, larger average fault dip angles produce smaller peak vertical displacements, smaller slip, and smaller maximum amplitudes of Rayleigh-wave breakout phases along the footwall. Similar results are seen for models with decreased shear and normal stress near the free surface, but with reduced peak vertical displacements, slip, and maximum amplitudes of Rayleigh-wave breakout phases. Future work will involve stochastic prestress distributions. Using time-dependent free surface deformation from the rupture models as input into a tsunami code may help shed some light on observed earthquake and tsunami processes – such as the 2012 Haida Gwaii Earthquake and Tsunami – that appear to show Rayleigh-wave phases recorded on ocean bottom pressure sensors ahead of the main tsunami. Transient vertical seafloor displacements from passing Rayleigh waves may be detectable by ocean bottom pressure sensors if the Rayleigh-wave speed is much faster than the speed of sound in the ocean (i.e., traveling Rayleigh waves will produce pressure changes in the water column). However, determining how such pressure observations relate to both fault slip distributions (in time) as well as the corresponding tsunami wave-train properties will be challenging.

Tsunami disaster mitigation leads to a need for tsunami early warning, especially on coastlines prone to large megathrust earthquakes and their resultant tsunamis such as highly populated coastal regions along the Pacific Rim. Earthquake source parameters such as seismic moment and slip distribution have first-order effects on tsunami size (e.g., Geist, 1998). Therefore, by constraining earthquake source parameters from characteristics of the Rayleigh-wave field, one can also constrain tsunami properties such as size and wave train structure (Dutykh and Dias, 2008). Such Rayleigh-wave analysis has implications for early estimation of far-field tsunami amplitude, since source parameters are directly related to tsunami generation and propagation. More accurate tsunami warning is still elusive due to large uncertainties in what causes the distribution of tsunami size and devastation; therefore, Rayleigh-wave observations from tide gauges and ocean bottom seismometers should be compared to wave models, serving as a model validation, while models can help bound the spatial and temporal limits for potential observations so that we can assess the ability of Rayleigh-wave analysis in determining tsunami wave train structure.

Bibliography

Abrahamson, N. A. and Somerville, P. G. (1996). Effects of the hanging wall and footwall on ground motions recorded during the northridge earthquake. *Bull. Seismol. Soc. Am.*, 86:S93–S99.

Aki, K. and Richards, P. G. (2009). *Quantitative Seismology.* University Science Books, 2nd edition.

Ammon, C. J., Lay, T., Kanamori, H., and Cleveland, M. (2011). A rupture model of the 2011 off the pacific coast of tohoku earthquake. *Earth Planets Space*, 63:693–696.

Andrews, D. J. (1976). Rupture propagation with finite stress in antiplane strain. *Journal of Geophysical Research*, 81(20):3575–3582.

Andrews, D. J. (2004). Rupture models with dynamically determined breakdown displacement. *Bulletin of the Seismological Society of America*, 94(3):769–775.

Andrews, D. J. and Barall, M. (2011). Specifying initial stress for dynamic heterogeneous earthquake source models. *Bull. Seismol. Soc. Am.*, 101(5):2408–2417.

Barall, M. (2009). A grid-doubling finite-element technique for calculating dynamic three-dimensional spontaneous rupture on an earthquake fault. *Geophys. J. Int.*, 178:845–859.

Beroza, G. C. and Mikump, T. (1996). Short slip duration in dynamic rupture in the presence of heterogeneous fault properties. *J. Geophys. Res.*, 101(22):449–460.

Bilek, S. L. and Lay, T. (2002). Tsunami earthquakes possibly widespread manifestations of frictional conditional stability. *Geophys. Res. Lett.*, 29:doi:10.1029/2002GL015215.

Blanpied, M. L., Tullis, T. E., and Weeks, J. D. (1998). Effects of slip, slip rate, and shear heating on the friction of granite. *J. Geophys. Res.*, 103:489–511.

Borrero, J. C., Dolan, J. F., and Synolakis, C. E. (2001). Tsunamis within the eastern santa barbara channel. *Geophys. Res. Lett.*, 28(4):643–646.

Brune, J. N. (1996). Particle motions in a physical model of shallow angle thrust faulting. *Proc. Indian Acad. Sci. (Earth Planet. Sci.)*, pages L196–L206.

Bruns, T. R., von Huene, R., Culotta, R. C., Lewis, S. D., and Ladd, J. W. (1987). *Geology and Potential of the Continental Margin of Western North America and Adjacent Basis, Circumpacific Council for Energy and Mineral Resources*, chapter Geology and Petroleum Potential of the Shumagin Margin, Alaska, pages 157–189.

Burridge, R. and Halliday, G. S. (1971). Dynamic shear cracks with friction as models for shallow focus earthquakes. *Geophys. J. R. astr. Soc.*, 25:261–283.

Chester, F. M. and Higgs, N. G. (1992). Multimechanism friction constitutive model for ultrafine quartz gouge at hypocentral conditions. *J. Geophys. Res.*, 97:1859–1870.

Christensen, N. I. and Mooney, W, D. (1995). Seismic velocity structure and composition of the continental crust: A global view. *J. Geophys. Res.*, 100:9761–9788.

Cocco, M. and Rovelli, A. (1989). Evidence for the variation of stress drop between normal and thrust faulting earthquakes in italy. *J. Geophys. Res.*, 94:9399–9416.

Cummins, P. R. and Kaneda, Y. (2000). Possible splay fault slip during the 1946 nankai earthquake. *Geophys. Res. Lett.*, 27:2725–2728.

Currie, I. G. (2013). *Fundamental Mechanics of Fluids*. Taylor and Francis Group, 4th edition.

Dalguer, L. A. and Day, S. M. (2007). Staggered-grid split-node method for spontaneous rupture simulation. *J. Geophys. Res.*, 112:doi:10.1029/2006JB004467.

Day, S. M. (1982). Three-dimensional simulation of spontaneous rupture: The effect of nonuniform prestress. *Bull. Seismol. Soc. Am.*, 72:1881–1902.

Dean, R. G. and Dalrymple, R. A. (1991). *Water Wave Mechanics for Engineers and Scientists*. World Scientific Publishing Co. Pte. Ltd.

Dedontney, N. and Rice, J. R. (2012). Tsunami wave analysis and possibility of splay fault rupture during the 2004 indian ocean earthquake. *Pure Appl. Geophys.*, 169:1707–1735.

Dieterich, J. H. (1978). Time-dependent friction and the mechanics of stick-slip. *Pure and Applied Geophysics*, 116:790–806.

Dieterich, J. H. (1979). Modeling of rock friction 1. experimental results and constitutive equations. *Journal of Geophysical Research*, 84(B5):2161–2168.

Dieterich, J. H. (1992). Earthquake nucleation on faults with rate- and state-dependent strength. *J. Geophys. Res.*, 211:115–134.

Duan, B. and Day, S. M. (2008). Inelastic strain distribution and seismic radiation from rupture of a fault kink. *J. Geophys. Res.*, 113:doi:10.1029/2008JB005847.

Duan, B. and Oglesby, D. D. (2006). Heterogeneous fault stresses from previous earthquakes and the effect on dynamics of parallel strike-slip faults. *J. Geophys. Res.*, 111:doi:10.1029/2005JB004138.

Dutykh, D. and Dias, F. (2008). Tsunami generation by dynamic displacement of sea bed due to dip-slip faulting. *Mathematics and Computers in Simulation*, 80(4):837–848.

Ewing, M., Tolstoy, I., and Press, F. (1950). Proposed use of the t phase in tsunami warning systems. *Bull. Seismol. Soc. Am.*, 40:53–58.

Fisher, M. A., Normark, W. R., Greene, H. G., Lee, H. J., and Sliter, S. W. (2005). Geology and tsunamigenic potential of submarine landslides in santa barbara channel, southern california. *Mar. Geol.*, 224:1–22.

Fisher, M. A., Sorlien, C. C., and Sliter, R. W. (2009). Potential earthquake faults offshore southern california, from the eastern santa barbara channel south to dana point. pages 271–290. Geol. Soc. Am., Spec. Pap.

Freymueller, J. T. and Beavan, J. (1999). Absence of strain accumulation in the western shumagin segment of the alaska subduction zone. *Geophys. Res. Lett.*, 26:3233–3236.

Freymueller, J. T., Woodard, H., Cohen, S. C., Cross, R., Elliot, J., Larsen, C. F., Hreinsdóttir, S., and Zweck, C. (2008). Active deformation processes in alaska, based on 15 years of gps measurements. In *Active Tectonics and Seismic Potential of Alaska, Geophysical Monograph Series 179, American Geophysical Union*, page doi:10.1029/179GM02.

Fujima, K., Matsutomi, H., Tsuji, Y., Kawata, Y., and Takahashi, T. (1999). Discussions on the source of 1998 papua new guinea earthquake tsunami. pages 381–385. Proc. Coastal Eng. Jpn. JSCE 46.

Geist, E. L. (1998). Local tsunamis and earthquake source parameters. *Adv. Geophys.*, 39:117–209.

Geist, E. L. (2002). Complex earthquake rupture and local tsunamis. *J. Geophys. Res.*, 107:doi:10.1029/2000JB000139.

Geist, E. L. and Bilek, S. L. (2001). Effect of depth-dependent shear modulus on tsunami generation along subduction zones. *Geophys. Res. Lett.*, 28:1315–1318.

Geist, E. L. and Dmowska, R. (1999). Local tsunamis and distributed slip at the source. *Pure Appl. Geophys.*, 154:485–512.

Geist, E. L., Titov, V. V., Arcas, D., Pollitz, F. F., and Bilek, S. L. (2007). Implications of the 26 december 2004 sumatra–andaman earthquake on tsunami forecast and assessment models for great subduction-zone earthquakes. *Bull. Seismol. Soc. Am.*, 97(1A):S249–S270.

Guatteri, M., Mai, P. M., Beroza, G. C., and Boatwright, J. (2003). Strong ground-motion prediction from stochastic-dynamic source models. *Bull. Seismol. Soc. Am.*, 93:301–313.

Guatteri, M. and Spudich, P. (2000). What can strong-motion data tell us about slip-weakening fault-friction laws? *Bull. Seismol. Soc. Am.*, 90:98–116.

Halliday, D. and Resnick, R. (1974). *Fundamentals of Physics.* John Wiley and Sons.

Harris, R. A., Barall, M., Andrews, D. J., Duan, B., Ma, S., Dunham, E. M., Gabriel, A.-A., Kaneko, Y., Kase, Y., Aagaard, B. T., Oglesby, D. D., Ampuero, J.-P., Hanks, T. C., and Abrahamson, N. (2011). Verifying a computational method for predicting extreme ground motion. *Seismol. Res. Lett.*, 82:638–644.

Harris, R. A., Barall, M., Archuleta, R., Dunham, E., Aagaard, B., Ampuero, J. P., Bhat, H., Cruz-Atienza, V., Dalguer, L., Dawson, P., Day, S., Duan, B., Ely, G., Kaneko, Y., Kase, Y., Lapusta, N., Liu, Y., Ma, S., Oglesby, D., Olsen, K., Pitarka, A., Song, S., and Templeton, E. (2009). The scec/usgs dynamic earthquake rupture code verification exercise. *Seismol. Res. Lett.*, 90:119–126.

Harris, R. A. and Day, S. M. (1993). Dynamics of fault interaction: Parallel strike-slip faults. *J. Geophys. Res.*, 98:4461–4472.

Hauksson, E. (2014). Average stress drops of southern california earthquakes in the context of crustal geophysics: Implications for fault zonehealing. *Pure Appl. Geophys.*, pages doi:10.1007/s00024–014–0934–4.

Hayes, G. P., Wald, D. J., and Johnson, R. L. (2012). A three-dimensional model of global subduction zone geometries. *J. Geophys. Res.*, 117:doi:10.1029/2011JB008524.

Hubbard, J., Shaw, J. H., Dolan, J., Pratt, T. L., McAuliffe, L., and Rockwell, T. K. (2014). Structure and seismic hazard of the ventura avenue anticline and ventura fault, california: Prospect for large, multisegment ruptures in the western transverse ranges. *Bull. Seismol. Soc. Am.*, 104(3):doi: 10.1785/0120130125.

Hughes, T. J. R. (2000). *The Finite Element Method: Linear Static and Dynamic Finite Element Analysis*. Dover Publications, Inc.

Hyndman, R. D., Yamano, M., and Oleskevich, D. A. (1997). The seismogenic zone of subduction thrust faults. *The Island Arc*, 6:244–260.

Ida, Y. (1972). Cohesive force across the tip of a longitudinal-shear crack and griffith's specific surface energy. *J. Geophys. Res.*, 77:3796–3805.

Imamura, F., Takahashi, T., and Takahashi, T. (1994). Is the fault plane dipping toward the east or west?—interpretation from tsunami data. pages 179–184. Kaiyo Monthly 7, 179-184.

Johnson, J. and Satake, K. (1994). Rupture extent of the 1938 alaskan earthquake as inferred from tsunami waveforms. *Geophys. Res. Lett.*, 21:733.

Kajiura, K. (1970). Tsunami source, energy and the directivity of wave radiation. *Bull. Earthquake Res. Inst., Univ. Tokyo*, 48:835–869.

Kame, N., Rice, J. R., and Dmowska, R. (2003). Effects of pre-stress state and rupture velocity on dynamic fault branching. *J. Geophys. Res.*, 108(2265):doi: 2210.1029/2002JB002189.

Kanamori, H. (1972). Mechanism of tsunami earthquakes. *Phys. Earth Planet In.*, 6:346–359.

Kanamori, H. and Rivera, L. (2006). Energy partitioning during an earthquake. In *Earthquakes: Radiated Energy and the Physics of Faulting Geophysical Monograph Series 170*, pages 3–13.

Kirby, S., Scholl, D., von Huene, R., and Wells, R. (2013). Alaska earthquake source for the safrr tsunami scenario. Technical report, U.S. Geol. Surv. Open File Rep. 2013-1170-B, edited by Ross, S. L. and Jones, L. M., Chap. B, pp. 40.

Kozdon, J. E. and Dunham, E. (2013). Rupture to the trench: Dynamic rupture simulations of the 11 march 2011 tohoku earthquake. *Bull. Seismol. Soc. Am.*, 103:1275–1289.

Lander, J. F., Lockridge, P. A., and Kozuch, M. J. (1993). Tsunamis affecting the west coast of the united states 1806–1992, ngdc key to geophysical records documentation kgrd-29. Technical report, pp. 242, U.S. Dep. of Commer., NOAA, Natl. Geophys. Data Cent., Boulder, Colo.

Lapusta, N., Rice, J. R., Ben-Zion, Y., and Zheng, G. (2000). Elastodynamic analysis for slow tectonic loading with spontaneous rupture episodes on faults with rate- and state-dependent friction. *J. Geophys. Res.*, 105:doi:10.1029/2000JB900250.

Lay, T., Kanamori, H., Ammon, C. J., Nettles, M., Ward, S. N., Aster, R. C., Beck, S. L., Bilek, S. L., Brudzinski, M. R., Butler, R., and DeShon, H. R. (2005). The great sumatra-andaman earthquake of 26 december 2004. *Science*, 308:1127–1133.

LeVeque, R. J. (2007). *Finite Difference methods for Ordinary and Partial Differential Equations*. Society for Industrial and Applied Mathematics.

Linker, M. F. and Dieterich, J. H. (1992). Effects of variable normal stress on rock friction: Observations and constitutive equations. *J. Geophys. Res.*, 97:4923–4940.

Liu, P. L.-F. (2009). *The Sea, Tsunamis*, chapter 9: Tsunami modeling - propagation.

Liu, P. L.-F., Cho, Y. S.and Yoon, S. B., and Seo, S. N. (1995). *Tsunami: Progress in Prediction, Disaster Prevention and Warning*, chapter Numerical simulations of the 1960 Chilean tsunami propagation and inundation at Hilo, Hawaii, pages 99–115.

Ma, S. and Archuleta, R. J. (2006). Radiated seismic energy based on dynamic rupture models of faulting. *J. Geophys. Res.*, 111:1978–2012.

Madariaga, R. (2003). Radiation from a finite reverse fault in a half space. *Pure Appl. Geophys.*, 160:555–577.

Marshall, S. T., Funning, G. J., and Owen, S. E. (2013). Fault slip rates and interseismic deformation in the western transverse ranges, california. *J. Geophys. Res.*, 118:4511–4534.

Matsuyama, M., Imamura, F., Hashi, K., Matsutomi, T., and Tsuji, Y. (1999). Numerical analysis of 1998 papua new guinea earthquake tsunami. pages 386–390. Proc. Coastal Eng. Jpn., JSCE 46.

McGarr, A. (1984). Scaling of ground motion parameters, state of stress, and focal depth. *J. Geophys. Res.*, 89:6969–6979.

Nason, R. (1973). Increased seismic shaking above a thrust fault, in san fernando, california, earthquake of february 9, 1971. Technical report, pp. 123–126, U.S. Dep. of Commerce, Washington, D. C.

Navon, I. M. (1979). Finite-element simulation of the shallow-water equations model on a limited-area domain. *Appl. Math Modelling*, 3:337–348.

Nielsen, S. B. (1998). Free surface effects on the propagation of dynamic rupture. *Geophys. Res. Lett.*, 25:125–128.

Oglesby, D. D. and Archuleta, R. J. (2000). Dynamics of dip-slip faulting: Explorations in two dimensions. *J. Geophys. Res.*, 105:13643–13653.

Oglesby, D. D. and Archuleta, R. J. (2003). The three-dimensional dynamics of a nonplanar thrust fault. *Bull. Seismol. Soc. Am.*, 93:2222–2235.

Oglesby, D. D., Archuleta, R. J., and Nielsen, S. B. (1998). Earthquakes on dipping faults: The effects of broken symmetry. *Science*, 280:1055–1059.

Oglesby, D. D., Archuleta, R. J., and Nielsen, S. B. (2000). The three-dimensional dynamics of dipping faults. *Bull. Seismol. Soc. Am.*, 90:616–628.

Oglesby, D. D. and Mai, P. M. (2012). Fault geometry, rupture dynamics and ground motion from potential earthquakes on the north anatolian fault under the sea of marmara. *Geophys. J. Int.*, 188:1071–1087.

Oglesby, D. D., Mai, P. M., Atakan, K., and Pucci, S. (2008). Dynamic models of earthquakes on the north anatolian fault zone under the sea of marmara: Effect of hypocenter location. *Geophys. Res. Lett.*, 35:doi:10.1029/2008GL035037.

Ohmachi, T., Tsukiyama, H., and Matsumoto, H. (2001). Simulation of tsunami induced by dynamic displacement of seabed due to seismic faulting. *Bull. Seismol. Soc. Am.*, 91:1898–1909.

Okada, Y. (1985). Surface deformation due to shear and tensile faults in a half-space. *Bull. Seismol. Soc. Am.*, 75:1135–1154.

Okal, E. A. (1988). Seismic parameters controlling far-field tsunami amplitudes: a review. *Nat. Hazards*, 1:67–96.

Olsen, K. B., Day, S. M., Dalguer, L. A., Mayhew, J., Cui, Y., Zhu, J., Cruz-Atienza, V. M., Roten, D., Maechling, P., Jordan, T. H., Okaya, D., and Chourasia, A. (2009).

Shakeout-d: Ground motion estimates using an ensemble of large earthquakes on the southern san andreas fault with spontaneous rupture propagation. *Geophys. Res. Lett.*, 36:doi:10.1029/2008GL036832.

Olsen, K. B., Madariaga, R., and Archuleta, R. J. (1997). Three-dimensional dynamic simulation of the 1992 landers earthquake. *Science*, 278:834–838.

Owczarek, J. A. (1968). *Introduction to Fluid Mechanics*. International Textbook Company.

Perry, S. S. and Bryant, W. A. *Fault Number 91, Ventura fault, in Quaternary fault and fold database of the United States: US Geological Survey website.* http://earthquakes.usgs.gov/regional/qfaults.

Peyrat, S., Olsen, K., and Madariaga, R. (2001). Dynamic modeling of the 1992 landers earthquake. *J. Geophys. Res.*, 106:26467–26482.

Pinter, N., Lueddecke, S. B., Keller, E. A., and Simmons, K. R. (1998). Late quaternary slip on the santa cruz island fault, california. *Geol. Soc. Am. Bull.*, 110(6):711–722.

Plesch, A. et al. (2007). Community fault model (cfm) for southern california. *Bull. Seismol. Soc. Am.*, 97(6):1793–1802.

Rabinowicz, E. (1951). The nature of the static and kinetic coefficients of friction. *Journal of Applied Physics*, 22(11):1373–1379.

Rockwell, T. K. (2011). Large co-seismic uplift of coastal terraces across teh ventura anticline: Implications for the size of earthquakes and the potential for tsunami generation. Southern California Earthquake Center Annual Meeting, Palm Springs, CA.

Ross, S. L. et al. (2004). Comments on potential geologic and seismic hazards affecting coastal ventura county, california. Technical report, U.S. Geol. Surv. Open File Rep., 2004–1286.

Ruina, A. (1980). *Friction laws and instabilities: A quasistatic analysis of some dry friction behavior*. PhD thesis, Brown Univ., Providence, R. I.

Ruina, A. (1983). Slip instability and state variable friction laws. *Journal of Geophysical Research*, 88(B12):10359–10370.

Ryan, H., von Huene, R., Scholl, D., and Kirby, S. (2012). Tsunami hazards to u.s. coasts from giant earthquakes in alaska. *EOS, Transactions American Geophysical Union*, 93(185):doi:10.1029/2012EO190001.

Ryan, K. J. (2012). Dynamic models of earthquake rupture on fault stepovers and dip-slip faults using various friction formulations. Master's thesis, Univ. of California, Riverside.

Ryan, K. J., Geist, E. L., Barall, M., and Oglesby, D. D. (2015). Dynamic models of an earthquake and tsunami offshore ventura, california. *Geophys. Res. Lett.*, 42(16):6599–6606.

Ryan, K. J. and Oglesby, D. D. (2014). Dynamically modeling fault step overs using various friction laws. *Journal of Geophysical Research*, pages 5814–5829.

Ryan, K. J., Oglesby, D. D., and Geist, E. L. (2013). Modeling sea-floor deformation and tsunami generation using dynamic finite element analysis. Technical report, U.S. Geol. Surv. Open File Rep. 2013-1170-D, edited by Geist, E. L., Chap. D, pp. 6-35.

Santini, S., Dragoni, M., and Spada, G. (2003). Asperity distribution of the 1964 great alaska earthquake and its relation to subsequent seismicity in the region. *Tectonophysics*, 367:219–233.

Sarna-Wojeicki, A. M., Williams, K. M., and Yerkes, R. F. (1976). Geology of the ventura fault, ventura county, california.

Satake, K. (1985). The mechanism of the 1983 japan sea earthquake as inferred from long-period surface waves and tsunamis. *Phys. Earth Planet In.*, 37:249–260.

Satake, K. (2002). *Tsunamis, International Handbook of Earthquake and Engineering Seismology, Part A*, pages 437–451.

Satake, K. (2007). *Treatise on geophysics, Volume 4-Earthquake seismology*, chapter Tsunamis, pages 483–511.

Savage, J. C. (1965). The stopping phase on seismograms. *Bull. Seismol. Soc. Am.*, 55(1):47–58.

Scholz, C. H. (1998). Earthquakes and friction laws. *Nature*, 391:37–42.

Shearer, P. (2009). *Introduction to Seismology.* Cambridge University Press, New York.

Shuto, N. (1991). Numerical simulation of tsunamis - its present and near future. *Nat. Hazards*, 4:171–191.

Simons, M., Minson, S. E., Sladen, A., Ortega, F., Jiang, J., Owen, S. E., Meng, L., Ampuero, J. P., Wei, S., Chu, R., and Helmberger, D. V. (2011). The 2011 magnitude 9.0 tohoku-oki earthquake: Mosaicking the megathrust from seconds to centuries. *Science*, 332:1421–1425.

Sokolnikoff, I. S. (1956). *Mathematical Theory of Elasticity.* McGraw-Hill Book Company, Inc.

Stein, S. and Wysession, M. (2003). *An Introduction to Seismology, Earthquakes, and Earth Structure.* Blackwell Publishing.

Strang, G. (2007). *Computational Science and Engineering.* Wellesley-Cambridge Press.

Tanioka, Y. and Satake, K. (1996). Tsunami generation by horizontal displacement of ocean bottom. *Geophys. Res. Lett.*, 23:861–864.

Townley, S. D. and Allen, M. W. (1939). Descriptive catalog of earthquakes of the pacific coast of the united states 1769 to 1928. *Bull. Seismol. Soc. Am.*, 29(1):1–297.

Ulrich, F. P. (1942). Progress report of the seismological work. Technical report, Unites States Coast and Geodetic Survey in the Western United States During 1941, 1942.

Wang, X. and Liu, P. L.-F. (2006). An analysis of 2004 sumatra earthquake fault plane mechanisms and indian ocean tsunami. *J. Hydraul. Res.*, 44(2):147–154.

Wells, R. E., Blakely, R. J., Scholl, D. W., and Ryan, H. (2011). Seismicity, topography, and free-air gravity of the aleutian-alaska subduction zone. American Geophysical Union, Fall Meeting, abstract T21B-2322.

Wells, R. E., Blakely, R. J., Sugiyama, Y., Scholl, D. W., and Dinterman, P. A. (2003). Basin-centered asperities in great subduction zone earthquakes: A link between slip, subsidence, and subduction erosion. *J. Geophys. Res.*, 108:doi:10.1029/2002JB002072.

Wendt, J., Oglesby, D. D., and Geist, E. L. (2009). Tsunamis and splay fault dynamics. *Geophys. Res. Lett.*, 36:doi:10.1029/2009GL038295.

Wilson, R. et al. (2014). The search for geologic evidence of distant-source tsunamis using new field data in california, in the safrr (science application for risk reduction) tsunami scenario. Technical report, U.S. Geol. Surv. Open File Rep., 2013-1170-C, edited by Ross, S. L. and Jones, L. M., Chap. C, pp. 122, doi:10.3133/ofr20131170c.

Yamashita, T. and Sato, R. (1974). Generation of tsunami by a fault model. *J. Phys. Earth*, 22:415–440.

Yamashita, T. and Sato, R. (1976). Correlation of tsunami and sub-oceanic rayleigh wave amplitudes possibility of the use of rayleigh wave in tsunami warning system. *J. Phys. Earth*, 24:397–416.

Yamazaki, Y., Lay, T., Cheung, K. F., Yue, H., and Kanamori, H. (2011). Modeling near-field tsunami observations to improve finite-fault slip models for the 11 march 2011 tohoku earthquake. *Geophys. Res. Lett.*, 38:doi:10.1029/2011GL049130.

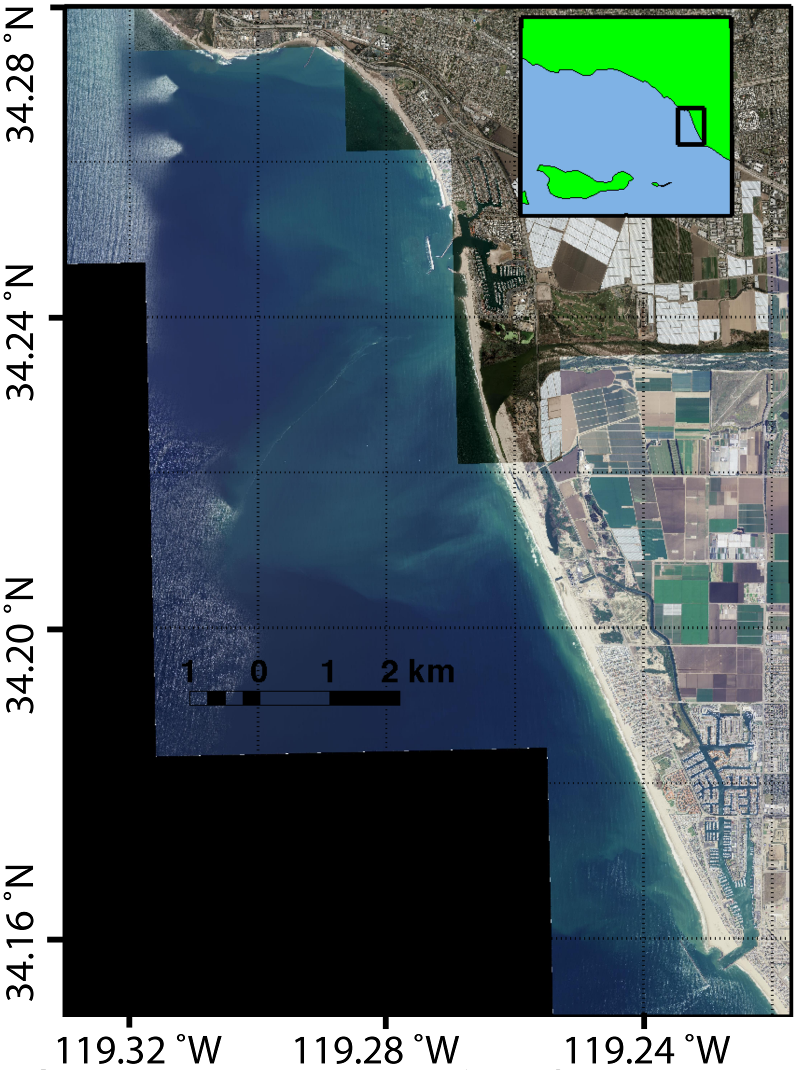

Figure A.1: Orthographic imagery of coastline indicated in figure 3.5, with modeling results removed.

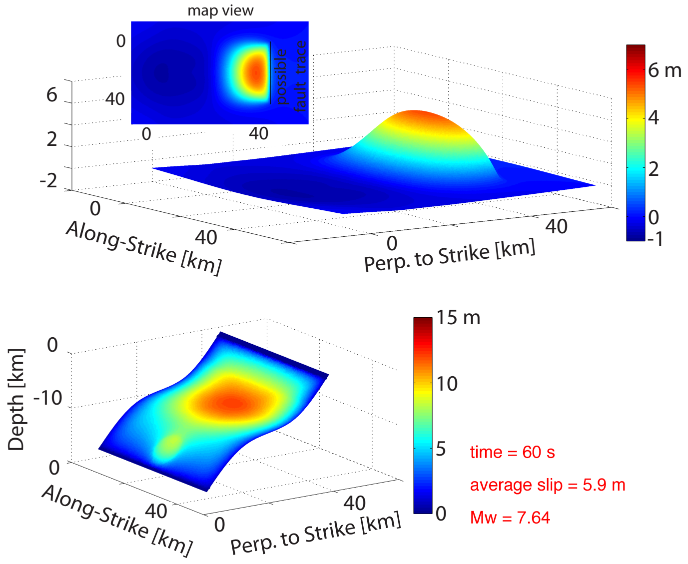

Figure A.2: Vertical free surface deformation and total slip. Top: Vertical surface (i.e., seafloor) deformation resulting from slip on the fault system, with a maximum vertical displacement of over +5 m. The map view inset shows the same vertical deformation and indicates the fault trace by a solid black line. Bottom: Amplitude of slip on the fault system, with an average of 5.9 m. Note that the final deformation and slip are shown at 60 s after nucleation. The M_w for the earthquake is 7.6.

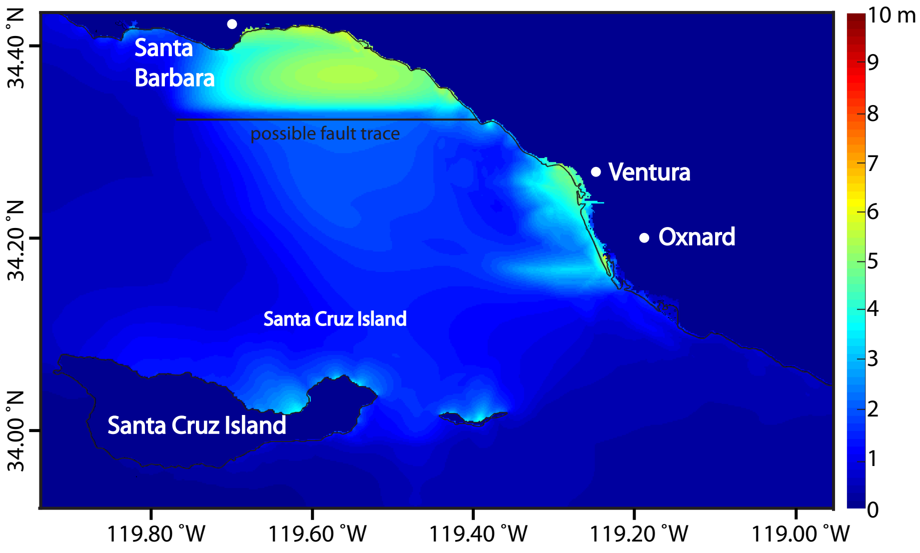

Figure A.3: Map of regional peak tsunami amplitude in meters resulting from an earthquake on the Pitas Point and Lower Red Mountain fault system. The thin solid black line indicates the coastline and the thick black line indicates the fault trace. Note that significant regional tsunami inundation occurs.

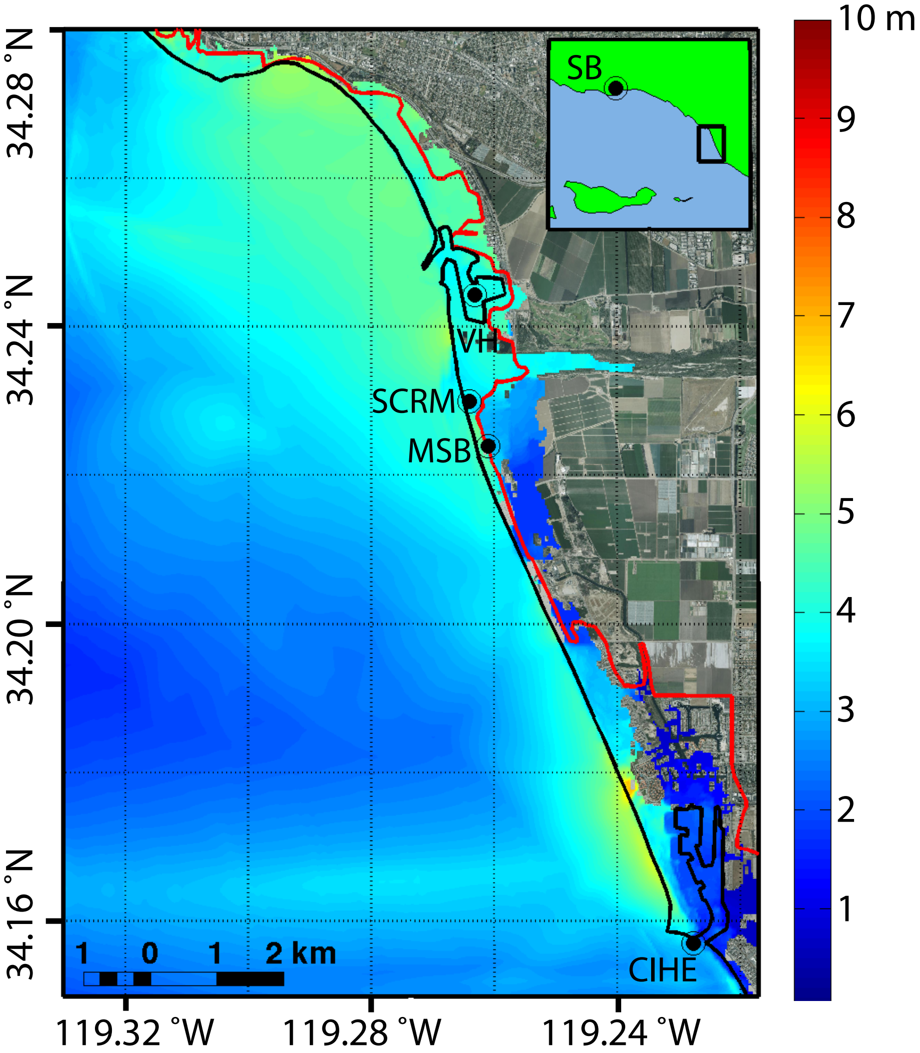

Figure A.4: Map (red box shown in figure 3.1) of localized peak tsunami amplitude, in m (around Ventura, CA), resulting from slip on the Pitas Point and Lower Red Mountain fault system. The solid black line indicates the coastline. The sold red line is the statewide tsunami inundation map coordinated by the California Emergency Management Agency. Letters indicate example locations (approximate): SB = Santa Barbara; VH = Ventura Harbor; SCRM = Santa Clara River Mouth; MSB = McGrath State Beach; CIHE = Channel Islands Harbor Entrance. Inset shows the map boundary in black. Note that inundation from the model is significantly greater in many places than the statewide estimate.